DEVELOPMENT OF CHARACTERIZATION OF 3D-PRINTED CONTINUOUS PITCH CARBON FIBER COMPOSITES

SINAN OLCUN

A THESIS SUBMITTED TO THE FACULTY OF GRADUATE STUDIES IN PARTIAL FULFILLMENT OF THE REQUIREMENTS FOR THE DEGREE OF MASTER OF APPLIED SCIENCE

GRADUATE PROGRAM IN
MECHANICAL ENGINEERING
YORK UNIVERSITY
TORONTO, ONTARIO

AUGUST 2022

Abstract

This study looks at the development of 3D printing technologies for the purpose of creating thermally conductive composites using continuous pitch carbon fiber and how various printing parameters affect thermal conductivity of samples. An initial prototype 3D printer was made with a custom dual nozzle extruder to print pitch carbon fibers, initial samples were measured with 37.1 W/mK effective thermal conductivity, this was much lower than what was expected of the samples. Imaging and μCT scanning confirmed fibers were breaking at some point in the process. A heat flow meter in a vacuum chamber was designed and fabricated to measure thermal conductivity of individual tows of carbon fibers to characterize breakage. The printing parameters affecting breakage were diagnosed and it as found that the angle between the nozzle and the printing bed had the greatest impact on breakage after a new printing system was developed using a 6-axis robot arm.

Acknowledgements

I would like to first off thank my supervisor Dr. Roger Kempers for providing all the guidance and support needed to finish this project while also creating an accepting environment at the TF-Lab, without his help and encouragement, this project could not be possible. I would also like to thank the members of the TF-Lab, Yehia Ibrahim and Caleb Isaacs were very helpful in developing the groundwork for this project and Dr. Ahmed Elkholy and Omar Khaled for supporting me the entire time and providing invaluable technical support throughout this project. Lastly, I would like to thank my friends and family, especially Arma Khan for providing amazing emotional support throughout my project.

Table of Contents

Table of Figures

List of abbreviations

CF	Carbon Fiber
PCF	Pitch Carbon Fiber
PAN	Poly-Acrylonitrile
AM	Additive Manufacturing
FFF	Fused Filament Fabrication
µCT	Micro Computed Tomography
PLA	Poly-Lactic Acid
PEEK	Poly-Ether-Ether-Ketone
PEI	Polyethyleneimine
PTFE	Polytetrafluoroethylene
GNP	Graphene Nano Platelets
CFRP	Continuous Fiber Reinforced Polymer

List of Symbols

k_{eff}	Effective Thermal Conductivity
k_f	Thermal Conductivity of Fibers
k_p	Thermal Conductivity of Polymer Matrix
v_f	Volume Fraction of Fibers
k_{meas}	Measured Thermal Conductivity
R_{meas}	Measured Thermal Resistance of Sample
Q	Heat Power Input
Q_{loss}	Heat Power Loss
V	Voltage
I	Current
L	Length
A	Cross-Sectional Area
σ	Measurement Uncertainty
T_a	Temperature of First Thermocouple
T_b	Temperature of Second Thermocouple
T_1	Temperature of First Thermistor
T_1	Temperature of Second Thermistor
$T_{surface}$	Surface Temperature
N	Layers of PLA between CF layers

Chapter 1 Introduction

The exponential growth found in the increasing transistor density within electronics has led humanity to a thermal management crisis. The rapid miniaturization of electronics for handheld devices and increased power consumption to improve product performance has forced the creation of many new techniques in improving the cooling systems for such products. Electronics that consume power dissipate most of the electricity input as thermal energy, the task of cooling these electronics has been mostly held by heatsinks. Although conventional air-cooled heatsinks have been doing an adequate job at cooling electronics for the last half of the 20th century, modern electronics have strained their usability. In general, electronics using transistors need to be kept at below 85°C to avoid damaging of the components, with the heat fluxes found in the modern era, this task is becoming unmanageable by convectional common heatsinks used [1]–[3]. Modern advancements have investigated methods of cooling high performance products more efficiently whilst reducing weight. The heavy all-metal heatsinks are not desirable for use in handheld devices, aerospace, and automotive industries as the increased weight of the heatsink will cause decreases in performance. Weight reduction has been a strategy adopted by airlines for the past decades, stories exist of companies like United Airlines switching to a lighter paper which drop the weight of their aircrafts by 11 pounds, going onto saving the company almost $300,000 a year [4]. CubeSat satellites are standardized method for researchers to send testing equipment into space, the size and weight constraints of 1 kg set by NASA generates a need for weight saving for the testers [5]. Furthermore, due to the nature of handheld and wearable technology, large strides have been made to create light weight heatsinks, such as those for wearable coolers that use innovative colling methods to cool thermoelectric devices [6], [7].

1.1 Research Motivation

Methods for weight saving in the terms of heat transfer can involve a variety of tactics, one of the most important aspects of weight reduction is the development of new materials used in heatsink designs. Aluminum and copper metals are conventionally used as heat exchanging materials, due to their high thermal conductivity, however their density is one of their greatest drawbacks. With the influx of high-power electronics, the weight of these materials has forced researchers to look at alternative materials with low density and higher thermal conductivity. New carbon-based composite materials with engineered molecular structures such as graphite, pyrolytic carbon, carbon nanotubes, and pitch carbon fibers have all been investigated [8]–[11]. Ongoing innovations into the field of manufacturing these materials necessitates new manufacturing methods for composites as well.

Additive manufacturing (AM) is an approach growing in popularity, where rather than subtracting materials from a stock material, the desired part is built up from scratch through a variety of techniques. This form of manufacturing eliminates the need for custom tooling for each part, and allows for designs to be realized much quicker, making it advantageous for use in rapid prototyping and low volume productions. Electronics in previously stated industries and experimental setups suffer from the lack of customizability in their cooling systems, as they are made in a low volume and are complex, requiring extravagant coolers to be produced through conventional techniques. Many industries have already looked to AM to cut tooling costs for low volume productions, though its use in the field of thermal management has been limited.

The combination of AM with thermally conductive materials will allow for the development of high performance heatsinks and heat exchangers to address the shortcomings of conventional heat sinks. The use of 3D printing will also allow for custom heatsinks to be manufactured with complex geometries, bespoke to the user’s needs for cooling.

1.2 Research Objectives

Previous work has shown that a viable material to be used in 3D printing for the creation of heatsinks and heat exchangers is continuous pitch carbon fiber (PCF) [12]. As continuous polyacrylonitrile (PAN) carbon fiber (CF) has been printed before into mechanically strong composites, it is hypothesised that PCF can be printed to enhance composites thermally. Therefore, this thesis will address three main objectives of this project:

1. Develop a 3D printing system which can additively manufacture continuous PCF polymer composites and quantify the effective thermal conductivity of these composites.
2. Develop an understanding of factors affecting PCF breakage during PCF processing and 3D printing, causing reductions in effective thermal conductivity.
3. Develop an improved continuous PCF 3D printing system that addresses the shortcomings of the original PCF process and helps to mitigate PCF breakage.

By accomplishing these objectives, an understanding of how PCF is affected during the printing process is developed. The methods are improved and developed which will allow future researchers to fabricate lightweight, 3D-printed heat exchangers with good PCF continuity and high effective thermal conductivity.

1.3 Thesis Outline

The thesis is organized into Chapters, with most Chapters corresponding to work done in several publications (either submitted or in preparation), with the exceptions being Chapter 2 which consists of a literature review and Chapter 7 which are the concluding remarks and outlook on the technology.

Chapter 3 represents the culmination of the work of several researchers into 3D-printed PCF composites and describes the primary approach for processing and 3D printing the

continuous PCF polymer composites used in this thesis. This Chapter details materials, PCF pre-processing, design of the 3D printer, sample fabrication, and initial sample thermal conductivity measurements. Samples were manufactured with different grades of PCF and with a range of volume fractions. Results from this Chapter were positive but highlighted the issue of fiber breakage. The understanding and mitigation of fiber breakage therefore becomes the central motivation behind the remainder of the thesis. Chapter 3 has been submitted to *Additive Manufacturing Letters* as “Thermal Conductivity of 3D-Printed Continuous Pitch Carbon Fiber Composites” and is currently under review.

Chapter 4 describes the development of a thermal metrology technique for the purpose of diagnosing how different printing parameters affect the thermal conductivity of individual PCF tows and printed rasters. This apparatus consists of a bespoke flow meter contained with a custom vacuum chamber to test individual samples using a single tow of CF. This measurement technique was required because printing larger-scale samples (such those used in Chapter 3 for experimenting of each individual printing parameter) was not feasible due to the high costs of the PCF, and the long printing times for the samples. Chapter 5 presents the results and discussions for how varying printing parameters affect PCF thermal conductivity, measured using the method developed in Chapter 4. Together, Chapters 4 and 5 are currently being drafted into a journal paper entitled “Characterization of Fiber Breakage and Effective Thermal Conductivity of 3D-Printed Continuous Pitch Carbon Fiber Composites”.

Chapter 6 presents the development and printing of continuous PCF using a revised extruder and a 6-axis robot arm. This setup was developed in order to vary printing methods, particularly the nozzle angle. Other printing operations such as printing curvatures with various radii, and corners with and without turning radii were tested to evaluate the ability to print more complex PCF composite geometries. The samples printed were also characterized using the apparatus developed in Chapter 4. Most of the work done in this Chapter was presented at ITherm

2022 in a conference paper and presentation entitled “Thermal Characterization of Continuous Pitch Carbon Fiber 3D-Printed using a 6-Axis Robot Arm” [13], and an expanded study is being drafted for journal publication.

Chapter 2 Literature Review

As electronics become smaller and power consumption increases, electronics cooling has become a major bottleneck for many industries. The aerospace, automotive, telecommunications, and wearable technologies sectors specifically require lightweight, high-performance coolers for their technology to function well. Because of its low cost, high machinability, and high thermal conductivity, aluminum has long been the dominant cooling material for many industries. Although metals such as copper and aluminum are very effective, they have weight limitations and cannot be used to create complex geometries. As a result, many researchers have explored the usage of polymer composites [14], [15]. Although polymers have low thermal conductivities, melting points, and yield strengths (which render them unlikely candidates for use as heat exchangers), they have other properties, including flexible design and an ability to accommodate fillers, which make them suitable for use in heat exchange.

2.1 Polymer Heat Exchangers

Pure polymer heat exchangers maintain high performance in low power applications while also being corrosion resistant, electrically insulated, and easy to manufacture [16]–[18]. Arie et al. manufactured an air-to-water heat exchanger by laser-melting thin layers (150 μm thickness) of high density polyethylene polymer; their designed heat exchanger had an overall heat transfer coefficient of 35–120 W/m^2K, depending on fluid flowrates [19]. It was generally seen that the thin polymer walls used for the transfer of heat only accounted for 3% of the overall thermal resistance of the system, hence the effectiveness of the polymer. Kroulíková et al. compared a commercial automotive radiator with one manufactured from bundles of thin hollow fibers (1 mm outer diameter with 0.1 mm thickness) made from Polyamide 612 [20]. The custom polymer heat exchanger was 10–15% more efficient than the metal heat exchanger and 30% lighter. Brožová et al. used similar hollow fibers to create a heat exchanger from bundles of the hollow fibers with

overall heat transfer coefficients of 250 W/m^{2}K and 80 W/m^{2}K for forced and natural convection, respectively [21]. Christmann et al. designed a falling film plate heat exchanger made from PEEK for use in seawater desalination; PEEK is an attractive choice because it has high corrosion resistance but is significantly less expensive than the corrosion resistant metal alloys generally used [22].

2.2 Polymer Composites

Pure polymer heat exchangers require extensive design efforts to accommodate the low thermal conductivity of polymers. Several methods have been devised by which thermal conductivity is increased by using thermally conductive fillers [23], [24]. High thermal conductivity fillers, such as carbon, ceramic, or metal particulates, are dispersed throughout the polymers. These fillers are in the nanometer to micrometer range, depending on particulate [25], [26]. Many studies have been carried out to create and characterize the material properties of polymer composites, because it is a tried-and-tested way to create low-weight, high-performance composites [15]–[19]. Serkan Tekce et al. investigated the effects of copper particulate, in various geometries and volume fractions, mixed into polyamide polymer; they discovered that a polymer filed with 60% copper platelets can increase effective thermal conductivity by up to 12 W/mK [32]. Trojanowski et al. discovered that a tenfold increase in the thermal conductivity of a polymer can result in heat exchanger effectiveness similar to that of one constructed from stainless steel [33]. The through-plane thermal conductivity of woven fibers was improved 2.8 times by Srinivasan et al. when they introduced diamond powder into the binding epoxy [34].

2.2.1 Particulate Filler Composites

When metallic and ceramic fillers are used in polymers, they generally only increase effective thermal conductivities by a factor of up to 10 to 20 times that of the original polymer [27]. Further improvement of the effective thermal conductivity of polymer composites requires the use

of carbon-based high thermal conductivity materials such as graphite, CFs, and carbon nanotubes. The unique chemical structure found in these materials allows them to have thermal conductivity values of 600–3000 W/mK, allowing for smaller volume fractions of fillers to greatly affect the effective thermal conductivity of the composite [26], [30], [35]. For example, Yuan et al. used multi-walled carbon nanotubes to create a composite polymer that achieved thermal conductivity of 18.9 W/mK at a relatively small weight ratio of 1% [36]. Jin Gyu et al. created composites out of stretched sheets of multi-walled carbon nanotubes that had a thermal conductivity of over 100 W/mK at higher weight concentrations of 60% [37]. Though multi-walled carbon nanotubes have the highest thermal conductivities found in engineering materials, they have yet to be adopted by industry due to high levels of impurities found in samples; rather, CFs dominate the industry at present [38].

2.2.2 Carbon Fiber Reinforced Polymer Composites

CFs are continuous chains of carbon formed into micrometer diameter fibers. Their chemical composition and orientation allow them to have excellent anisotropic material properties [39], [40]. There are two mainly used precursor materials when creating CFs which determine the final product's properties: PAN and mesophase pitch. CFs made from PAN are have smaller diameters (1–5 μm); they are used in strength reinforcing due to their high tensile strength and low cost, allowing for low weight yet strong parts [41]. Pitch-based CFs are made from mesophase pitch; this causes the fibers to form in larger diameters (10–11 μm). These fibers are known to have extremely high thermal and electrical conductivity [42]. PCF only accounts for only 5% of CFs produced because they have been generally deemed too difficult to handle due to their high brittleness compared with PAN-based CF. Manufacturing involving the use of CFs can be split into two groups identified by the usage of continuous or discontinuous fibers as fillers.

2.2.2.1 Discontinuous Carbon Fibers

Discontinuous carbon fibers are CFs that have been respectively chopped or milled mechanically to small rods or powder in sizes ranging from millimeters to micrometers. Chopped and milled fibers are simpler to implement because they can be mixed into a polymer matrix as an additive, with minimal requirements to modify manufacturing. Discontinuous CFs can be added to a polymer matrix and then extruded with ease for manufacturing methods such as injection moulding. Flöck et al. used injection moulding to create polymer composites of PEEK and CF to test for wear resistance [43]. Similarly, Yuan et al. created PEEK and CF polymer composites and tested their thermal and mechanical properties, comparing composites made from PAN and pitch CFs [44]. Discontinuous fibers are a cheap and simple way to increase the mechanical and thermal properties of polymers; however, these materials have disadvantages which can result in only marginal increases for the polymer composite over the values for the base matrix. One issue most polymer composites face is voids forming within the structure. Miyachi et al. developed a method to measure thermal diffusivity in CF and resin polymer composites [45]. By comparing impregnated and non-impregnated samples, they found that impregnated samples had, on average, double the thermal diffusivity of non-impregnated samples, implying that a large number of voids exist in the samples. Fibers suspended in the polymer matrix also need to be axially aligned because the fiber properties only exist in the axial direction. Kuriger et al. developed a novel method to align fibers during extrusion to increase thermal and mechanical properties, this method untangled the fibers and aligned them at least ±30° from the axial direction [46].

The most significant disadvantage of discontinuous fibers can be attributed to their discontinuous nature which introduces breaks in between the fibers where polymer or air voids exist, causing weak points and discontinuity. Kuriger and Alam manufactured aligned CF polymer composite samples and found that even at high levels of uniaxial alignment at a volume fraction of around 23% they showed axial thermal conductivity of approximately 6 W/mK [47]. Others have

also noticed this discrepancy: though material properties can be predicted accurately, relatively high volume fractions only yield slight increases over simple polymer matrices [48]–[50].

2.2.2.2 Continuous Carbon Fibers

Continuous CF composites, as their name suggests, are composites in which the continuous fiber is incorporated throughout the entire sample without any discontinuities, allowing for high anisotropic properties. This method is the preferred way of using CF as a composite: the resulting composite has properties like metal alloys but also decreases the overall weight significantly. The general manufacturing process for continuous CF composites involves vacuum bagging or autoclaving continuous fiber patterns in a mould and curing the resin to create a solid structure; this method is commonly used in the aerospace, automotive, and structural industries [51]–[54]. Many research studies have been conducted on optimizing and cheapening the manufacturing methods for continuous CF composites. Park et al. compared the mechanical properties of samples made from vacuum bagging and the autoclave process and discovered that, although much cheaper, the vacuum bagging process showed similar results to samples made by autoclaving [55]. Koushyar et al. further showed that manufacturing parameters such as temperature, pressure, and time during the autoclaving process can have a large impact on the sample's properties [56]. Continuous carbon fibers can also be weaved to make panels. Joven and Minaie conducted a study in which they measured the material properties of the composite sample with variations in the weave patterns [57]. Although continuous CF manufacturing has primarily used PAN carbon fibers because industries such as aerospace and automotive require lightweight and high-strength parts, these manufacturing techniques have been applied to pitch carbon fibers as well. Martins et al. used the vacuum bagging process to create a heat-dissipating electronics container; the container was able to dissipate heat almost as effectively as an identical aluminum sample while having a weight reduction of 23% [58]. Silva et al. created a pitch and PAN CF weave and measured the thermal conductivity of the whole sample while varying the

angle of the fibers to the direction of heat flow, creating thin plate samples with thermal conductivities of 150 W/mK [59]. Gaier et al. tested the thermal conductivity of woven pitch-based CF composite structures and found irregularities between predicted and experimentally obtained values; however, overall they suggest that weaving low and high thermally conductivity fibers together in such a way could allow for intricate heat transfer paths [60]. Athanasopoulos and Siakavellas successfully used pitch carbon fibers to create and test a thermal cloak, using the high anisotropic thermal conductivity to nullify heat flux and create an isothermal region across a set area [61]. Northrop Grumman Space Technology undertook an investigation into multiple materials to be used as thermal radiators to cool down electronics in space-faring satellites and compared high thermal conductivity carbon fibers composites to one another [62]. Goncharov et al. manufactured four thermal radiators made from high-thermal-conductivity continuous CF polymer composites and found that they satisfied Russian space standards in their testing [63]. Automated tape and fiber placement is another method of manufacturing with continuous fibers, in which tows of fibers are laid into a mould using a tape roller to make lightweight, high strength parts [64]–[66]. The fiber placement method allows for large scale production of composite parts, however specific issues are still faced in production that leads to defects, which have been explored by researchers [67]. Denkana et al. created a monitoring system to inspect for defects such as gaps, overlaps, twisted tows, and foreign bodies as these were deemed to be defects that cause structural weaknesses in manufactured parts [68]. Mathematical work has been done to discover algorithms for proper placement of the fibers, as depending on the stress felt by the parts, there is need to align with respect to the anisotropic properties of the fibers [69]. As can be seen, continuous fibers offer many advantages, especially in the use of lightweight high-performance structures, which has led to many studies adapting them to other manufacturing methods.

2.3 Additive Manufacturing

AM is a category of manufacturing that uses 3D printers to easily build complex geometries with metals, polymers, and ceramics from the ground up. Compared with other manufacturing methods, AM is a new and still developing field with large amounts of research still ongoing to facilitate its adoption into industries. Several unique types of AM exist, each with their own strengths and weaknesses. The most common are binder jetting, directed energy deposition, material extrusion, material jetting, powder bed fusion, sheet lamination, and vat photopolymerization [70]. Depending on the process, metal alloys, engineering polymers, ceramics, composites, smart materials, and bio-inks can all be used as precursor materials for creating parts. Further research is ongoing into different materials to be used in 3D printing [71]. Several industries have already begun employing AM because it allows rapid prototyping of bespoke parts with complex geometries. AM is particularly useful in dentistry: vat photopolymerization methods such as stereolithography are already being used to create resin orthodontic aligners, and many surgeries can be simulated on a 3D-printed model to avoid unexpected issues [72]. The aerospace industry benefits greatly from the low production volumes and high complexity made possible by AM, because these reduce the high costs and time involved in tool manufacture [73]. Companies like *Relativity Space* have already introduced metal 3D printing as an alternative manufacturing method for rockets because of the restrictive tooling costs associated with large rockets [74]. Other industries are on the cusp of adopting 3D printing as their preferred manufacturing method; in particular, the enhancement and manufacture of heat exchangers has been greatly investigated in the past decade. Current manufacturing techniques for heat exchangers are limited by the conventional machining of metal alloys and their complex assembly; designs are based on existing models of heat exchangers. Direct metal laser sintering and laser powder bed fusion manufacturing methods have been widely adopted and investigated for creating unique, single-part, metal heat exchangers with complex geometries [75], [76]. These

manufacturing methods are particularly beneficial for use in heat exchanger manufacture because of the ability to mathematically optimize designs in a way that is not feasible using conventional means. 3D printing also further improves heat transfer characteristics in heat exchangers because of the nature of the manufacturing process: rough surfaces and internal micro channels greatly increase heat transfer and pressure drop [77], [78].

2.3.1 Fused Filament Fabrication

Although 3D printing is a disruptive technology that has changed how engineers look at design and manufacturing processes, entry into the field is still prohibitively expensive because of the high costs associated with the machines. Only Fused Filament Fabrication (FFF) has found commercial success, owing to its ease of use and low cost [79]. In FFF, an extrusion system is used to primarily melt a thermoplastic precursor material though other materials; materials most often used are thermosets, rubber, ceramic, and a wide variety of composites [80]. The extruded material is guided by a three-axis CNC motion system; its motion is controlled by a Gcode file, historically used for CNC machining. The extruded material is laid down in layers to additively built parts. Thermoplastics are the simplest and easiest material to print using this method; polymers like polylactic acid (PLA), acrylonitrile butadiene styrene (ABS), and polyethylene terephthalate glycol (PETG) have become the most widely used polymers for FFF. FFF is the most widely adopted 3D printing solution because of its low cost, ease of use, rapid prototyping capabilities, and use of open-source hardware and software. FFF has limited usefulness because it uses thermoplastics which, though easy to print, have low melting points, mechanical strength, and chemical resistance; this has led to many investigations on how to improve the material properties of thermoplastics.

2.3.2 Composites in Fused Filament Fabrication

As with regular polymer structures, the need to improve material properties has yielded many investigations using both continuous and discontinuous fillers in thermoplastics. Companies like *Markforged* have taken many steps to standardize the use of fillers in FFF; their printers, which can print polymer composites with metallic and ceramic powders as well as continuous fibers such as glass, Kevlar, and carbon, have led to commercial success [81], [82]. Although continuous fillers offer far greater capabilities when incorporated into polymer composites, studies on fillers have been skewed more in favour of discontinuous fillers because no modifications are needed to the existing 3D printing infrastructure [83].

2.3.2.1 Discontinuous Fillers in Fused Filament Fabrication

In AM, discontinuous fillers and particulates are used in a similar fashion to how they are used in the conventional manufacturing of polymer composites. Within the extruder in the conventional FFF process, polymer filament of diameter 1.75 mm or 2.85 mm is inserted into the extruder. There, it is melted and mixed in the liquefier stage, then extruded out of the nozzle. Manufacturing filament with different compositions of particulate filler and polymer, then feeding that through the extruder is simple and requires no modification of the original extruder (though some hard particulate may damage the nozzle over time, making nozzles made from harder materials better suited to this method). A wide selection of particulates in different polymer matrices have been tested; studies show that metal- and carbon-based particulates have the highest impact on the material properties of manufactured composites [84]. Researchers like Singh et al. have already developed repeatable methods to improve the thermal performance of printed samples using chemical and mechanical mixing to create ABS filament with graphene filler. Zhang et al. investigated the specific heat capacity and thermal conductivity of carbon fibers chopped to lengths of 5–6 mm with carbon nanotubes grafted onto them, and carbon nanoplatelets and nanotubes in polyamide 12 at varying filler ratios [85]. Through testing of

samples produced through FFF, it was discovered that polyamide 12 with 15% carbon nanoplatelets and 1% carbon nanotubes had the highest thermal conductivity increase from that of the base polymer. Ferreira et al. conducted experimentation on the mechanical properties of 3D-printed samples made from PLA filled with 15% carbon fibers by weight (PLA+CF, ProtoPasta) [86]. As the fiber lengths found in the PLA were on average 60 µm, they helped to increase the tensile and shear modulus of the samples over the pure polymer; however, they had negligible effects on the strength of the part when tested in the direction of printing—this was attributed to the extremely short lengths of the fibers. Blanco et al. produced their own filaments, mixing PLA with 10%, 20%, and 30% PAN-based carbon fibers by weight. On examination, the thermal properties of the printed samples showed a modest improvement in thermal conductivity from 0.16 W/mK to 0.21 W/mK for the 30% CF by weight sample [87]. Zhu et al. showed that the thermal conductivity of polyamide 12 with 6% carbon nanoplatelets by weight was 51.4% higher when printed in the direction of the heat flow than if the same sample was made by compression moulding [88]. Love et al. discovered that adding 13% PAN-based carbon fibers by weight with average length of 3.2 mm to ABS polymer resulted in double the tensile strength and quadruple the tensile modulus for in-plane samples, but the samples were weaker in the z-direction [89]. The lower properties in the z-direction were attributed to the higher stiffness caused by the added filler. The layers did not conform to one another, resulting in poor adhesion; however, this also led to less curling and higher dimensional tolerance in prints. Dorigato et al. created their own composite feedstock out of ABS and multi-walled carbon nanotubes, which they used to make parts through compression moulding and FFF [90]. They learned that even though the filler particulate was discontinuous, material modulus and stiffness increased in the direction of printing. In terms of print quality, Liu et al. discovered that printing PLA with wood fibers and carbon fibers prints resulted in high formability, while the same polymer with aluminum, copper, and ceramic had higher amounts of print failure [91]. They also point out that using short fibers

reduces interlayer bonding, causing the samples to have lower material properties than those of the virgin PLA. Large area AM also takes advantage of discontinuous fibers; Hassen et al. showed that by feeding chopped carbon fibers into the screw extruder, along with the polymer matrix, large polymer composites can be produced. The shear force in the polymer during the process causes the fibers to mostly align in the direction of printing [92].

These studies on the usage of fillers in polymers for FFF arrive at similar conclusions, and three main issues can be observed in the final printed composites. First, it is paramount that the discontinuous fibers align, because multiple researchers have observed that unaligned fibers only marginally improve properties when compared with aligned fibers. Second, interlayer bonding is heavily affected by the amount of filler in the polymer: having too much filler results in poor layer adhesion, mechanically weakening the parts. Third, even when filler fibers are aligned and interlayer bonding is not an issue, the achieved increases in thermal and mechanical properties are only marginal compared with what the properties of the filler suggest could be possible.

2.3.2.2 Continuous Fillers in Fused Filament Fabrication

The manufacturing of continuous fiber composites by FFF requires that modifications be made to the commercial extruder because there are many additional aspects to consider. Conventional FFF machines have a liquefier stage in which a polymer filament of diameter 1.75 mm or 2.85 mm is inserted, melted and mixed, and then extruded out of a smaller diameter nozzle. The conventional extruder must be modified to allow for the continuous fiber to pass through the liquefier stage and out of the nozzle without breaking or mixing, or a second nozzle must be introduced specifically for the continuous fiber extrusion. In the past decade, many methods have been devised by both researchers and companies to create continuous-fiber-reinforced polymers (CFRP) using a modified FFF method, and researchers have looked into how various printing parameters affect the mechanical properties of the printed samples [93]. Continuous fiber

extruders also require a cutting and compacting mechanism for better print path controllability and higher layer bonding, respectively [94].

Due to the nature of the process, three methods exist to implement continuous fibers in the fused deposition modeling process: before the nozzle, in the nozzle, and after the nozzle [95],[96]. One of the most successful continuous fiber printers has been the Mark One (Markforged), which uses a before-the-nozzle approach to print glass, kevlar, and carbon fibers in a nylon matrix. Parts tested by Dickson et al. showed that samples printed using CF had a tensile strength 6.3 times that of the pure polymer samples [97]. Zhang et al. used numerical simulations to develop and optimize a before-the-nozzle extruder that could extrude a continuous CF composite filament; their nozzle was optimized to limit blockages and increase formability [98]. Before-the-nozzle extrusion requires the fibers used to be coated in the matrix polymer prior to printing; the coating is required because the matrix polymer will be used to fuse layers and fibers to each other. Prior coating allows for the fiber filament to be gripped by the extruder gears so that the fibers may be forced through the nozzle; otherwise, the fiber's flexibility will cause it to become pliable and clog the nozzle.

Pultrusion methods have also been developed by researchers. Vaneker developed a coating system for comingled fiber which involved feeding the fibers through a bath of molten polymer (in this case polypropylene) and out of a nozzle that created filament with diameters of 1.76 mm and 1.23 mm [99]. Similarly, Ming et al. coated fiber tows in UV curing resin prior to printing; the cool hardened resin was then extruded through a nozzle and cured on the print bed with UV lasers [100].

In-nozzle implementation is a popular method for the FFF of continuous fibers because it does not require any preprocessing of the continuous fibers and it is easy to change the matrix polymers. Matsuzaki et al. popularized this method of printing; they created a secondary port in the liquefier stage of the extruder where CF tows could be inserted, coated with the polymer

matrix, and coaxially extruded out of the nozzle [101]. Prüß and Vietor also developed a novel extruder; the fibers were fed down the center port of the extruder and two ports from the sides were used to feed polymer filaments into the liquefier [96]. The dry continuous fibers are sucked down with the flowing polymer through the nozzle. As the fibers had no rigidity to be extruded on their own, the fiber feeding could not be controlled, and this is deemed to be disadvantageous for 3D printing. Ibrahim et al. also worked on a wire 3D printing setup, which allowed them to create metal wire reinforced polymers, polymers with wires arranged in varying orientations within can then be used for various applications such as sensors or heating elements while increasing mechanical strength [102], [103].

The last method of continuous fiber implementation involves using a secondary mechanism to implant the continuous fibers after printing the polymer matrix. Mori et al. were among the first to experiment with this idea: they added continuous carbon fibers in between layers by hand during printing. The samples were then placed in an oven to fuse the CF to the polymer matrix [104]. Baumann et al. tried several approaches for post-nozzle implementation such as laying continuous fibers between layers of polymer by hand, using a heated needle to press fibers into the polymer, and using chemical solvents to melt fibers into the polymer matrix [95]. Although post-nozzle implementation of fibers gives the most direct control for continuous fiber placement, this method is more akin to techniques not considered to be AM; it also does not take advantage of many of the strengths of AM.

Testing has been carried out across the many processes used to integrate continuous fibers in FFF to see if material properties comparable to those conventionally produced can be achieved in composites. Araya-Calvo et al. measured the flexural and compressive properties of 3D-printed polyamide 6 reinforced with continuous CF produced by Markforged. The samples they tested were comparable to parts made from compression moulding [105]. Giarmas et al. 3D printed glass-fiber-reinforced nylon honeycomb structures using a Mark Two (Markforged) printer

to investigate the effects of differing fiber orientations; the final printed samples were deemed good replacements for the same structures manufactured using conventional methods [106]. Heidari-Rarani et al. manufactured their own extruder and CF filament. They printed CF-reinforced PLA samples to test bending and tensile strength, and found that the addition of continuous fibers increased the properties greatly when compared with pure PLA [107]. A large factor that causes poor results for the continuous fiber reinforced samples is the appearance of voids between the fibers and matrix. Zhang et al. show that by infusing samples with epoxy the samples had 29.3% and 22.1% higher stiffness and strength, respectively [108].

The effects of various parameters found in FFF on the properties of continuous fiber composites have been studied extensively. Chacón et al. studied the effects of varying fiber volume fraction, build orientation, and layer height for nylon reinforced with various continuous fibers [109]. Unconventional printing methods for continuous fibers, such as variable layer thickness and non-flat layers, have also been studied and found to be effective [110][111].

2.3.2.3 Continuous Pitch Carbon Fiber in Additive Manufacturing

Although many studies have been carried out on continuous fibers in AM, most of these studies compare the various mechanical properties found in polymers reinforced with either natural fibers or PAN-based carbon fibers. Examination of thermal properties has largely been restricted to polymers with discontinuous fillers, with no studies or work carried out to date on additively manufacturing thermal conductive composites using continuous fibers. Comparing to other metals and polymer composites with respect to thermal conductivity and density (specific thermal conductivity), a large opportunity presents itself as PLA with 20% volume fraction scores higher on this figure of merit then other materials, as seen in Figure 2-1. Compared to other composites using graphene-based fillers, higher thermal conductivities with lower weight and filler volume fraction can be obtained.

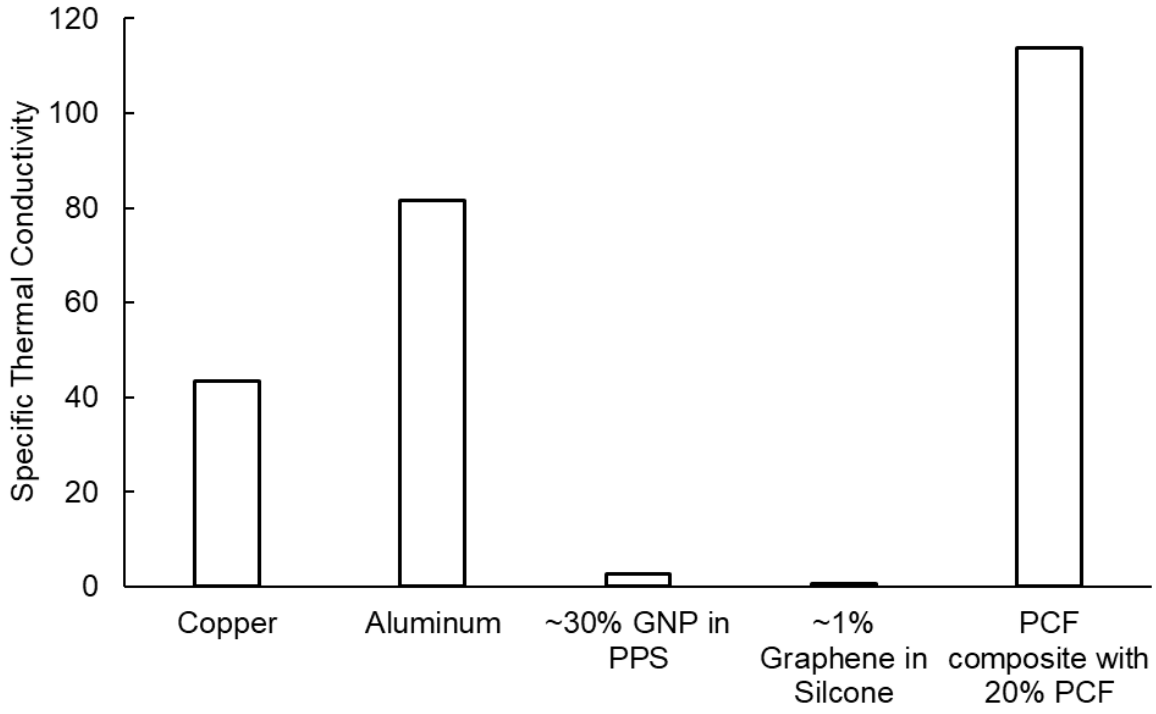

Figure 2-1: Specific thermal conductivity (thermal conductivity divided by density) of varying metals and graphene polymer composites [29].

Pitch-based carbon fibers have only been used as chopped or milled fibers mixed into polymer matrices to improve thermal conductivity; little to no work has been done to investigate continuous pitch carbon fibers (PCF) in FFF. This is likely because of the extreme brittleness of pitch carbon fibers; the harsh 90˚ angle the nozzle makes with the printing surface is hypothesized to cause large amounts of breakage. Initial studies by Ibrahim et al. determined that if a continuous PCF-reinforced polymer composite could be printed, with PCF making 20% of the volume fraction, polymer composite thermal conductivity would rival that of aluminum alloy 6061 which is commonly used in heat sink applications [112].

Chapter 3 Continuous Pitch Carbon Fiber 3D Printing

The lack of literature investigating continuous PCF 3D printing has led to the investigation of discovering a method to 3D print high effective thermal conductivity samples. The use of fused deposition modeling to extrude continuous PCF would allow for samples with directed heat flow paths. The use of AM would also allow for higher volume fractions of PCF as the extrusion will be much more controlled than what can be achieved by hand laying. This study explores the creation of the continuous PCF printing setup and the testing of samples effective thermal conductivity produced by the new 3D printer. The effective thermal conductivity was compared to the parallel analytical model to witness how effectively the continuous PCF was printed.

3.1 Methodology & Experimental Set-up

PCF produced by Mitsubishi Chemicals were chosen and used in the 3D printing process as seen in Table 3-1 due to their high thermal conductivity and commercial availability. The polymer matrix used throughout the composites produced in this study was limited to PLA, this polymer was used due to its ease of printability and low cost, later on different polymer matrices should be looked into, especially if the outlook tends towards high temperature settings.

Table 3-1: Material properties of continuous PCF (Mitsubishi Chemicals).

Property	Density	Yield	Tensile Strength	Tensile Modulus	Thermal Conductivity	Electrical Resistance	Fiber Diameter	Fiber Tow Count
Units	**g/cm3**	**g/1000m**	**MPa**	**GPa**	**W/mK**	**μΩm**	**μm**	**Fibers**
K13D2U	2.21	365	3799	938	765	1.5	11	2000
K1392U	2.15	270	3700	760	210	5	10	2000
K1352U	2.12	270	3600	620	140	6.6	10	2000

3.1.1 Modified 3D Printing Process

Before 3D printing with the PCF listed in Table 3-1, the fibers had to be coated with the polymer matrix, this was a necessity as the CF did not have the rigidity required to be fed through a direct drive extrusion system. This coating was done using a custom pultrusion device, the apparatus included a polymer bath which the CF would be passed through. After the polymer

bath, the CF would be pulled through a nozzle, the nozzle diameter was set to 0.8 mm, this diameter was chosen as smaller diameters meant it was harder to initially feed the carbon fibers through, while larger diameters would mean that the filament produced would be too thick to extrude. After the PCF was pultruded through the nozzle, it would be laid on an aluminum cooling rack, which in the end resulted in 2 m long PCF filaments that could be fed into the extruder. Rolling the PCF filament was not possible has the hardening of the PLA as it cooled immediately after leaving the polymer bath meant that the new filament was far too brittle to be rolled up. The process of coating the PCF can be seen in Figure 3-1.

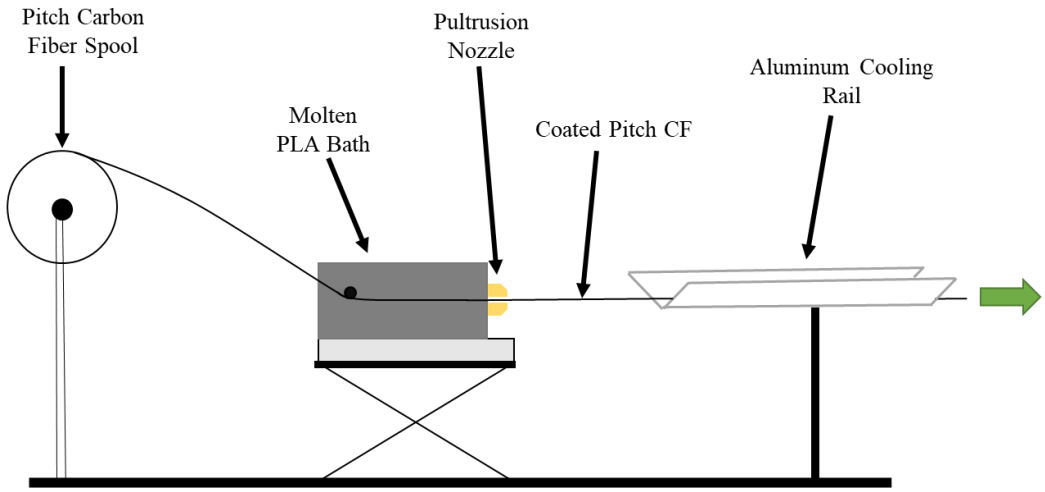

Figure 3-1: Diagram of the pitch carbon fiber filament creation process.

As the biggest problem with 3D printing of continuous PCF was the high brittleness of the fibers, a new nozzle was designed and fabricated to amend for this inconvenience. In other studies, the continuous printed wires or fibers are extruded from the nozzle at a 90° angle to the printing bed. This sharp angle can exacerbate fiber breakage during the extrusion of pitch-based CF due to its lower flexural strength, especially compared with metal wires and PAN fibers used in previous studies. Breakage of the continuous fibers must be avoided as this reduces the effective thermal conductivity of the fabricated composite due to the discontinuity in the heat flow paths.

In the present study, an open-source FFF printer (Prusa MK2 i3, Prusa Research) was modified to print with the pre-coated pitch-based CF filaments described in Figure 3-1. To help address the challenge of PCF breakage, a custom printing head angled at 45° to the printed bed was designed to prevent fiber breakage by reducing the bending stress on the CF filament during extrusion. The custom heating block was made of aluminum and designed to allow for the use of dual extrusion nozzles as shown in Figure 3-2. The right nozzle was used to extrude the polymer matrix at 90° to the bed, while the left nozzle printed the pre-coated fibers at 45°. In doing so, the fibers were subjected to less shear stress during extrusion, and the use of dual nozzles allowed for more control over the fiber-to-polymer ratio and print quality.

A second feed motor was used to control the independent extrusion of the fibers and the polymer. The fiber feed motor was fixed directly in front of the fiber printing heat sink, allowing for optimal control in feeding the fibers into the printing nozzle, with the shaft of the motor wrapped in rubber to ensure feeding traction. The fibers were fed all the way through the heat sink with a PTFE tube to guide the filament until it was extruded; this insulated the fiber filament to ensure it did not melt and clog inside the nozzle.

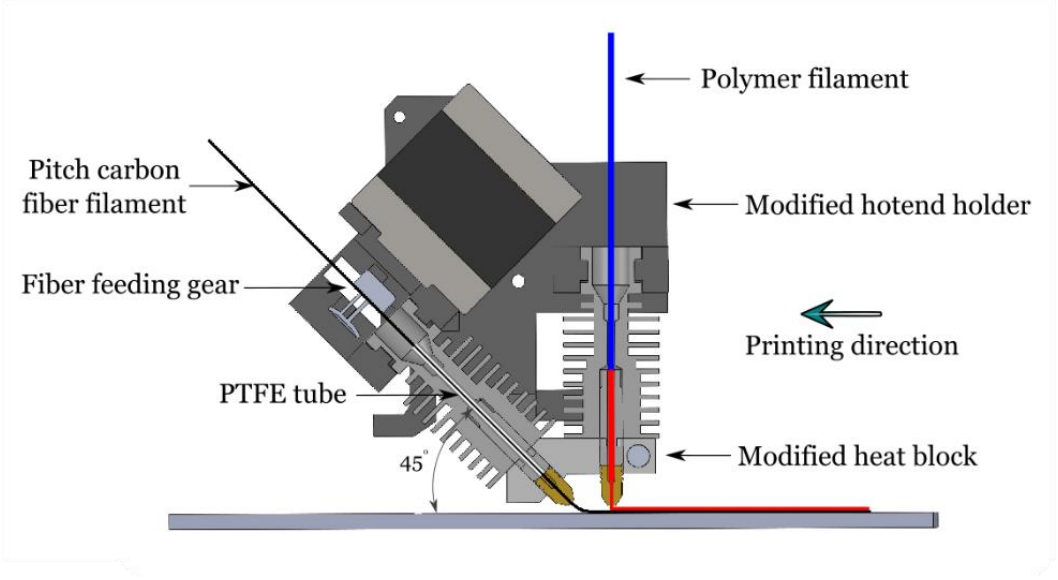

Figure 3-2: Diagram of the initial continuous pitch carbon fiber printhead.

The polymer was fed separately using the conventional Bowden extruder mechanism specified by the Prusa multi-material expansion kit. Standard 30 mm cooling fans were used to cool the polymer and fiber filament heat sinks. Also, while the figure shows both nozzles extruding simultaneously, in practice only one nozzle was used at a time for a given layer, as explained below. The angled printhead however resulted in restrictions for printability as the 45° angle was only a factor in decreasing breakage when printing in the positive X-direction, which meant that the PCF could only be printed in a single direction. Future innovations seen in Chapter 6 amended this issue, resulting in far less restrictions when it came to 3D printing.

3.1.2 Printing Properties

The printing parameters are summarized in Table 3-2. For the approximately 1 mm diameter coated fiber filament, a nozzle diameter of 1.5 mm was used to help minimize friction between the fibers and the nozzle. A polymer nozzle of 1mm was selected to match the filament diameter; however, it can be changed to any size. The printing temperature was set to 200°C which is recommended for PLA. The lower printing speed was selected (800 mm/min) to allow for the solidification of the PLA within the fiber filament while printing; it also helped the geometrical quality of the printed components.

Table 3-2: Printing parameters for samples produced.

Fiber Filament Diameter	1	mm
Fiber Nozzle Diameter	1.5	mm
Fiber Printing Speed	50	mm/s
Polymer Filament Diameter	1.75	mm
Polymer Nozzle Diameter	1	mm
Polymer Printing Speed	20	mm/s
Extruder Temperature	200	°C

To facilitate full control over fiber and polymer layers, a fiber cutting mechanism is usually implemented. However, for the unidirectional samples printed in the present study, the fiber was sufficiently brittle such that inclusion in the printing code of a sudden movement of the printing head in the reverse direction was sufficient to break the fibers. This allowed for the printing of different fibers and polymer rasters in the same printing layer.

3.1.3 Sample Preparation

To vary the PCF volume content of the samples, the amount of PLA layers in between layers of PCF were controlled, the construction of the sample scan be seen in Figure 3-3. The Gcode, which defines to motion taken by the printer to create the samples, was set to 3 different settings in which the number of PLA layers were between each layer of PCF layers, N, was set to 2, 3 and 4 layers. Controlling N was a simple and functional method in controlling volume fraction of the samples, giving a good variety of volume fractions while being able to keep all other parameters identical for all the samples. Nine samples in total were produced, the same volume fraction control method was used for the other two fiber grades discussed in Table 3-1.

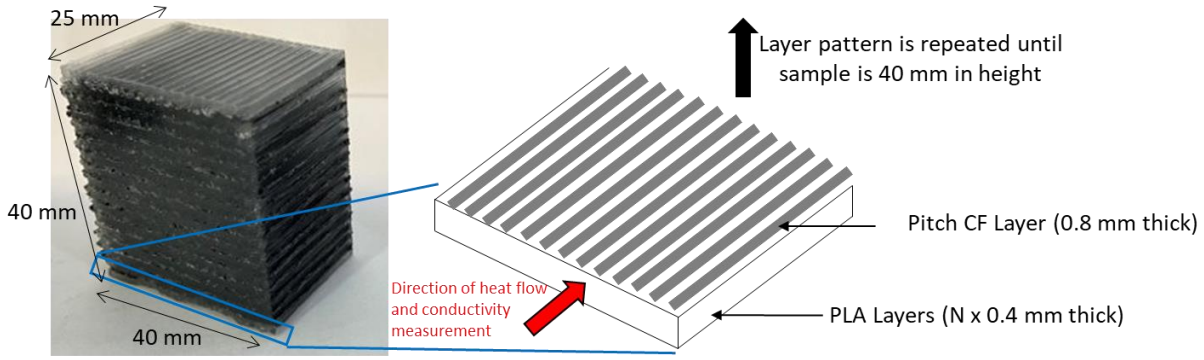

Figure 3-3: Schematic of how layers are built using the Gcode, with a photograph of a sample for context/

For each grade of CF used and stated in Table 3-1, three samples with varying PCF content were prepared. Figure 3-4 shows the photographs taken of these samples, the plane in

which the heat would be flowing was set to 40 mm by 40 mm, with the thickness being set to approximately 25 mm. The layer height for the PLA layers were set to 0.4 mm, with the layers of PCF being set to 0.8 mm.

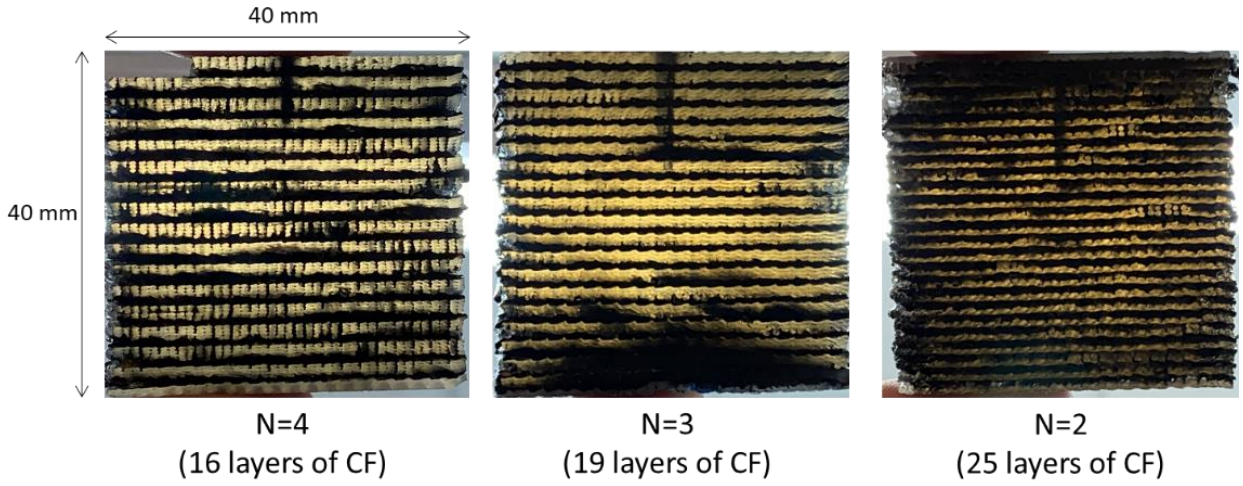

Figure 3-4: Images of the cross-sectional areas of the samples with varying fiber content.

3.2 Thermal Conductivity Characterization

Prior studies have shown that the best model for estimating thermal conductivity when dealing with composites is the use of the parallel model described by equation (3-1).

$$k_{eff} = v_f k_f + (1 - v_f) k_p \tag{3-1}$$

Using this model in which the fiber volume fraction v_f, is used along side the polymer and fiber thermal conductivities k_p and k_f respectively to calculate the effective thermal conductivity k_{eff} of the samples. k_p was set to 0.2 W/mK as this was discovered in previous experimentation to be the thermal conductivity of the polymer in the given orientation [113]. k_f was set to 800 W/mK as stated by the manufacturer in Table 3-1. Volume percentage of CF in each sample was calculated by finding the sum of the cross-sectional area of all the individual fibers and dividing

by the total cross-sectional area of the samples. A layer of CF found in the sample consisted of 40 rasters, with each raster theoretically containing 2000 fibers as stated by the manufacturer. Three separate G-code files were created as discussed earlier, with 16, 19, and 25 layers of CF evenly distributed through the sample. With knowledge of the cross-sectional area of a single fiber and the total number of fibers in the sample, the volume percentage of the fibers could be calculated.

3.2.1 Metrology Technique

A guarded heat flow apparatus was used, designed and built by Elkholy et al., to measure effective thermal conductivity of samples, the device will measure the steady state thermal resistance and calculate thermal conductivity through Fourier's law [113], [114]. A schematic of the apparatus is shown Figure 3-5. Input power is conducted from the primary heating block, through the sample, to the primary cooling block. Two calibrated thermocouples are embedded 10 mm apart within each sample (denoted by T_a and T_b in Figure 3-5). This removes contact resistance from the conductivity measurement. The thermal power is provided electrically by four cartridge heaters embedded in the main heating block, as shown in Figure 3-5. To achieve a one-dimensional heat flow through the sample and eliminate heat loss to the ambient, the primary heating block was enclosed by a secondary heating block which served as a guard heater. The power supplied to the guard heater block was independently controlled to achieve the same temperature as the primary heating block, ensuring that all input power to the primary heating block flowed through the sample. Consequently, at steady-state conditions, the sample thermal resistance R_{meas} was measured using equation (3-2).

$$R_{meas} = \frac{(T_a - T_b)}{Q} \tag{3-2}$$

T_a and T_b denote the measured temperatures within the sample, and Q is the input power to the primary heating block measured electrically (Q= IV). Thus, the thermal conductivity can be calculated by simplifying equation (3-2).

$$k_{meas} = \frac{L}{A\left[\frac{(T_a - T_b)}{Q}\right]} \tag{3-3}$$

Equation (3-3) shows the simplified for of the equation used to solve for the effective thermal conductivity k_{meas} in which L is the length between the two Thermocouples, and A is the cross-sectional area of the samples.

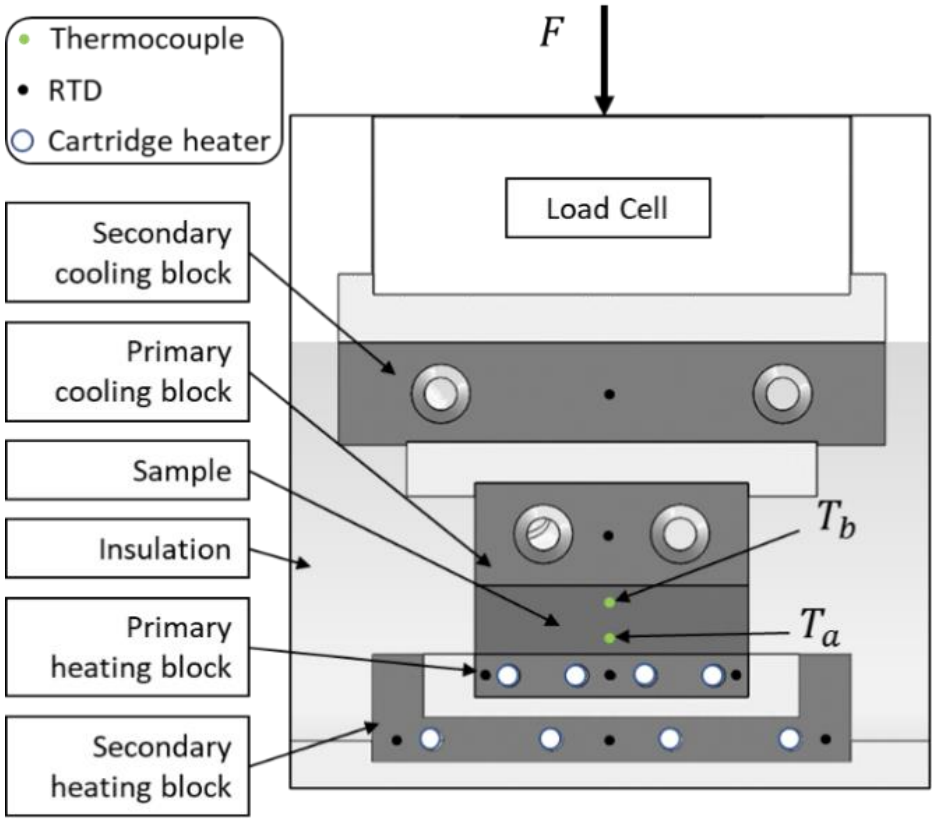

Figure 3-5: Schematic of the guarded heat flow meter used for testing of samples.

3.3 Results

The three grades of PCF listed in Table 3-1 were each printed at three different volume fractions using the layer configurations shown in Figure 3-4. Their effective thermal conductivity as a function of volume fraction is shown in Figure 3-6. Generally, the samples with higher fiber conductivities tended to have higher measured effective thermal conductivities at a given volume fraction. Also, broadly speaking, the effective conductivity of the samples tended to increase with volume fraction. The highest measured thermal conductivity was 37.1 W/mK for the D2U sample with a volume fraction of 9.5% PCF. That said, the effective conductivities tended to plateau (and slightly decrease in the case of the K13D2U fiber) at the highest volume fraction. Here, only two layers of polymer existed between each of the CF layers and visual observation suggested that the print quality of subsequent CF rasters was somewhat poorer, leading to fiber breakage.

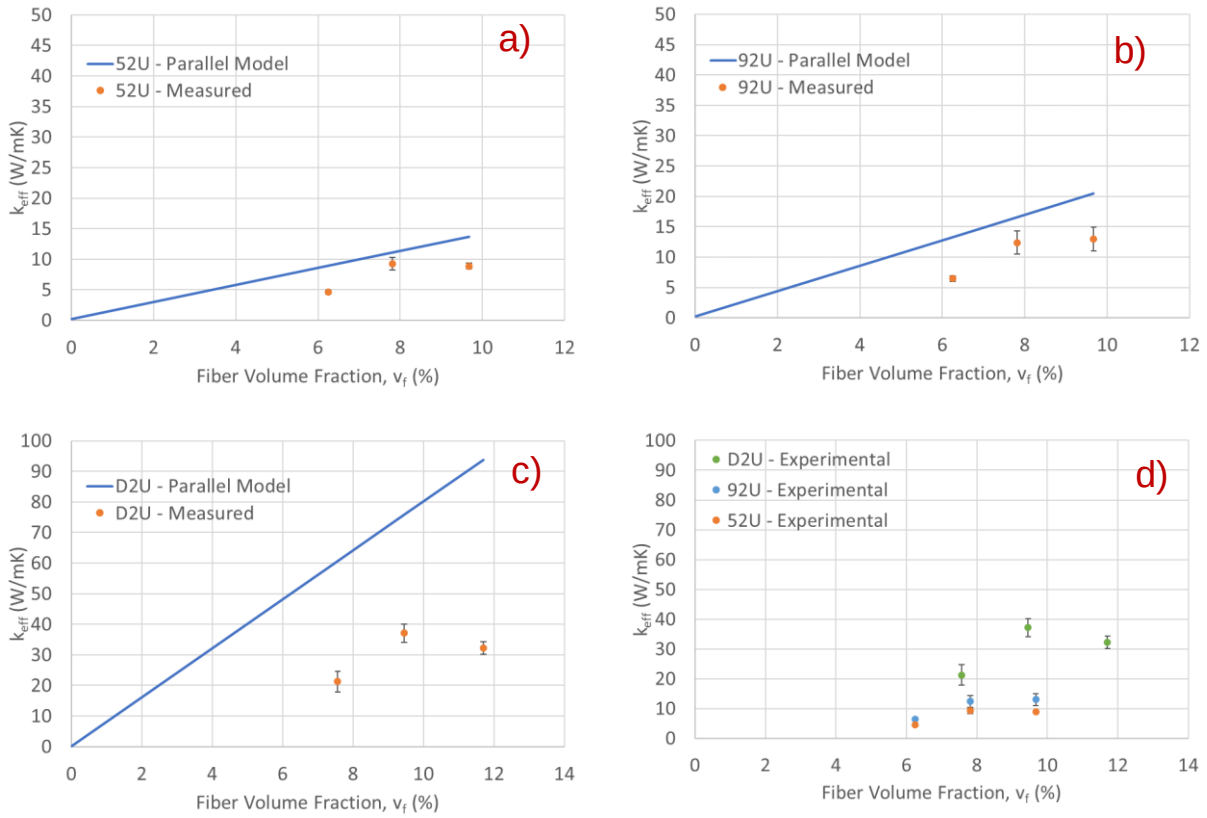

Figure 3-6: Sample thermal conductivity (measured and predicted by the parallel model) as a function of fiber volume fraction for fiber grades a) K1352U, b) K1392U, c) K13D2U, and d) a comparison of measured thermal conductivity of all three fiber grades.

The corresponding thermal conductivity predicted using the continuous parallel thermal model is also plotted in Figure 3-6. The model predicts a linear variation in effective thermal conductivity as a function of volume fraction. For all the samples tested, their measured thermal conductivities are lower than that predicted by the parallel model: The K1352U samples had average k_{eff} values that were 33% lower than predicted by equation (3-1), the K1392U samples were on average 38% lower, and the K13D2U samples were on average 61% lower.

It is important to note that the parallel rule-of-mixture model represents an idealized thermal model where there is no breakage of fibers and therefore no discontinuity in the conduction path. Because pitch-based carbon fibers are relatively brittle compared with PAN fibers, the deviation between the model and the experimental results is conjectured to be caused by fiber breakage during the coating and/or printing process, causing discontinuities in the fibers of the 3D-printed CFPC samples. In addition, the deviations from the model's predictions suggest that the relative degree of fiber breakage depends on the grade of fiber used: The pitch-based CF grades with lower thermal conductivities and tensile modulus exhibit less breakage than the samples printed with CF with higher thermal conductivity and tensile modulus.

3.3.1 Fiber Breakage Analysis

Micro-computed tomography (μCT) was used to investigate the morphology of the printed samples and assess the existence and degree of fiber breakage. Methods similar to those by Melenka et al. used to identify quality of braided fiber composites can allow for better understanding of created composites and the fibers within [115]. An 8mm x 8mm x 20mm section of the 3D-printed K13D2U sample (9.5% v_f) was cut from the larger 3D-printed sample for microCT scanning. A Bruker SkyScan 1272 MicroCT was used to image the sample. Images of the printed samples had a resolution of 4904 x 3280 pixels with an individual pixel size of 0.5μm in length. In total, 3600 images were captured at rotational steps of 0.1°, with the full scan taking 5 h to complete. Sample images were then reconstructed into cross-sectional scans using

NRecon (Bruker-MicroCT) to create 500 images perpendicular to the z-axis. These images were used to reconstruct a 3D representation of the sample in which only the fibers were visible; this could be further examined for printing errors. Images of the 9.5% v_f K13D2U sample are shown in Figure 3-7. Here, fiber breakage and misalignment are distinctly visible. This provides a reasonable explanation for the somewhat lower k_{eff} measurements than predicted by the parallel rule-of-mixture model. Analysis of the images revealed that breakage of the PCF tended to occur more on the upper side of the CF layers, which is hypothesized to be due to forces exerted by the polymer extruder passing over the layers and pushing down on the previously printed CF layer. Although the images show breakage, it should be noted that detailed analysis would be a more accurate way of determining and quantifying breakage

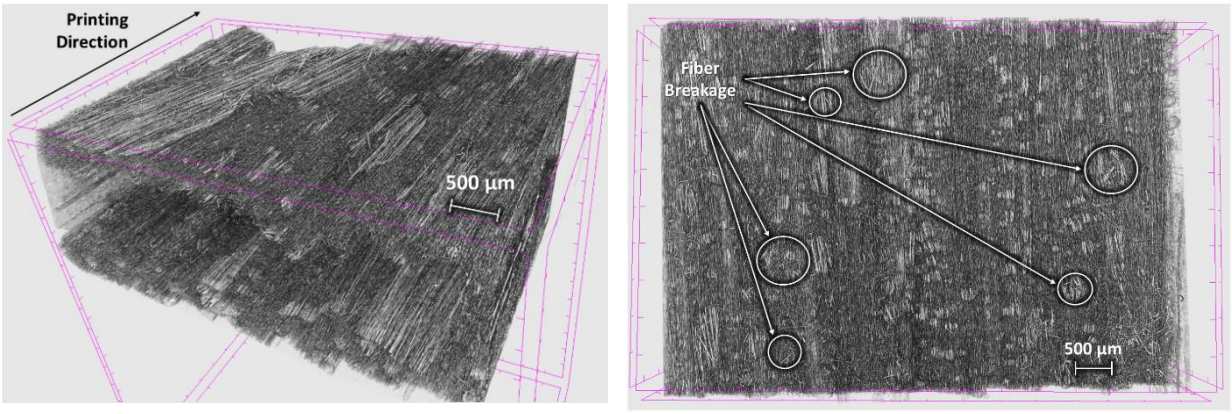

Figure 3-7: MicroCT images of sample K13D2U at 9.5% fiber volume fraction showing fiber breakage.

3.3.2 Comparison with Other 3D-Printed Carbon Composites

Several previous investigations have 3D-printed polymer composites which contain some type of carbon-based filler; however, most of these have focused on the mechanical properties of the printed components. Only a handful of studies have characterized the thermal conductivity of 3D-printed composites, and the maximum thermal conductivity from these investigations are summarized in Table 3-3.

Table 3-3: Summary of Thermal Conductivities of 3D-Printed Carbon-Based Composites

Fiber/Filler Material(s)	**Matrix Material**	**Filler Type**	**Filler Fraction**	**Max. Thermal Conductivity (W/mK)**	**Ref.**
Carbon fiber	Acrylonitrile butadiene styrene (ABS)	Discontinuous	1.7% by vol.	0.22	[116]
Graphite	ABS	Discontinuous	4.3% by vol.	0.37	[116]
Carbon fiber	Polyether ether ketone (PEEK)	Discontinuous	30% by wt.	0.61 (at 25°C)	[117]
Carbon fiber	Polypropylene	Discontinuous	10% by vol.	0.869	[118]
Graphite nanoplatelets and carbon fiber	EPON 862	Discontinuous	7.6% CF and 9.3% graphite by wt.	1.83 (at 25°C)	[119]
Graphene nanoplatelets (GNPs) and carbon nanotubes (CNTs)	Polyamide 12 (PA12)	Discontinuous	15% GNP and 1% CNT by wt.	0.73 (at 30°C)	[85]
Carbon fiber and alumina	Silicone rubber	Discontinuous	12% CF and 30% alumina by vol.	7.36	[120]
PAN carbon fiber	Nylon	Continuous	32.2% by vol.	2.97	[112]
Pitch carbon fiber	PLA	Continuous	9.5% by vol.	37.1	Present Work

In all cases, the thermal conductivity of the 3D-printed composite was higher than the base matrix material. Most previous studies used discontinuous filler particles which were premixed with the matrix materials in the desired volume fraction prior to extrusion. This allowed for good control over the filler fraction and generally required minimal modification to the printing hardware itself. Investigations which combined CF with other filler materials, such as graphene nanoplatelets (GNP) or alumina exhibited somewhat higher measured thermal conductivities

(e.g., up to 7.46 W/mK measured by Ji et al.) [119], [120]. In the study by Ibrahim et al., 3D-printed composites which used continuous CF yielded a maximum effective thermal conductivity of 2.97 W/mK but required a volume fraction of 32.2% because of the relatively low thermal conductivity of the PAN fibers used [112].

The present work differs from previous work done by using nominally continuous PCF, which have significantly higher thermal conductivities than PAN fibers and therefore require less fiber volume fraction filler to achieve 3D-printed composites with higher effective thermal conductivity. However, the main drawback of this approach is the increased brittleness of the fiber, which results in a significant degree of breakage during printing and limits the thermal conductivity of the samples. However, despite having lower than predicted values, the thermal conductivities measured herein are significantly higher than any previously 3D-printed carbon-based composite and show promise for potential heat transfer applications. For example, the thermal conductivities of the D2U 3D-printed composites are significantly higher than those of stainless steel (k≈18 W/mK).

3.4 Discussion and Conclusion

A method for 3D printing pitch-based continuous CF using a low-cost, open-source 3D printer was developed and used to fabricate unidirectional PCF and PLA composites. The effective thermal conductivities of 3D-printed CFPC samples fabricated from fibers of different conductivities and at different volume fractions were characterized experimentally and compared to the parallel rule-of-mixture model. The key findings are as follows:

- Effective thermal conductivity increased with pitch fiber conductivity.
- Sample thermal conductivity generally increased with fiber volume fraction; however, for the highest volume fractions, k_{eff} tended to plateau.

- A maximum effective thermal conductivity of 37.1 W/mK was measured using a 9.5% volume fraction of pitch carbon fiber.
- The parallel thermal model overpredicted the effective thermal conductivity of the samples due to suspected fiber breakage occurring during the printing process.
- MicroCT analysis confirmed a degree of breakage in the printed fiber rasters.

The next Chapters will address improving the thermal conductivity of the printed parts by developing a better understanding of factors affecting fiber breakage and to improve the PCF extrusion process to mitigate fiber breakage. In the future, more work should be done to quantify breakage in samples through software used in µCT imaging, which could accurately describe the amount of breakage within samples. K1352U and K1392U polymer composites should also be imaged to compare the amounts of breakage. Software analysis can show what exactly is happening within the samples 3D printed, showing whether it is breakage, misalignment, or some other mechanism that is present causing a decrease in thermal conductivity.

Chapter 4 Tow Thermal Conductivity Measurement Apparatus

Work done in the previous Chapter has presented an issue when it comes to 3D printing of PCF: the main issue being the breakage that occurs due to the brittleness of the fibers. As found in Figure 3-7, it is known that fibers break at some point during the printing process. Many different printing parameters exist that affect the integrity of the fibers, requiring a new method to understand the effects of the parameters, as they are varied. Visual techniques such as microscopy and µCT scanning exist to visualize the breakage of fibers at a micro-scale; however, these methods present difficulty when comparing two samples with similar levels of breakage and they only offer a qualitative look at the samples. Different methods of measuring breakage quantitatively in continuous fiber composites were researched, however, thermal conductivity measurement was deemed to be the best way to measure the level of breakage. Although thermal conductivity measurements do not directly correlate to the amount of breakage, by using these measurements, an estimate of how much disruption to the fibers is occurring can be achieved by individual printing parameters. The high thermal conductivity found in the PCF yields high sensitivity in measurement whilst having low amounts of heat loss to surroundings. Other methods were also used to investigate breakage, Hu et al. used microscopy on printed fibers at different stages to determine the degree of breakage caused by that stage of printing with success [121]. The microscopy method was able to see the breakage, yet it could not quantify breakage, hence Hu et al. had to do mechanical tensile and compressive tests to quantify the breakage. The Caminero et al. research group looked at non-destructive ways to see breakage in samples, using a scanning electron microscope to adequately examine the areas of breakage, this method was able to show the breakage in a detailed manner [122]–[124]. Liao et al. showed that µCT scanners could be used to examine the individual fibers, this process however was found to be a slow method as each scan can only look at a small volume while taking a long time to process [125]. This Chapter describes the design, manufacturing, and commissioning of a low-power thermal

conductivity measurement apparatus for quantifying the degree of fiber breakage in single tows (coated or uncoated) of PCF or PCF rasters after printing. Such a device will allow for quantification of fiber breakage along a raster of fibers, which will provide the ability to diagnose breakage in the fibers.

4.1 Thermal Conductivity Measurement

Ascertaining the degree of breakage after the tow found in the AM method devised, requires for a robust apparatus to measure the thermal conductivity of a single tow of carbon fiber. Long samples need to be measured with minimal heat loss and good accuracy. The testing apparatus is also expected to be of simple construction and easy to use, as many samples must be tested, and a steady state measurement is desired. Apparatuses such as the 3ω technique initially seem ideal as they neglect heat loss from samples, giving the best accuracy. However, this method would be hard to implement for continuous wire samples, as it is believed that the high thermal conductivity of the samples would result in low heat loss from the sample during testing [126], [127]. More complex techniques such as Raman spectroscopy and laser flashing have been used by others to measure thermal conductivity of carbon fibers, but were deemed unreasonable due to lack of resources [128], [129]. T-type probe methods have been used to measure thermal conductivity of thin fibers in a simple manner, however these methods are only tested for singular fibers with no coating; 3D printed PCF exist in a matrix, which is hypothesized to cause issues [130]–[133]. Several direct heating techniques were found, and eventually, a method akin to those by Piraux et al. and May et al. was chosen. The utilized method requires temperature sensors to be placed along a suspended wire to measure the temperature gradient in a vacuum chamber [134], [135]. Such a design would allow for troubleshooting of printing systems and understanding of how different printing parameters affect thermal conductivity of the fibers in the future.

4.1.1 Description of Measurement Process

The steady state approach devised for this project would be conceptually close to Figure 4-1, in which two temperature sensing elements will be used to measure a temperature gradient across samples. Samples will be clamped on either end, a small copper clamp will be used to apply heat power through the samples and a cold block kept at a constant temperature will be used to promote heat flow.

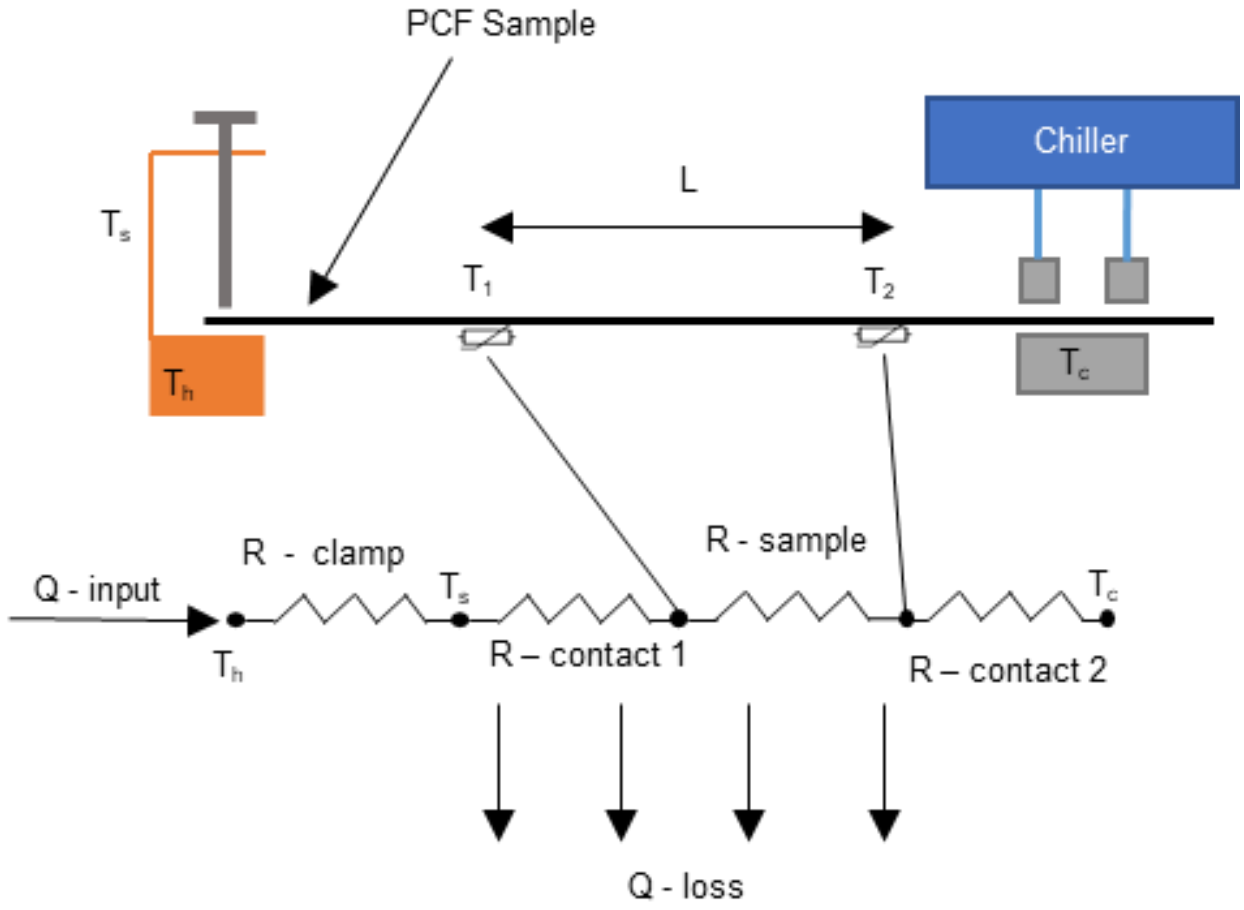

Figure 4-1: Heat flow apparatus configuration.

The thermal resistance R_{Sample} of the sample is measured according to:

$$R_{Sample} = \frac{T_1 - T_2}{Q_{input}} \tag{4-1}$$

where T_1 and T_2 are the measured temperatures across the sample and Q_{input} is the electrical input power to the heater. This approach relies on the assumption that heat loss via convection and radiation from the sample, and the heating clamp are minimal. Otherwise, measurements will result in overestimation of the thermal conductivity due to the relatively high surface area of samples and clamp as compared to the cross-sectional area of the sample. To address this issue a vacuum chamber is proposed, which would limit the amount of heat being lost to the environment. Although extremely high vacuum systems would be necessary to reduce all heat leakage, by reducing to a sufficient vacuum, a heat loss calibration can be done to accurately measure thermal conductivity of samples.

A thermistor (GAG22K7MCD419, TE Connectivity) probe was embedded tightly into a small, machined copper clamp, which was then used to clamp on the end of the PCF tow. A Keithley 2400 Sourcemeter was used to control and measure the electrical power applied to the thermistor probe. The opposite end of the tow was clamped to a copper water block which was kept at a constant stable cold temperature using a PID thermoelectric water chiller. The temperature drop between the two sensing thermistors is measured using a Lakeshore Model 370 AC Resistance Bridge, to accurately measure the resistance of the two thermistor probes with minimal self-heating in the four-wire configuration. These two sensors were calibrated together by finding resistance values corresponding to the temperature measured by an accurate RTD (5606 Full Immersion PRT, Fluke) in an insulated box with controlled ambient temperature, such that the resistors were found to show the same temperature reading with a maximum uncertainty of approximately 0.02 K. During sample testing, typical temperature differences were approximately 3-5 °C (depending on thermal conductivity of the sample) for input powers of on the order of 10^{-2} W. Temperature and input power measurements were collected and displayed by a MATLAB script. All tests were run until steady state was achieved. The set-up and experimentation process are visualized in Figure 4-2.

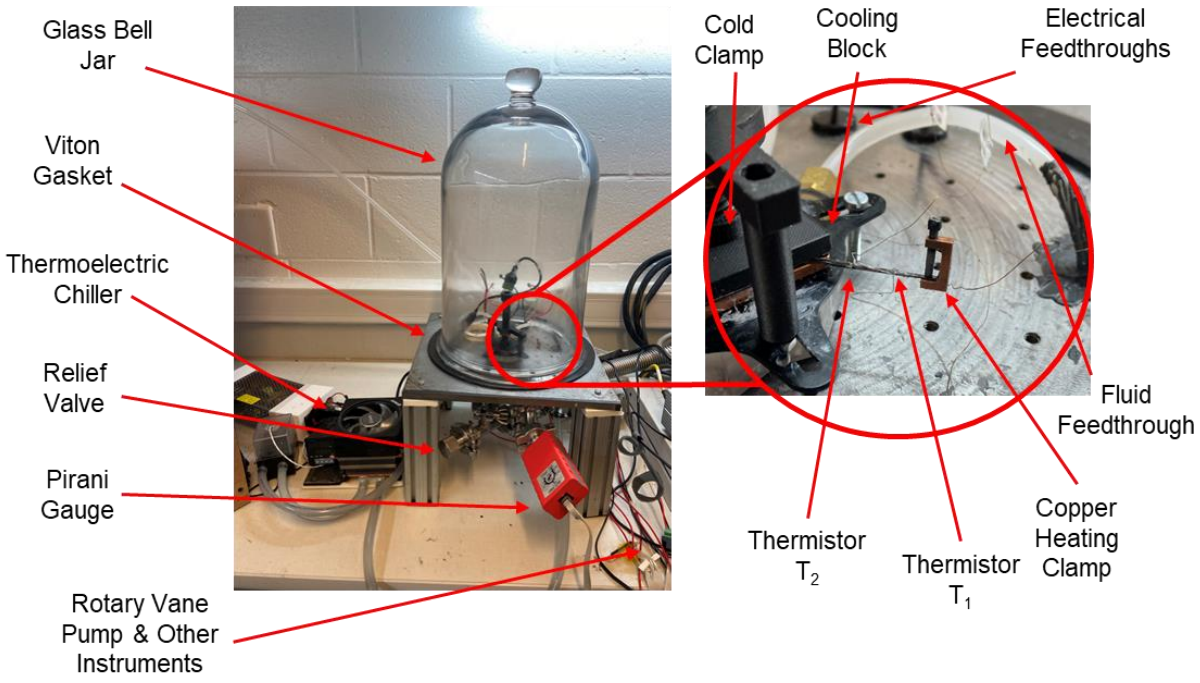

Figure 4-2: Image of fiber thermal conductivity measurement apparatus.

4.1.2 Vacuum Chamber Design

The vacuum chamber was constructed, as seen in Figure 4-3, using a metal plate and a glass bell jar to house the heat flow meter. A bell jar was used as multiple tests were needed to be done and other chamber set ups using ISO or CF fixtures do not allow for quick replacement of samples inside the set-up. Electrical and fluid feedthroughs were used to measure and control the thermistor probes for the heat flow meter, and to cool the copper water block. All mating surfaces were polished and checked for micro scratches, to ensure there were no leakages that could harm the quality of the vacuum. Vacuum was achieved using a rotary vane pump (Edwards V5), this pump was used as it can create a vacuum in the 10^{-3} mbar range. A Pirani gauge (EDWARDS APG-L-NW16) was used to measure the vacuum within the chamber. Outgassing was minimized by thoroughly cleaning and heating up the inner surfaces of the chamber to remove any contaminants. Measurements only took place once the chamber had reached $2\,x\,10^{-3}$ mbar for consistency of measurements. It was determined that a vacuum of $2\,x\,10^{-3}$

mbar is required as at this level of vacuum, thermal conductivity of air is lowered to 4% of what the thermal conductivity at atmospheric pressure (0.0011 W/mK) [136]. 10^{-3} mbar was chosen as between 1 and 10^{-3} mbar, the thermal conductivity decreases significantly (100% to 4% of air at atmospheric pressure), however this decrease plateaus and from 10^{-3} to 10^{-5} mbar (4% to 0.1%). Reducing the vacuum any further would require for a much more complex design involving a turbo or molecular pump with higher rated fittings, for a marginal decrease in heat loss. The vacuum of 10^{-3} mbar was also found to be in the same range for tests done by other researchers such as May et al., Wang et al., and fuji et al. among others [128], [135], [137].

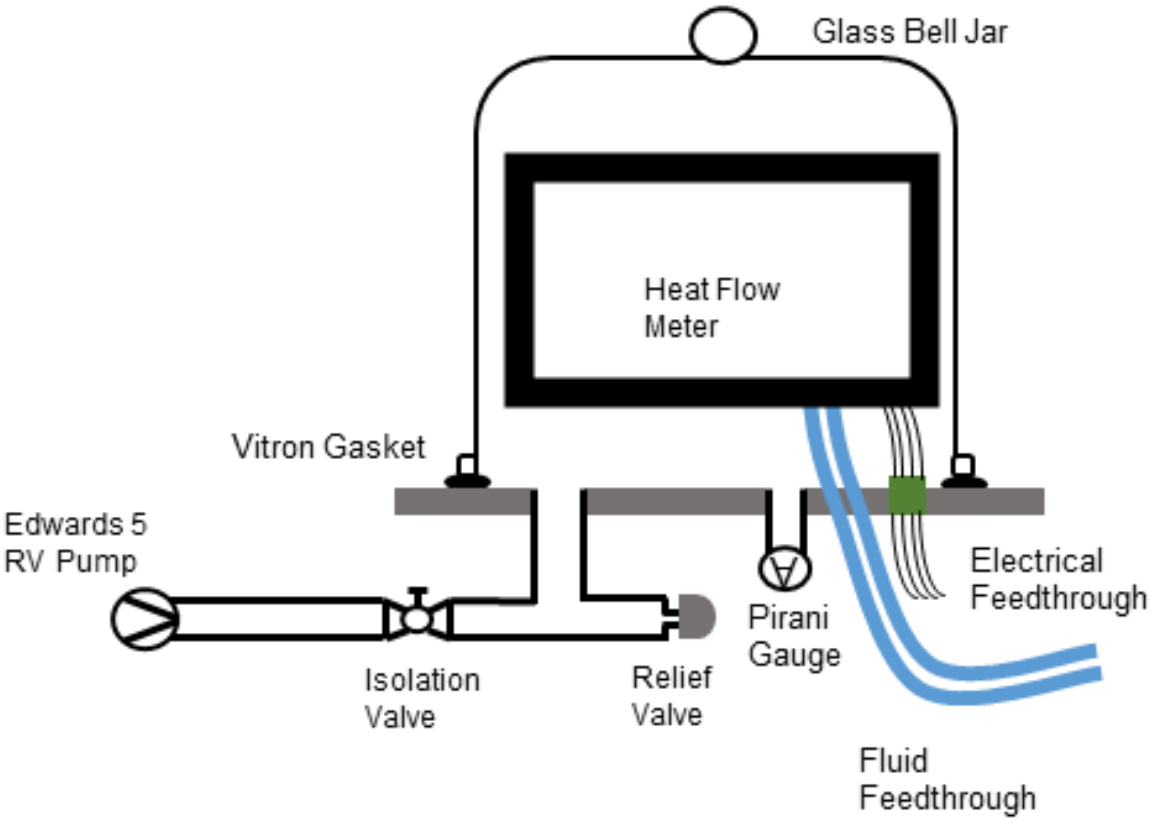

Figure 4-3: Diagram of the vacuum chamber constructed.

4.1.3 Uncertainty Analysis and Calibration

To measure the thermal conductivity of the samples, power is applied to the hot clamp thermistor. As the sample is heated, a temperature gradient is measured, as visualized in Figure

4-1. The length between the thermistors was measured using a vernier caliper, and the cross-sectional area was determined using the diameter of a single fiber which was then multiplied by the number of fibers (approximately 2000) to find the total cross-sectional area. 2000 fibers was an accurate estimation, as when the measurement was done with a tow of CF that had not been modified, the original thermal conductivity of 765 W/mK was measured.

The measured temperature values were used to solve for the resistance of the sample in equation (4-1), which was then used to find thermal conductivity k of the fibers calculated as:

$$k_f = \frac{\mathrm{L}}{\left(R_{Sample}\right)\mathrm{A_f}} \tag{4-2}$$

where L is the length between thermistors, T_1 and T_2 are the temperatures for the two thermistors placed on the samples, Q_{input} is the electrical power applied to the heating clamp, which was measured through the current and voltage measured with the Source Meter (Q=VI), and A_f is the cross-sectional area of the conducting fibers.

Table 4-1: Uncertainty error values for testing apparatus.

Parameter	Symbol	Uncertainty	Measurement Technique
Voltage, V	σ_V	± 0.02%	Keithley 2400 SourceMeter
Current, I	σ_I	± 0.02%	Keithley 2400 SourceMeter
Sample Length, L	σ_l	± 1 mm	Vernier Caliper
Fiber Diameter, d_f	σ_{d_f}	± 0.5 µm	[138]
Temperature Difference, ΔT	$\sigma_{T_{1\&2}}$	± 0.02 K	Lakeshore 370 AC Resistance Bridge

As stated before, the two thermistors had an uncertainty of 0.02 K after calibration, with the Lakeshore model 370 being used to measure the resistances having an accuracy 0.03%. This

calibration as achieved through inserting the thermistors prior to testing into a temperature-controlled environment with an accurate RTD (5606 Full Immersion PRT, Fluke). Resistance readings of the thermistors were recorded along with the temperature reading shown by the RTD at 10°C, 20°C, and 30°C, these resistance readings were then used to solve for the Steinhart-Hart coefficients which bound temperature values to resistance readings [139].

The uncertainty of the power applied was determined by the Sourcemeter uncertainty for voltage and current, both being 0.02%. The individual fiber diameters were identified by the manufacturer to be 11 μm, however, Naito et al. showed the same fibers were found to have and uncertainty of approximately 0.5 μm [138]. The number of fibers in each tow was based on the properties given by the manufacturer at 2000 fibers. Image processing techniques used previously, showed good adherence between theoretical CF volume in a tow, based on 2000 fibers and 11 μm diameter, and experimentally determined CF volume [140]. Error propagation was done with values found in Table 4-1, to determine relative measurement uncertainty in equation (4-3) [141]. On average, this was found to give CF samples a relative uncertainty of around 8%.

$$\frac{\sigma_k}{k} = \sqrt{\left(\frac{\sigma_V}{V}\right)^2 + \left(\frac{\sigma_I}{I}\right)^2 + \left(\frac{\sigma_L}{L}\right)^2 + \left(2\frac{\sigma_{d_f}}{d_f}\right)^2 + \left(\frac{\sqrt{{\sigma_{T_1}}^2 + {\sigma_{T_2}}^2}}{d_T}\right)^2} \tag{4-3}$$

Equation (4-3) shows how the error propagates, with V, I, L, d_f and d_T being the values for voltage, current, length between thermistors, individual fiber diameter, and temperature difference respectively and the corresponding σ being the measurement uncertainty for that parameter from Table 4-1. K and σ_k were the measured thermal conductivity and the uncertainty of the thermal conductivity for the samples, and all subsequent graphs in this thesis use the measurement uncertainty for the error bars.

4.1.2 Heat Loss Calibration

The quality of the vacuum induced in the testing apparatus does not eliminate all lateral heat loss, a miniscule amount of convection and radiation will occur, which establishes the need for heat loss calibration. In numerical and analytical modelling done, it was found that the large surface area of the copper clamp will result in the heat loss. To eliminate heat loss from the copper clamp, testing was done in which the copper clamp was suspended within the vacuum with power being applied to the hot thermistor. A second thermistor measures the ambient temperature within the vacuum chamber. A third thermistor was attached to the surface of the copper clamp as resistances between the hot thermistor and the surface of the copper clamp meant that hot thermistor temperature was not an accurate representation of surface temperatures.

The amount of heat power lost was measured with respect to the temperature difference of the surface and atmospheric temperatures, to create equation (4-4) representing heat loss at different surface temperatures. The calculated lost power was then subtracted from the power input to create an accurate representation of heat power entering the sample. For most samples this heat loss varied between 25%-35%.

$$\dot{Q}_{Loss} = 0.0006129(T_{Surface} - T_{\infty}) \tag{4-4}$$

As stated, heat loss from the sample itself was found to be negligible due to the small surface area of tested samples. When analytically calculating the heat loss from lateral radiation away from the sample using the Stefan-Boltzmann law, the amount of power lost was below 1%. Testing was also done to validate the negligible thermal radiation from the sample, by testing two different copper wires of same diameter, length, and thermal conductivity, but with different emissivity's. One sample was prepared with a light coating of black spray paint, to give it a high emissivity, the second samples surface was kept the same, as copper has a low emissivity (emissivity of 0.05). Both samples had near identical (within the range of uncertainty for samples)

thermal conductivities. Convection from the samples was also found to be negligible due to the short sample lengths and low temperature difference across the sample.

4.2 Experimental Validation

The accuracy of the thermal conductivity test rig was verified, by measuring the thermal conductivities of different metal wires with known thermal conductivities over a range of input powers. Figure 4-4 shows the measured thermal conductivities of a 28 AWG Copper 110 wire, an 18 AWG Aluminum 1100 wire, and a 1.5 mm diameter 99% tin solder wire as a function of heater input power. The average measured thermal conductivity of the aluminum and tin samples was 214.7 W/mK and 64.8 W/mK respectively, which agrees well with the accepted values of 220 W/mK and 66 W/mK respectively, the measured values being only 2.45% and 1.9% off of the known values. For the coper wire sample, the average measured thermal conductivity was 409.8 W/mK which is about 5% higher than the accepted value 390 W/mK.

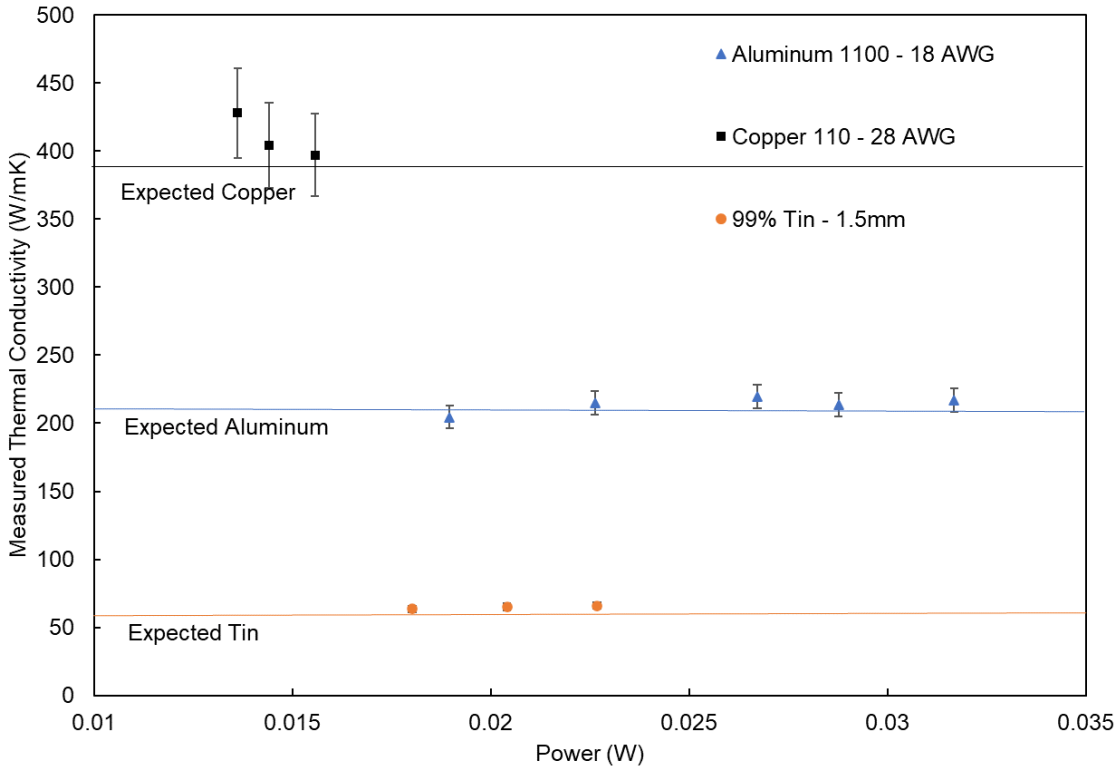

Figure 4-4: Measured thermal conductivity of varying metal wires.

The uncertainty of the measurement apparatus derives from the fact that it is a custom-made heat flow meter, therefore, its repeatability needs to be determined. Through testing of the same material multiple times and showing that the test rig can attain the correct known thermal conductivity every time, the uncertainty in testing can be diminished. Repeatability testing was done by resetting the samples by replacing the aluminum with another piece of the same exact wire, different distances between the thermistors were used to show length independence and identical power input of approximately 35 mW was used. Test results are presented of thermal conductivity for 1100 aluminum, as seen in Figure 4-5.

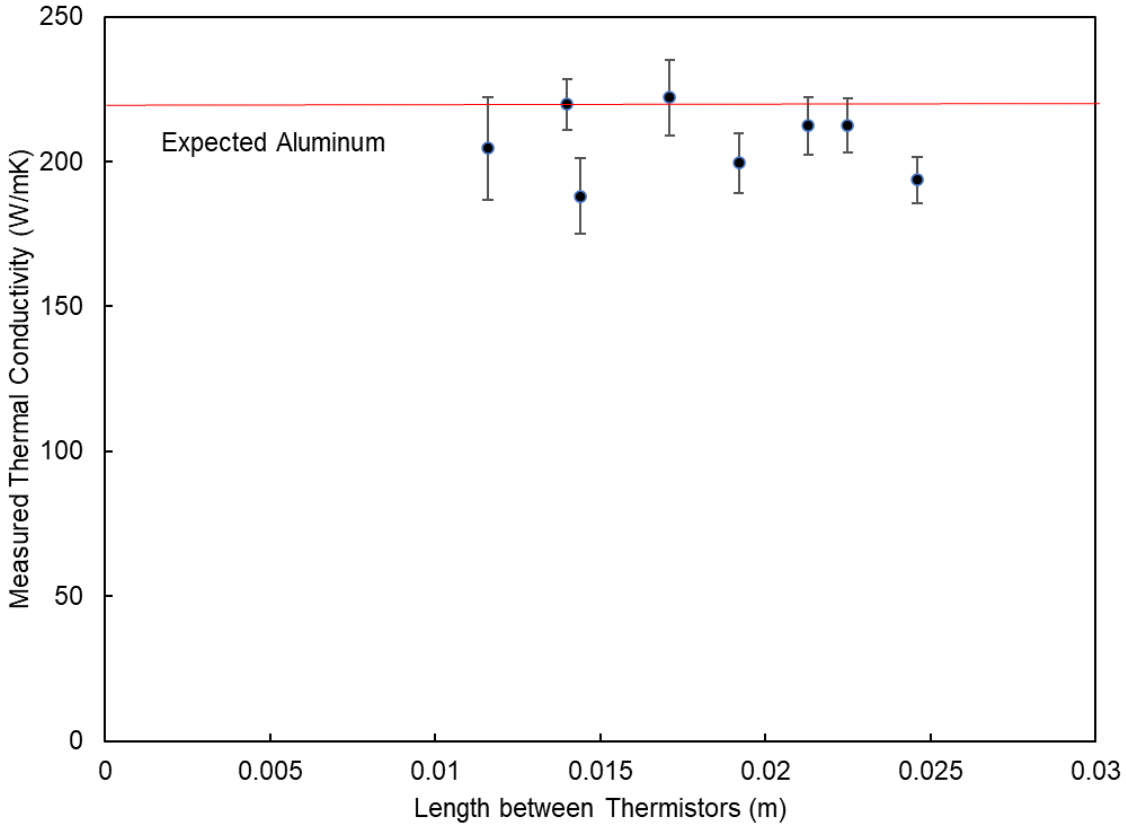

Figure 4-5: Repeatability testing of thermal conductivity of Aluminum 1100 with varying length between thermistors, red line indicates expected thermal conductivity of samples.

Length between thermistors varied from 11.6 mm to 25 mm, the calculated thermal conductivity was found to be independent based on the absolute measured length. Samples were

compared to the known thermal conductivity of the 1100 aluminum, a mean thermal conductivity of 206 W/mK and a standard deviation of 11.42 W/mK was measured. The lowest accuracy was found in a sample that was off by 32 W/mK form the expected 220 W/mK, which is an error of 14.4%. In the future one-way ANOVA tests could be used to further prove the accuracy and validity of the testing apparatus build confidence in the results, however due to the length taken for each measurement (around 3 hours per measurement), it was deemed impractical for the study.

4.3 Conclusion

In this chapter, a tow thermal conductivity measurement apparatus was designed, fabricated, and validated to be used in measuring the thermal conductivity of 3D printed PCF tows. The apparatus uses a heat flow meter approach to send heat power through the samples, with thermistors placed along the sample to measure the thermal conductivity of the sample being tested. The heat flow meter was placed within a vacuum chamber, reducing the heat lost to the surroundings of the sample, resulting in a more accurate measurement. The validate the measurement apparatus, metal wires with known material compositions and thermal conductivities were experimented with. Copper, Aluminum, and Tin wire had their thermal conductivities measured with varying input powers and thermistor distance. The apparatus was validated and was deemed to be usable for measurement of thermal conductivity of PCF tows.

Chapter 5 Characterization of Carbon Fiber Breakage

The pitch carbon fibers initially explored in Chapter 3 (K1352U, K1392U, and K13D2U manufactured by Mitsubishi Chemicals) are continuous carbon fibers with some of the highest thermal conductivities seen in the industry. Of these, K13D2U has the highest thermal conductivity (765 W/mK), however this grade of PCF also has the highest tensile modulus and is extremely brittle. For the grades with lower thermal conductivity (92U and 52U), lower tensile modulus is reported, and the thermal conductivity results from Chapter 3 suggest K1352U and K1392U grades to be far less brittle than the K13D2U samples. The occurrence of breakage in 3D printed samples lowers the overall effective thermal conductivity, which was seen in initial tests and prints. The issue of breakage can be circumvented by increasing the volume fraction of the CF filler in sample. Though increasing filler content in samples increases the thermal conductivity, it is unappealing as it increases the cost and weight of the samples. Aluminum alloys such as 6061, 6062, and 6063 have thermal conductivities of approximately 150 W/mK; to be on par, a fiber volume fraction of 20% of K13D2U is needed assuming no fiber breakage occurs while printing. Breakage that occurs which yields in only half of the expected thermal conductivity would require that double the CF would be needed to attain required thermal conductivity, with the PCF having almost double the density and many times the cost of the polymer matrix (PLA), this would not be economical to use in this state.

Therefore, the objective of this Chapter is to characterize the effect of several printing parameters on thermal conductivity of the resultant fiber to understand the mechanism of breakage during the fabrication process. By understanding the causes of breakage, the 3D printing process can be improved and refined to minimize fiber breakage. The initial coating process was suspected of causing breakage; therefore, the first step will be to determine if the coating process causes any reduction in the thermal conductivity of the PCF. In the 3D printing process, the printing speed has shown to be an important factor with its effects on continuous

fiber composites studied in great depth [142]–[144]. Generally, an increase in printing speed is known to cause more errors in layer adhesion and X-Y accuracy whilst causing the continuous fibers to cool down much faster, which adds stress on the fibers. Another mechanism of breakage to be examined is raster spacing, when printing continuous PAN CF composites, the spacing between rasters is generally ignored, with more emphasis going into examining the voids formed by the continuous fiber rasters, and looking into raster orientation and its effects [145], [146]. When printing continuous pitch carbon fiber, it was noted and observed that although the PCF filament had a diameter of approximately 0.8 mm, when rasters were laid next to one another at 1 mm intervals, the layer would become overcrowded and disorganized, resulting in breakage.

Finally, although the angle of the nozzle to the printing bed is suspected to be a large factor in fiber breakage, it was not feasible to develop a system for varying nozzle angle on the setup described in Chapter 3. Chapter 6 will look at nozzle development for a new printing system and the effects of angle of extrusion in terms of fiber breakage.

5.1 Characterization Methods

As discussed, PCF coating, samples printing speed, and raster spacing are thought to be the most important factors when dealing with conventional printing parameters, each one of these methods to determine the amount of breakage occurring. The testing plan is shown in Table 5-1, in which each one of these parameters will have a combination of tests done to identify and express the levels of breakage happening due to the process.

The PCF coating technique will have coated and uncoated samples compared using the single tow thermal conductivity technique developed in the previous Chapter. By comparing the measured thermal conductivities, breakage could be observed if occurring due to the coating process. This process was also done for varying print speeds, as printed tows of CF can be tested equally well once the ends of the sample were burnt off.

To further analyze fiber breakage, imaging methods were used to qualitatively explore the breakage occurring at various steps during the printing process. Though the thermal conductivity testing will allow for quantitative results, a qualitative look at the fibers would give insight into what the fibers go through after each process of the printing. To Image the fibers through microscopy the PLA and other epoxies around the fibers need to be burned off first. Hu et al. were able to use this technique to identify which stage of printing for FFF 3D printing of PAN carbon fibers caused the most breakage [121]. Using this technique will allow examining of fiber breakage within a tow due to fiber coating and 3D printing processes.

Thermal imaging was also used to better understand how the thermal variations were experienced by the samples. Samples were viewed with an FLIR A6700 MWIR infrared camera to analyze the temperature of the PCF as they leave the extruder nozzle. Unlike conventional FFF printers, the PCF extruder has no stage in which the molten polymers are mixed and passed through a smaller diameter nozzle; instead, the PCF is heated and passed through the extruder heating section. If samples are not heated to a high enough temperature where the polymer has fully melted, the stress caused from the sharp angle at the nozzle could induce breakage.

The process developed by Elkholy et al. was also used for macro 40 mm by 40 mm samples to determine the bulk effective thermal conductivity of samples with varying raster spacing [112], [114].

Table 5-1: Techniques used to characterize fiber breakage occurring due to the selected processes.

Process	**Characterization Methods**
Pitch Carbon Fiber Coating	- Single Tow Thermal Conductivity - Microscopy Imaging
Varying Print Speed	- Single Tow Thermal Conductivity - Microscopy Imaging - Thermal Imaging
Raster Spacing	- Macro Sample Thermal Conductivity - Microscopy Imaging

5.2 Effects of the Fiber Coating Process

For all three grades of CF examined, uncoated and coated samples had their thermal conductivities measured to evaluate if the coating process (described above) caused any breakage. K13D2U, K1392U, and K1352U samples of 60 mm length had their thermal conductivities measured before and after passing through the polymer bath, the thermal conductivity measured was then compared to manufacturer specifications. Samples were measured using the heat flow meter developed and discussed in Chapter 4. Coated samples had adequate rigidity to be suspended midair for measurement, whilst uncoated tows were adhered to a polymer bar. The ends of the samples were melted off to ensure the heating clamp had good contact with the samples, which would decrease heat excursions from the clamp and promote heat flow through the sample. The first measurements were done to understand if, and how, the coating process affects breakage of fibers. The fiber coating process is a necessary process that the fibers must go through before being extruded. For the three grades of carbon fiber, thermal conductivity was measured after the fibers were coated, which were then compared to the original

uncoated fibers. Figure 5-1 shows that the samples incur no breakage because of the coating, with samples showing nearly identical thermal conductivities prior to and after the coating process, within the uncertainty error based on error propagation.

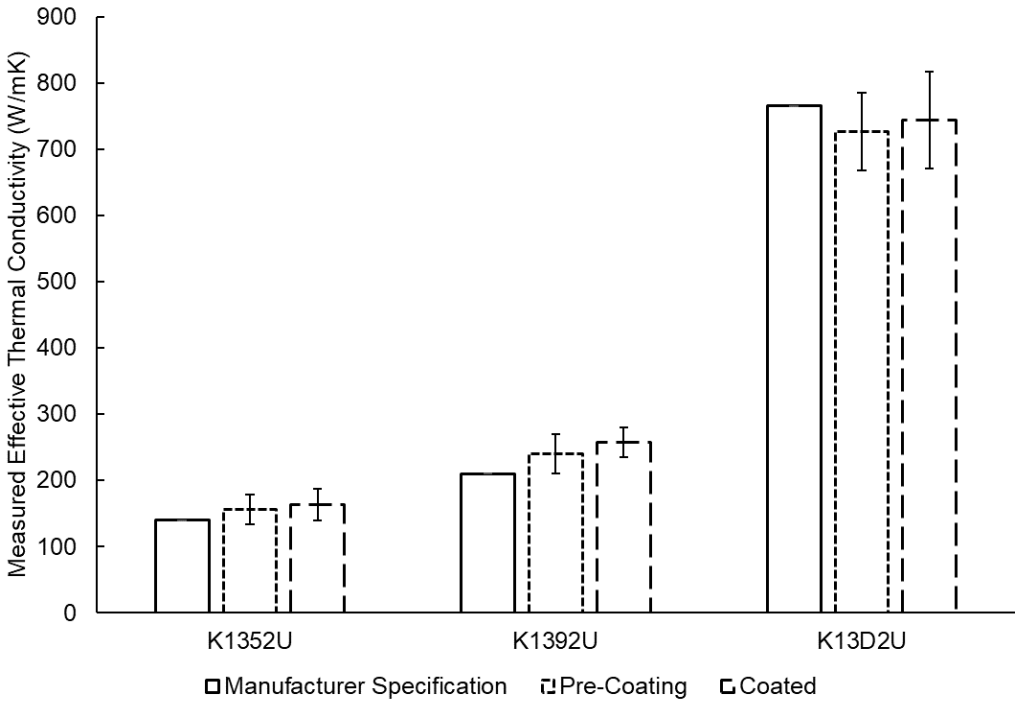

Figure 5-1: Measured thermal conductivity of varying grades of pitch carbon fiber before and after the polymer coating process, thermal conductivity prior to coating was provided by manufacturer.

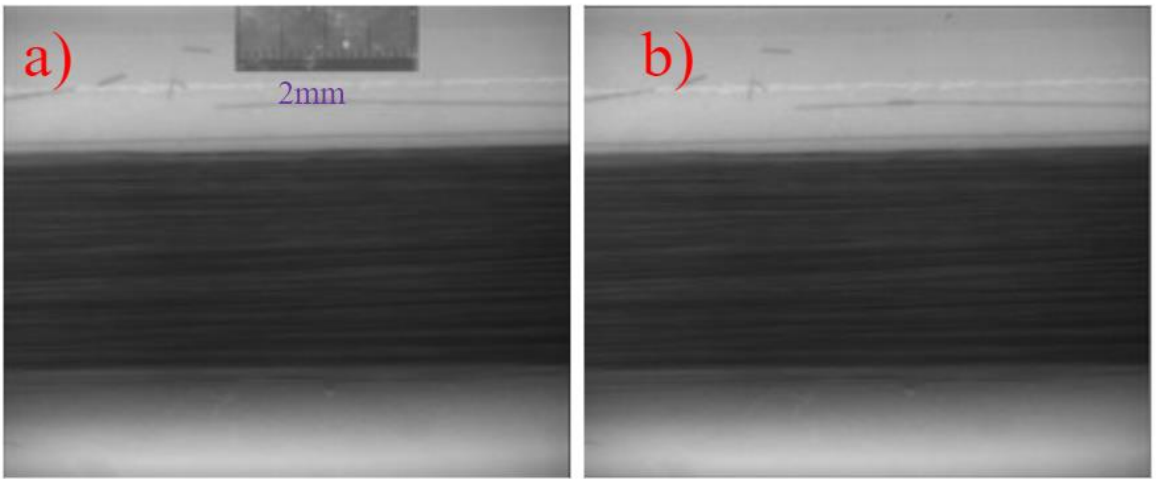

Figure 5-2: Microscope images taken of K13D2U PCF after burning out the polymer matrices, a) uncoated samples directly from the roll, b) fiber filament that had been coated in PLA polymer.

Microscope images shown in Figure 5-2 compare the fiber integrity and quality before and after the coating, showing almost no difference from one sample to the other. The thermal conductivity measurements along with the microscopy imaging results show that no breakage happens because of the coating process.

5.3 Effect of Printing Speed

The second round of testing involved examining how printing speed affects the integrity of the carbon fibers. Initially, print speed settings were chosen based on printing parameters found in commercially available products. The extrusion of the PLA polymer was done at 800 mm/min, whilst for the PCF the printing speed was chosen to be 3000 mm/min. As the PCF does not have a liquefaction and mixing stage, it was believed that printing at the average printing speed for a Prusa i3 Mk2 would be satisfactory. Print speed for the PLA polymer was chosen to be 800 mm/min to promote well structured layers of polymer. Single tows of CF of the three grades were prepared by printing at speeds between 800 mm/min and 3000 mm/min to see if lowering the speeds would be beneficial in lowering breakage, all printing was done with the nozzle and bed being 215°C and 60°C respectively. Samples with the length of 100 mm were printed, 20 mm from either end were cut off to eliminate any effects from the print start and end.

Prior to measuring thermal conductivity of samples printed at varying printing speeds, repeatability for the printing process was developed by printing several CF tows at the same speed and measuring their thermal conductivity. Samples of K13D2U were printed at 1500 mm/min and their thermal conductivity was measured as seen in Figure 5-3. On average the thermal conductivity of the samples 478.8 W/mK and the standard deviation of the samples were 19.27 W/mK. Similarly to the repeatability testing done for the metal wires in the previous section, a one way ANOVA test should be done to improve confidence for the printing process, however due to the long testing times, this was not done.

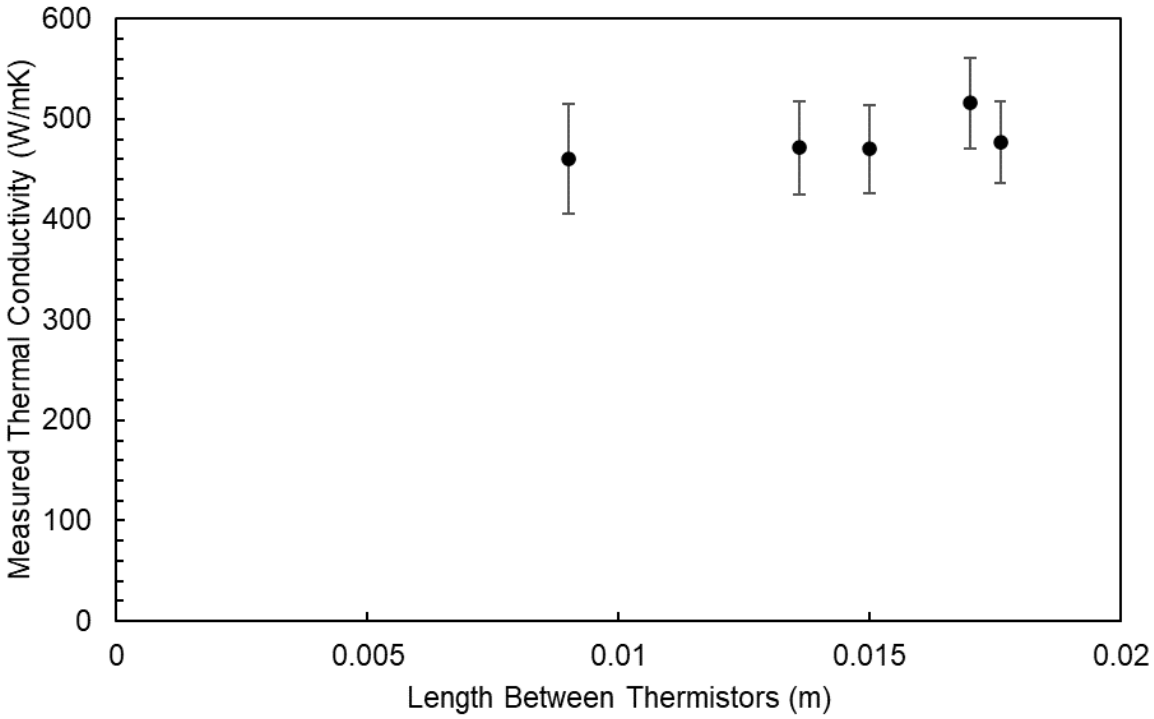

Figure 5-3: Thermal conductivity of K13D2U tows printed at 1500 mm/min.

Thermal conductivity of the different grades of CF were measured and presented in Figure 5-4. For lower conductivity samples, only three speeds were tested due to a lack of breakage, whilst for the K13D2U samples, two additional speeds were examined. Measurements for the K13D2U samples show that at speeds between 800 mm/min to 2500 mm/min little to no change in the amount of breakage is observed, as measured thermal conductivity is in the range of 448.3 W/mK to 479.9 W/mK, with average measurement uncertainty of 8.5 % to 11.9%. An outlier for K13D2U can be seen at 3000 mm/min printing speed, in which the thermal conductivity decreases greatly, with the tow thermal conductivity measuring at only 110.9 W/mK. This outlier was found to be repeatable in both thermal conductivity measurements and microscope images, which was determined to be a product of an error in the printer's software. It is believed that acceleration profile within the printer firmware follows a different profile after the print speed is set to 3000 mm/min: this harsher acceleration profile results in greater breakage than is seen at lower speeds.

Specifically, it is observed that the PID of the 3D printer that controls the speed overshoots the desired target, resulting in an oscillation of the speed around to the desired speed set in the Gcode. Samples of K1392U which have lower conductivity and tensile modulus were found to be mostly intact in terms of thermal conductivity. The outlier from the acceleration profile is also seen to a lesser extent, mainly due to the CF being less brittle. Samples of K1352U were seen to have no change in thermal conductivity at any printing speed, this is expected due to the elasticity of this CF (the outlier at 3000 mm/min is not seen). Further printing with the K1352U samples would benefit from a fiber cutting mechanism, as it was found often, that the whipsaw motion of the extruder to break off fibers occasionally does not yield in a clean break.

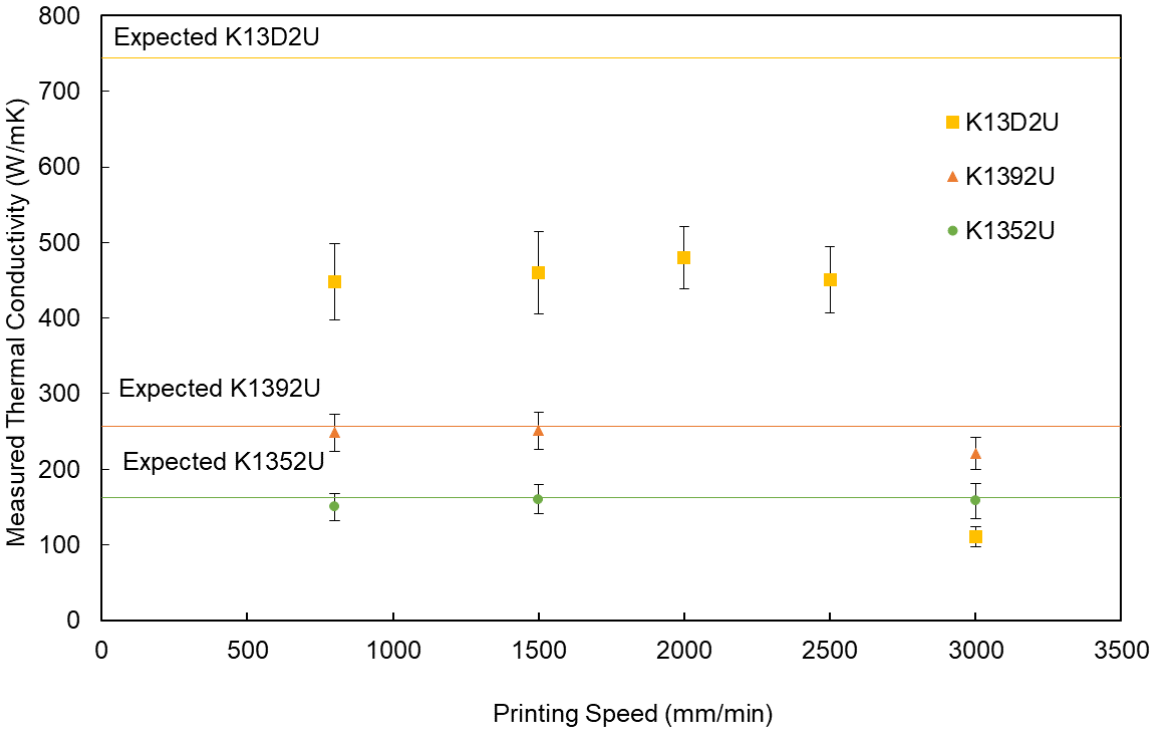

Figure 5-4: Measured thermal conductivity of printed tows of K13D2U, K1392U, and K1352U, colour of lines corresponds to the expected thermal conductivity of the fibers for each grade.

One interesting aspect seen in these tests, specifically for the K1352U and K1392U, is that the thermal conductivity measured does not correspond to the measured thermal conductivity

of full samples printed and tested previously. This indicates that for the lower conductivity samples, the catalyst of breakage is dictated by the macro-interactions happening between layers of PCF and polymer, rather than the micro-interactions between the fibers and extruder. Inversely, the large amount of breakage seen for the K13D2U samples indicate that a large portion of the breakage is happening due to the micro-interactions in the nozzle, most likely hypothesized to be an aspect of the nozzles angle to the bed.

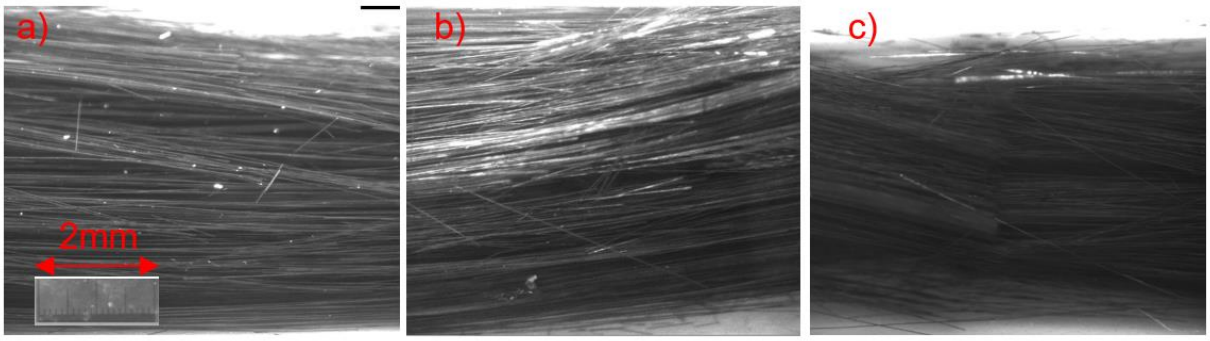

Figure 5-5: Samples of K13D2U that have been printed at various speeds and had their polymer matrices burned off, samples were printed at a) 800 mm/min, b) 1500 mm/min, and c) 3000 mm/min.

Microscope images show similar results to thermal conductivity measurements, Figure 5-5 presents the average sections of printed samples of K13D2U CF at multiple speeds. Samples printed at 800 mm/min and 1500 mm/min show similar amounts of breakage as expected, whilst those printed at 3000 mm/min clearly show the outlier breakage, with most of the fibers being destroyed and turned into long/short fibers.

5.3.1 Printing Temperature Analysis

Print extrusion temperature is generally an important print parameter to inspect, for most polymer extrusion processes, large diameter filaments enter a liquefier stage, meltdown, and mix, and then are extruded out of a smaller diameter nozzle. When looking at continuous fiber extrusion, there is no liquefier stage as it is desired for the polymer matrix of the fibers to melt

without affecting the continuity of the fibers. As the polymer used for layer and raster adhesion becomes molten, the rigidity of the filament will decrease allowing for the PCF to melt at the nozzle. However, as can be seen in Figure 5-6, the temperature of the extruded filament drops significantly after the printing has begun. This is because before the extrusion has begun, the filament remains in the heated nozzle, reaching a steady state temperature close to the temperature of the nozzle. Once extrusion has begun, the process turns into transient heating, even if the extrusion speed of the filament is 800 mm/min. This means that any point along the filament is only heated for a maximum of 1.5 seconds. Due to the transient heating process within the extruder, the filament is heated for a time dependent on the printing speed and then extruded; hence, the temperature drop is higher in faster printing speeds. The nozzle was viewed with a FLIR A6700 MWIR infrared camera to analyze the temperature of the PCF as it left the extruder nozzle, print speed was set to 1500 mm/min.

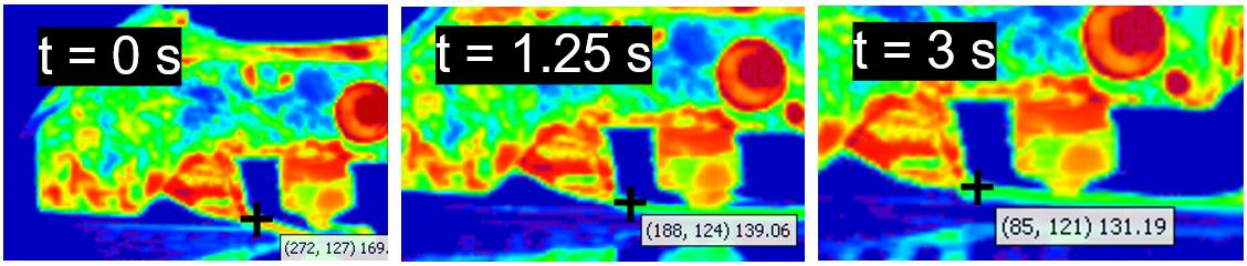

Figure 5-6: Thermal images taken with a FLIR A6700 MWIR infrared camera of the pitch carbon fiber printing process, third number in the white box indicates temperature of filament as it leaves the nozzle, in degrees Celsius.

Analyzing Figure 5-6, shows that the temperature of the extruded PCF filament drops by 40 °C to around 130 °C, three seconds into the printing process. When printing with PLA polymer it is optimal to print at temperatures between 180 °C and 220 °C. To see if this temperature drop has any bearing on breakage, microscopy was done to inspect samples for their entire lengths.

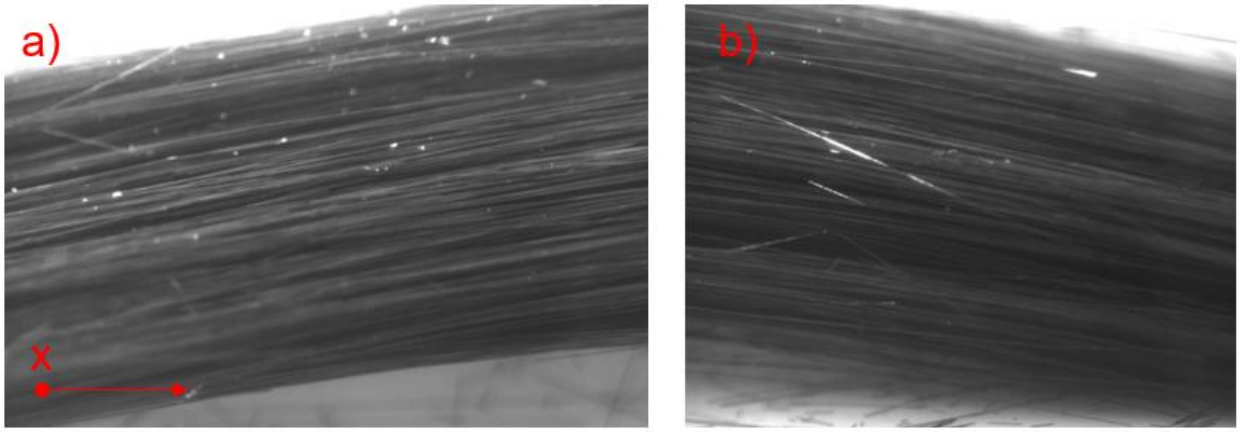

Figure 5-7: Images of carbon fiber printed at 800 mm/min, a) fiber integrity at x = 20mm b) x = 60 mm.

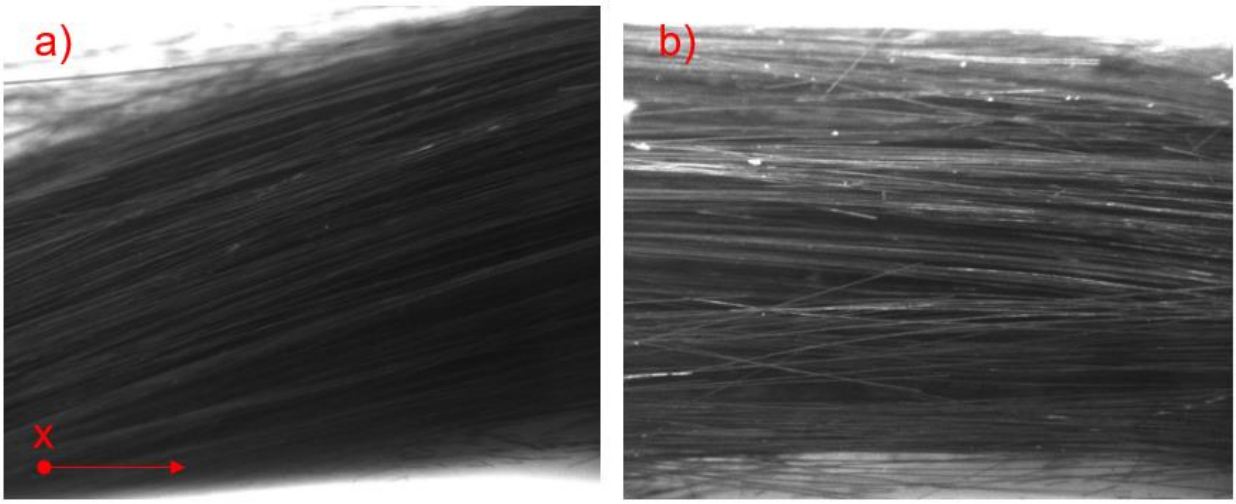

Figure 5-8: Images of carbon fiber printed at 1500 mm/min, a) fiber integrity at x = 20mm b) x = 60 mm.

100 mm long samples were printed at 800 mm/min and 1500 mm/min. 20 mm of the sample was cut off from either end to neglect the effects of the cutting mechanism. The samples had their polymer matrices burned off; the samples were inspected at 2.5X zoom. Figure 5-7 and Figure 5-8 shows images of PCF that have been printed at 800 and 1500 mm/min and had their polymers burned off. The images show the quality of fibers at the beginning of printing compared to at the end of printing. Figure 5-7a and Figure 5-8a show fibers at 20 mm into the extrusion process, while Figure 5-7b and Figure 5-8b show the integrity of fibers approximately 60 mm into

the extrusion. Though samples printed at 800 mm/min do not show much change in quality or breakage of fibers, samples printed using the same printing parameters as those for Figure 5-6, clearly show that far more breakage occurs at 60 mm into printing. Further imaging showed that this increase in breakage along the length was repeatable. Samples printed at 3000 mm/min did not show a visible increase in breakage due to the high amount of breakage along the entire sample. Longer samples printed in the future can better show how the extended printing duration harms fiber quality.

5.4 Effect of Raster Spacing

Full samples, with the cross-sectional area of 1600 mm^2, were also manufactured for the K13D2U samples, and had their thermal conductivities measured. Full samples were manufactured mainly with the purpose of understanding the effects of how the polymer and PCF layers interact with one another. Samples were printed at different volume fractions, which was done by adjusting the ratio of PLA polymer layers to PCF layers. During previous printing, it was observed that the PCF rasters, when printed at 1 mm intervals, caused overcrowding and misalignment in the layers. Although the PCF filament has a diameter of 0.8 mm, when printed, the carbon fibers are pressed down into a rectangular shape, with a width greater than 0.8 mm. The raster spacing was increased from every 1 mm to every 1.5 mm to understand whether the raster spacing is a catalyst for fiber breakage.

Microscope images were also taken for a single layer of PCF layer, show in Figure 5-9. These images were the main instigator in examining the effect of raster spacing. Figure 5-9a and b clearly show large amounts of breakage, which is hypothesized to occur mainly because of the raster spacing; the rasters being spaced too closely to one another, resulted in the nozzle damaging the new raster while it is laid next to the previously printed raster. Fiber damage can also be seen from the rasters overcrowding, which has led to carbon fibers being lifted. When the PLA layer passes over the PCF to print a purely polymer layer further breakage is caused.

Thermal conductivity of full samples with a length and width of 40 mm and 25 mm thick were measured, in which the fibers were oriented to promote heat flow in the thickness direction. The samples had varying volume fractions to compare to the parallel model.

Figure 5-9: Images of a layer of pitch carbon fiber printed at a raster spacing 1 mm, the samples were printed at a) 800 mm/min, b) 1500 mm/min, and c) 3000 mm/min.

The method of testing involved the usage of a guarded heat flow meter developed in the TF-lab, previously discussed in Chapter 3 by Elkholy et al. [114]. The guarded heat flow meter, seen in Figure 3-5, applies a controlled heating load onto the bottom of the sample, where the heat travels through the sample to the cold block on top of the samples. Two holes are created in the sample in line with the heat flow along the sample, in which high calibrated RTD's are placed to measure the temperature gradient along the sample. Fourier's law was used to back out effective thermal conductivity values of the samples and graphed in Figure 5-10.

Samples that had the PCF extruded with greater raster spacing were found to have thermal conductivities of 18.51, 20.70, and 32.09 W/mK for fiber volume fractions of 5.5%, 6.4%, and 8.0% respectively, as seen in Figure 5-10. These samples were shown to have a large amount of breakage, compared to the thermal conductivity that is expected from the rule of mixtures parallel model; however, the amount of breakage is similar to that found in single raster prints, as can be seen in Figure 5-11. Samples printed using previously used raster width again showed a great amount of breakage, with the thermal conductivity values around 19.45, 22.60, and 36.96 W/mK at fiber volume fractions of 7.6%, 9.5%, and 11.7% respectively.

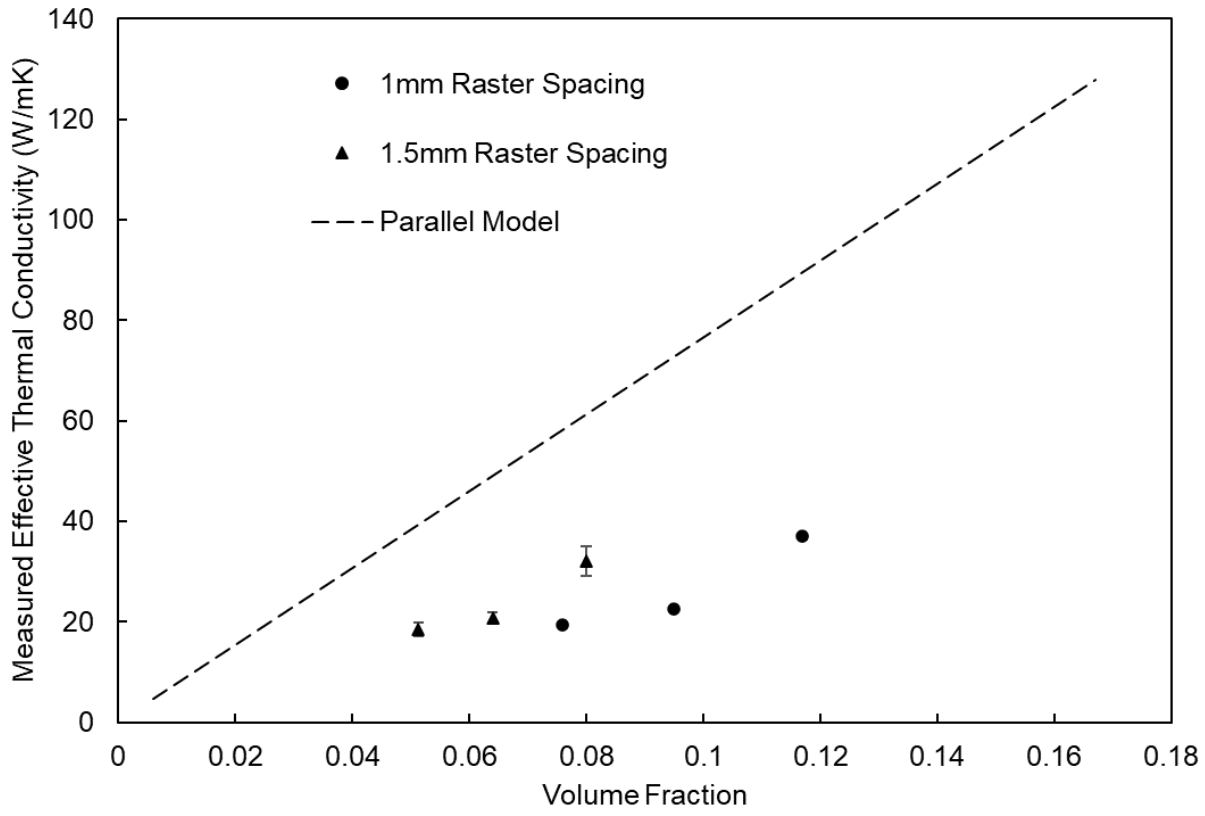

Figure 5-10: Comparison of the measured effective conductivity for composite samples manufactured (K13D2U and PLA) with 1 mm and 1.5 mm raster spacing.

Around 10% less breakage is happening with the new printing parameters as seen in Figure 5-10. Furthermore, the new samples have breakage like the measured single raster breakage seen in Figure 5-4. Single rasters of K13D2U printed at 800 mm/min at the same temperatures had breakage of around 45%. This indicates that the breakage found now is based on only the micro-interactions within the nozzle, such as printing angle and internal roughness of the hotend, rather than the interactions between layers and rasters as they are printed.

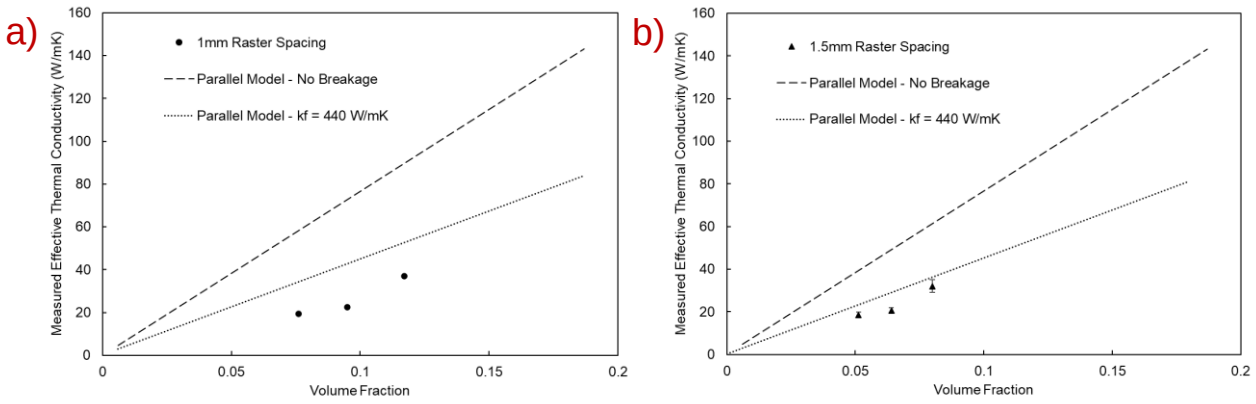

Figure 5-11: Comparison of measured thermal conductivity of a) 1 mm raster spacing, and b) 1.5 mm raster spacing with respect to the thermal conductivity of fibers, kf, based on measurements in Chapter 4.

5.5 Conclusion

This study has shown that the initial printing process, developed for printing of PCF composites, still needs to be improved to reduce the breakage experienced by the PCF within the extruder. Printing parameters such as speed, extrusion length, raster spacing, extrusion temperature, and breakage mechanism was found to affect print quality, however, results show that most of the breakage is caused by other parameters such as interactions within the nozzle, like friction and nozzle angle to the bed. Print speed was found to affect breakage only when the speeds rose to 3000 mm/min. Print angle is hypothesized to be the origin of most of the breakage the PCF experiences, yet due to the nature of the 3D printing platform, this can not be easily changed or experimented with. Though the question of the cause of the breakage remains, samples with low volume fractions of 8% were printed and shown to have an effective thermal conductivity of 32.09 W/mK, which is significantly higher than any other 3D printed composite investigated in literature [83], [85], [116], [117], [147]. Scanning electron microscope imaging could also be used in the future similarly to the microscope imaging to view the fiber tows more in depth to understand how the individual fibers are being affected.

Chapter 6 Development of Robot CFRP Printer Capabilities

The previous investigations of 3D-printing of continuous PCF composites explored their thermal conductivity and tensile strength. These tested samples were 3D-printed using the K13D2U (Mitsubishi Chemical Corporation) grade of pitch carbon fiber. These studies used the FFF printing setup, where a custom manufactured dual nozzle hot end was used to print a coated PCF filament with the first nozzle, and PLA polymer with the second nozzle. The nozzle used to print the PCF filament was angled to the bed at 45°, as seen in Figure 3-2, to help reduce fiber breakage. However, previous samples were found to have far lower effective thermal conductivities and strength than theoretical models predict with the 3D-printed samples having thermal conductivities on average 55% of what is expected from the parallel rule-of mixture model. It was also discovered that printing parameters such as printing speed, and raster spacing, along with the coating process, had minimal effect on the breakage seen. Therefore, to better understand and mitigate this fiber breakage, a new extruder and printing system was developed. The extruder was designed to print the continuous PCF filaments in various ways that could not be done with the prior extruder, which allowed more in-depth characterization of fiber breakage in terms of thermal conductivity based on these printing methods. This new printing system, along with testing various print angles, will allow for the PCF to be printed in multiple directions, creating composites with multi-directional heat flow paths.

6.1 6-Axis CFRP 3D Printer Design

In previous investigations, the 3D printer used a fixed angle hotend, which resulted in the PCF being extruded at a constant 45° relative to the print bed. The fixed angle limited the printer to only printing unidirectional samples along the x-axis, severely limiting the complexity of printed parts. To overcome these limitations, a new extruder has been designed and fitted on a 6-axis robot arm, which allows the nozzle to be angled freely in any direction and for full articulation of

the nozzle during printing. The larger working surface and high accuracy and repeatability of the robot arm used, will also help in reducing imperfections in printing and creating larger sized components. Other researchers have used 6-axis robotics for 3D printing, the usage of robots with higher degrees of freedom allow for larger print areas, better control of fiber alignment, and more complex geometries [148]. Yao et al. determined that using the greater mobility of the 6-axis robot can result in better print quality due to print scheduling decreasing the amount of stringing [149]. The greater mobility yielded by the robot also helps in accomplishing true 3D prints, rather than the 2.5D printing often found on commercial prints. 2.5D printing is the concept in which planar xy-layers are printed on top of one another. This method causes what is known as the staircase effect and promotes mechanical shearing at the interface between layers. Full 3D printing, as the name suggests, involves creating non-flat planar layers, removing the staircasing effect found in curves. İpekçi and Ekici use a 6-axis robot arm to 3D print CFRP, and successfully print hollow tubes with bends without any staircasing [150]. Hack et al. also developed a novel printing process in which continuous fibers were printed with success in a large volume [151]. Due to the low speeds required when printing the continuous pitch carbon fiber, print times are generally high for printing even the smallest parts. Hack et al. got around the print speed issue by using a process like the tape winding process. Automated fiber placement also generally uses the mobility of robot arms to create parts, the 6-axis of the robot were found to be a good method for aligning fibers in various directions dependent on the use of the part and the stresses it is to experience [64], [65]. Various types of print heads exist for robot 3D printing, with most designs leaning towards the usage of a pellet extruder design, which allows for faster printing with greater material variety [152]. For the purposes of this project, which is to explore the mechanisms of breakage experienced by the PCF composites, a simple filament extruder design was used.

6.1.1 New Extruder Design

The extruder designed for this project is shown in Figure 6-1. The extruder was required: to be able to extrude the continuous PCF filament manufactured using previous techniques, be able to print at various angles, and to avoid clogging of the nozzle. An all metal V6 extruder (E3D-Online) was chosen as the basis for a customized extruder. Although the same heatsink, hot-end, heat-break, heater, and thermistor were used, a new nozzle had to be manufactured as the original extruder nozzle was found to have several incompatibilities with the printing setup. The largest diameter of nozzle provided by the manufacturer is 0.8 mm, at this diameter the PCF filament would experience friction as it passes through the nozzle, although this might improve the heating of the filament. Previous prototypes found that friction at the nozzle led to high amounts of clogging and breakage. The second problem faced by the nozzle is its low profile, causing for the extruder to crash into the printing bed when angling the extruder. The new nozzle was manufactured with these issues in mind, the diameter of the nozzle was set to 2 mm such that in addition to the PCF filament, other sized filaments made in the future could be extruded.

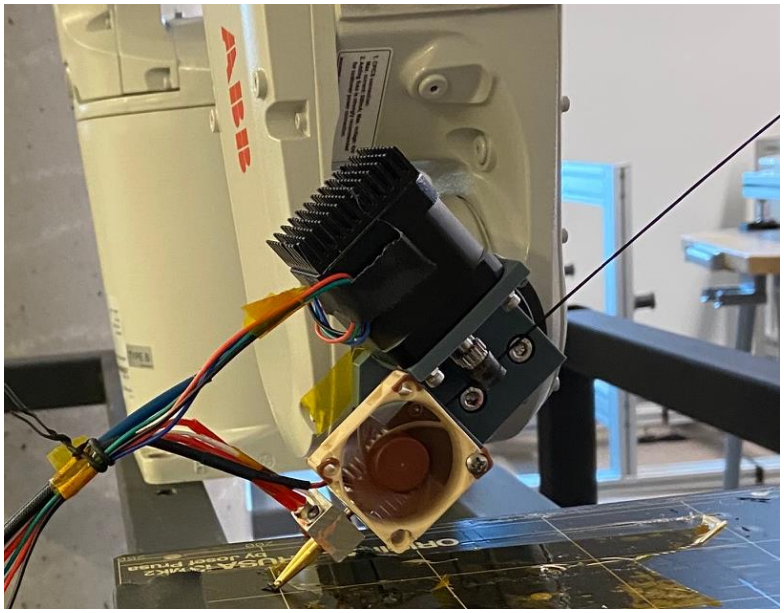

Figure 6-1: Image of new extruder mounted on robot arm, in the 45° orientation.

The nozzle was elongated to allow for the angle between the extruder and normal line from the print bed to go up to 65°. This elongation will help in heating of the filament, as the fiber heating length will be longer than that of the previous extruder. To decrease friction between the filament and extruder walls, the internal walls of the extruder and nozzle were coated with a polytetrafluoroethylene (PTFE) spray. PTFE is a polymer primarily used reducing friction, more commonly known by its commercialized name of Teflon, that has a melting point of 327 °C, allowing for it to be used as a surface coating within the extruder. PTFE has found success in the FFF industry, a tube of PTFE is often inserted within the extruder prior to the liquification stage such that the polymer filament can be guided to it with reduced friction. Replacing the tube with a coating will ideally allow for greater heating of the filament, as the polymer tube acts as a thermal insulator.

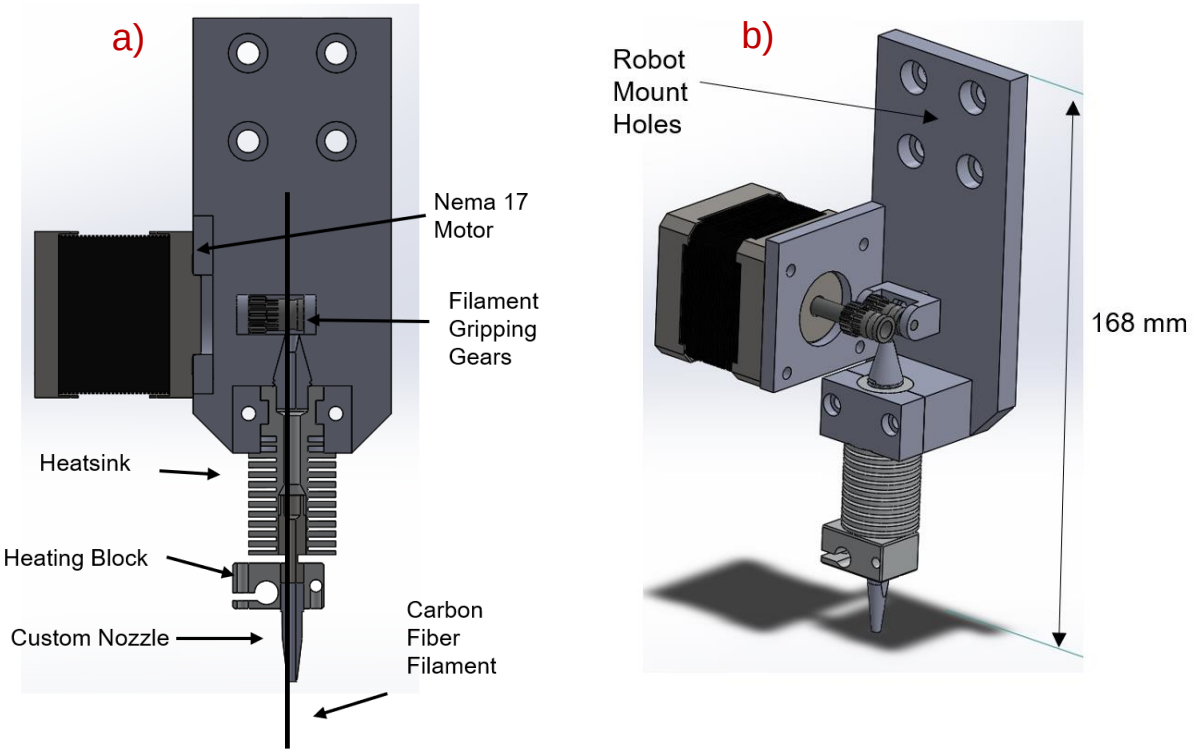

Figure 6-2: CAD diagram of new extruder a) cross sectional, and b) isometric.

Figure 6-2 displays the new extruder, in addition to the V6 extruder, an additional filament guide was made to make sure filaments inserted into the nozzle passed into the nozzle with ease. A Nema 17 stepper motor with gripping gears were used to feed the filament into the extruder accurately.

6.1.2 6-Axis Robot Arm and Printing Test Cell

The robot arm chosen for this project was an IRB1200-7/0.7 (ABB Ltd.) as seen in Figure 6-3. This robot was chosen for specifically for its excellent accuracy of 0.2 mm and rigidity, with its high speeds and weight bearing of up to 7 kg, offering good expandability for future projects. The accuracy and rigidity are particularly important, as vibrations that occur during the printing process will decrease print quality, this the print head vibrating could also cause breakage in the printed samples [153]. As continuous PCF printing needs to be done quickly to be applicable in industry, the high speeds of this robot arm will not limit research functionality. The large working space provided by the robot arm will also aid in not hindering research efforts in the future if large volume printing is desired.

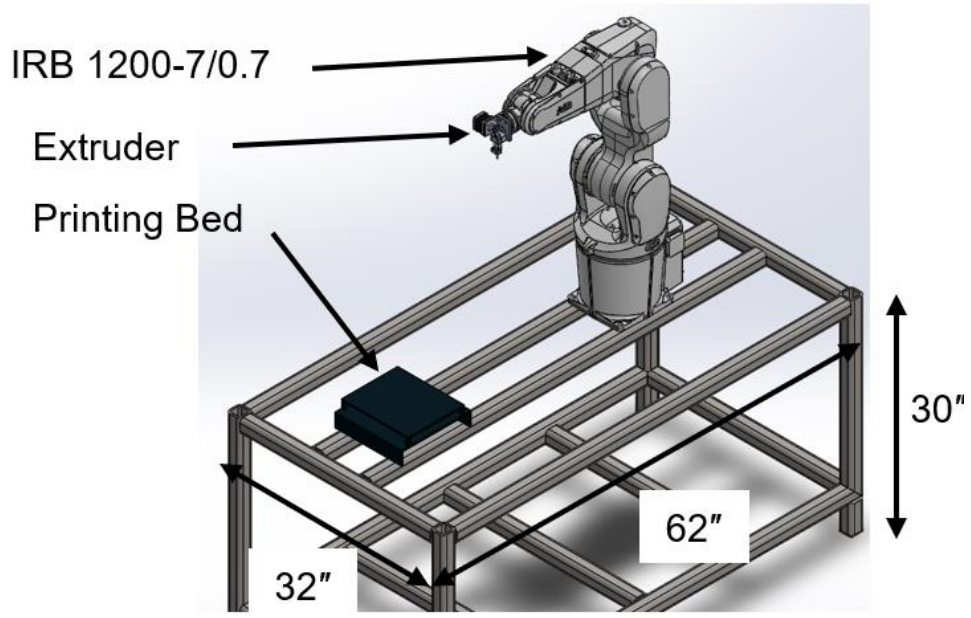

Figure 6-3: Robot printing setup, robot and extruder controllers are placed in the below portion of the table.

The 6-axis robot arm was placed on a custom constructed table, the image can be seen in Figure 6-3 made form welded square tubes. The design was chosen to limit the footprint of the system and to have ease of portability. A printing bed was fabricated into the table, the print bed levelling was done by using four compression springs adjusted with screws. Simple print patterns were performed by the robot and the print bed was calibrated such that the first layer adhesion was sufficient. The printing bed was coated in a thin layer of polyethyleneimine (PEI), to promote adhesion of the first layer on the bed, this polymer was chosen as it is known for its adhesive properties to other polymers.

6.1.3 Software and Control

The stepper motor, heater, and thermistor on the extruder were managed using a RAMPS 1.4, which is a modified Arduino board specifically fabricated for 3D printing applications. To 3D print with the robot arm used for this project, a method to convert the 3D printing instructions found in common Gcode into a format that the robot could understand is required. Robots manufactured by ABB Ltd. use a proprietary language called RAPID. Coding in this language is not user friendly, hence the offline robot simulation software of RobotStudio was used. RobotStudio allows for teaching of motions and instructions to a simulated robot offline. These instructions can then be turned into RAPID code and then transferred to the real-world platform. RobotStudio contains a 3D printing plugin, which allows for Gcode to be uploaded onto the software, this Gcode is then converted to the RAPID code, with many settings available. Options like robot speed, tool orientation, the use of additional axes, and print quality can all be adjusted prior to the conversion. Software integration between the Robotstudio and the extruder Ramps 1.4 controller was attempted, however this was a long process that did not result in a complete product due to the differences between the control protocols. Future work will need to devise a control system in which a feedback loop between the extruder and robot can be created and used such that accurate printing can be done for more complex geometries.

The printing process involved first creating Gcode to be printed. Commercial slicer software can not be used for this process as they disregard fiber orientation and do not take into consideration the custom filament and nozzle sizes. FullControl Gcode Designer was used as it allows for print parameters to be quickly turned into a Gcode without the need of any CAD models or slicer software [152].

6.2 Comparison of Extruders

Using methods developed in prior Chapters, samples were created and had their thermal conductivities measured. First, samples were created with the same parameters as the old extruder to understand if the new design decisions for the new extruder had much effect on breakage. The new extruder, with its PTFE coating, larger nozzle, and longer heating zone is expected to provide higher thermal conductivities at the same print angle. Samples were printed using the same printing parameters with the only difference being the extruder itself as seen in Figure 6-1. The first of the tests involved measuring the thermal conductivity of a raster, printed at a 45° nozzle orientation on both the old and new printing system. This was done to examine the effects the new nozzles design decisions had on fiber breakage and thermal conductivity. Samples were printed at the same printing parameters of 800 mm/min printing speed, 215°C for nozzles, and 60°C for the print bed. Figure 6-4 shows the comparison between the two samples.

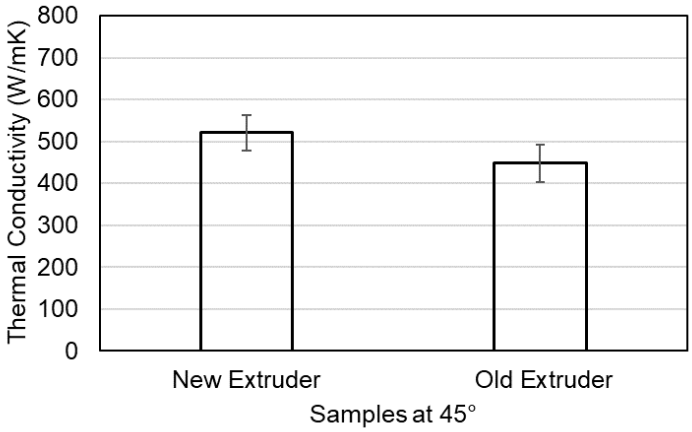

Figure 6-4: Measured thermal conductivity of K13D2U samples printed at 45° nozzle orientation using the old and new printer.

The previously used extruder was limited to printing at 45° due to the fabricated design, limiting the thermal conductivity of printed samples to 442 W/mK. When printing with the new nozzle, a thermal conductivity of 521 W/mK was measured. For the newly manufactured samples, a thermal gradient was measured with a change in temperature of 4.8 K across a length of 20.5 mm. The high uncertainty of these samples is a result of the uncertainty of the diameter of the fibers as discussed previously; Naito et al. saw that the 11 μm diameter PCF varied in their diameter by 0.5 μm [138]. This increase in thermal conductivity shows that having a nozzle in which the fibers are heated for longer and can pass through easier results in less broken fibers overall.

6.3 Nozzle Orientation

Samples were then examined for their thermal conductivity with varying print angles, which is the angle between a line normal to the print bed and a line through the center of the nozzle as seen in Figure 6-5. A single raster was extruded onto the printing bed, each tow of the K13D2U sample has around 2000 individual fibers, with each fiber approximately 11 μm in diameter. The same printing speed of 800 mm/min, hot end temperature of 220 °C, and bed temperature of 60 °C was used when printing all samples. All samples were printed using the same parameters and g-code settings, except for the angle of the nozzle to the bed, with the tested angles between the nozzle and normal being 45°, 50°, 55° and 60°. Samples were printed to a length of 100 mm, however had 20 mm removed from each end to eliminate errors because of nozzle acceleration or the cut-off method used.

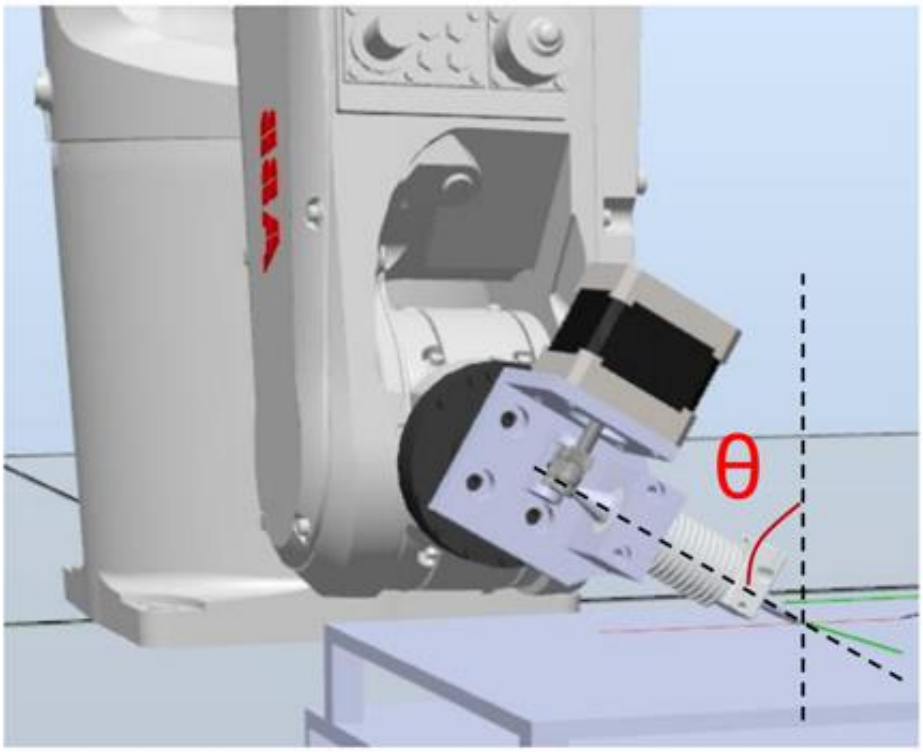

Figure 6-5: Angle identification for new robot extruder.

Throughout this project, it was hypothesized that the nozzle orientation with respect to the printing bed was the main contributor to breakage seen in all the samples that have been tested so far. Samples were printed at 5° intervals from 45° to 60°, the angle could not be increased anymore as parts of the extruder came into contact with the printing bed. Furthermore, when printing at such angles, the printed PCF did not adhere to the bed, resulting in failed prints and inconsistent print quality. During experiment, the cold block was held at 14 °C and the hot clamp was supplied with approximately 40 mW. The ambient temperature in the chamber was kept at 22°C. The distance between thermistors T1 and T2 on the samples was approximately 20 mm apart for each sample such that a large enough temperature difference could be measured.

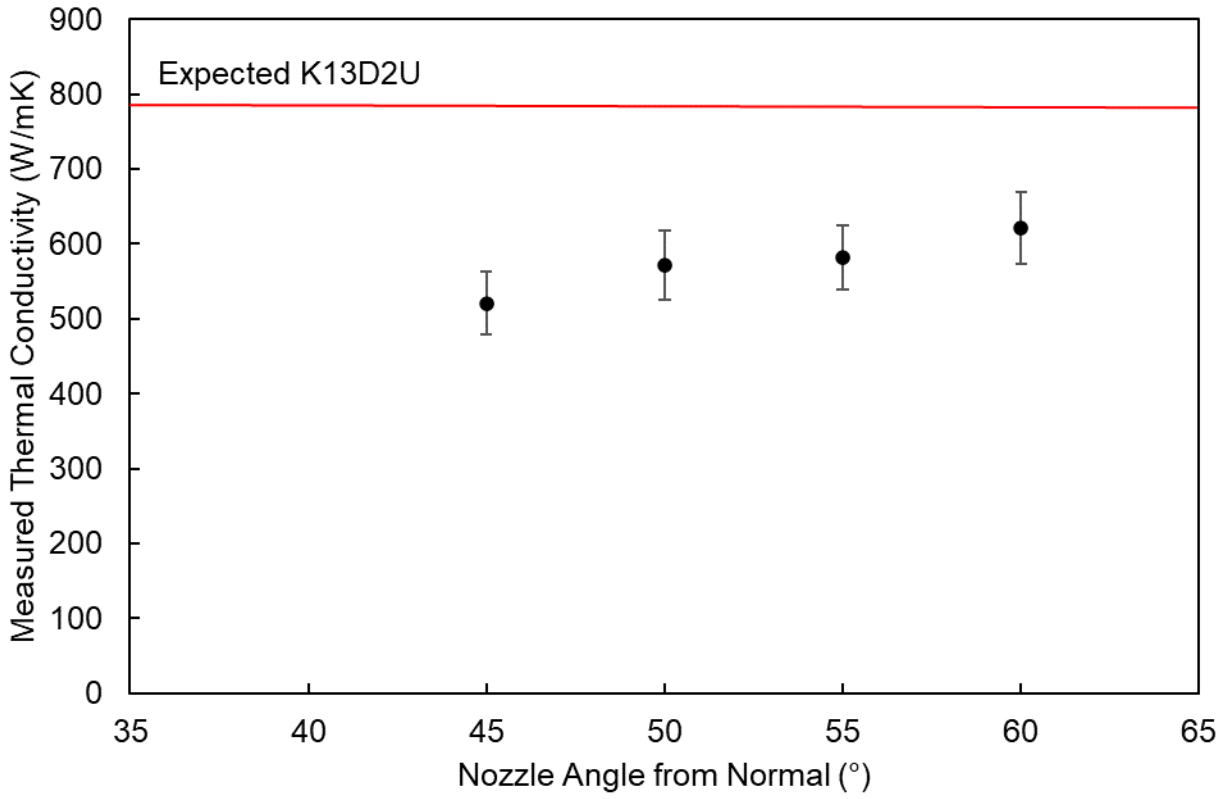

Figure 6-6: Measured thermal conductivity of pitch carbon fiber samples 3D printed at varying nozzle orientation angles.

The extruder from previous investigations was limited to printing at only at 45° angle. This printing limitation yielded a measured thermal conductivity of 442 W/mK (when printing at a linear speed of 800 mm/min) representing only 58% of the specified thermal conductivity of the original pitch carbon fiber. The new extruder printed three different samples at 45°, 50°, 55°, and 60°, which yielded thermal conductivity values of 521, 578, 581, and 621 W/mK, respectively, shown in Figure 6-6. This demonstrates that shallower print angles between the heated bed and nozzle results in less breakage in the fibers, and thus resulting in higher thermal conductivities (closer to original fiber values). The sample printed at 60° showed the best result at 82% of the original thermal conductivity of the PCF (K13D2U).

6.4 Radius of Curvature

Tests were also done to discover what the smallest radius of curvature on the XY-plane could be printed before causing additional breakage. This testing was done as the future of this project would involve printing fibers along the heat flow paths, which requires a curving motion from the extruder to be able to print. Previously, the extruder used could not accomplish this radial motion as the PCF extruding nozzle had a constant orientation. Using the 3D printing plugin in RobotStudio, the nozzle could be made to have a consistent orientation with the direction of printing, resulting in the nozzle always being angled at a given angle in the direction of printing. Radius of curvature of these samples were varied from 50 mm down to 10 mm as seen in Figure 6-7. All prints were done at same printing speed of 800 mm/min, hot end temperature of 220°C, and bed temperature of 60°C. Prior to and after the curvature portion of the prints, the samples had 10 mm of straight printing to allow for the samples to be fully adhered to the bed.

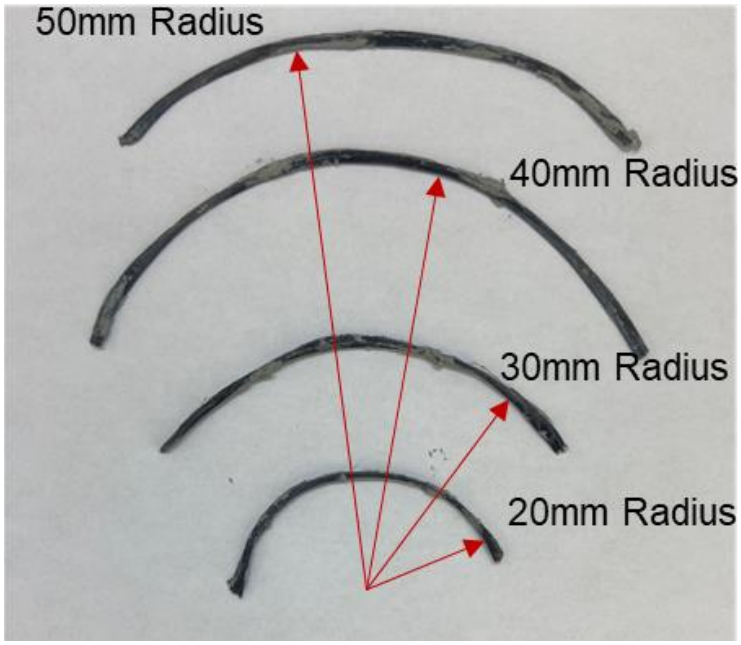

Figure 6-7: Images of printed samples at varying radius of curvatures.

When printing samples with radius of curvature, an issue was encountered with the Robotstudio software, similar to 3D printers, the RAPID code generated by the software instructs

the robot to travel between discrete points rather than continuous motion, specifically when below 1 mm. The minimum distance between points was set to 1 mm and the Gcode was made such that each curve was made of segments greater than 1 mm. The samples tested were printed at a nozzle orientation of 55°, although 60° is the max angle that can be printed at yielding the highest of thermal conductivities, print bed adhesion was more desired in these samples. Samples were printed and tested with all other parameters kept the same; the results were compared to the thermal conductivity of linear samples printed at 55° as if the thermal conductivity is lower than this value then it can be interpreted that more breakage is happening to the samples.

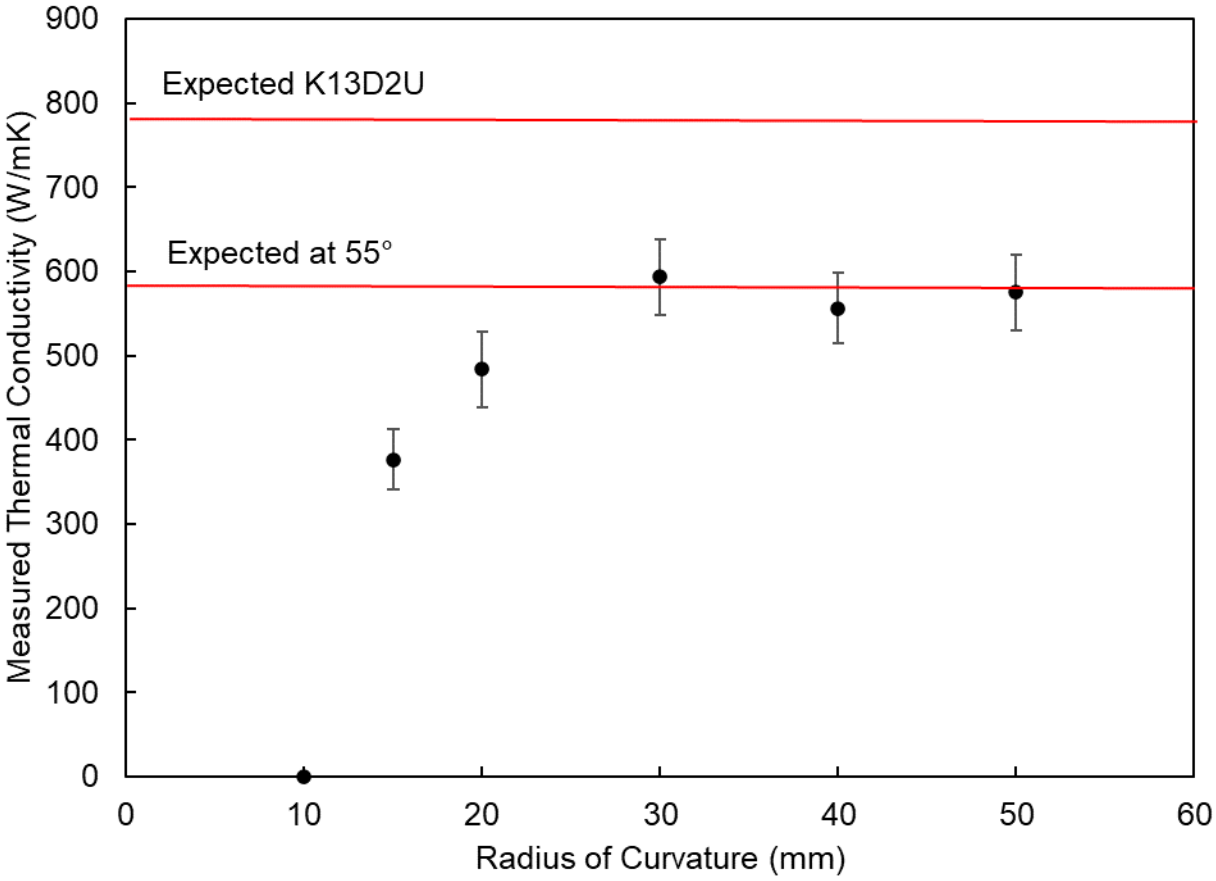

Figure 6-8:Thermal Conductivity of samples printed at varying radius of curvatures.

Figure 6-8 shows the measured thermal conductivity of samples with respect to the radius of curvature they were printed at. Samples could not be printed at a radius of curvature of less

than 15 mm; an attempt to print at a radius of 10 mm was made, however, this curve was too tight, and the sides of the nozzle were observed to be clearly cutting into the CF tow during the extrusion. Samples printed with a radius between 30 and 50 mm had their thermal conductivities ranging from 556 W/mK to 593 W/mK, being within the error of the expected thermal conductivity of 581 W/mK. The sample printed at a radius of 20 mm was the first to show degradation in thermal conductivity, having a thermal conductivity of 483 W/mK. A radius of 15 mm was also attempted, and lower thermal conductivities were seen: the thermal conductivity of the sample being 376 W/mK.

6.5 Angular Printing

Corners and turns are also an important aspect of 3D printing, hence samples were printed and visually examined to qualitatively identify how thermal conductivity decreased from the differently angled corners. Thermal conductivity tests were done on samples printed in which the nozzle simply turned, and samples where a small curvature of radius of 20 mm was used, as seen in Figure 6-9. A curvature radius of 20 mm was used as it gave the highest resolution for the corner without increasing the breakage, as known from the previous radius of curvature testing. Similar to radius of curvature when it comes to 3D printing, the printing of corners is an important aspect of creating complex geometries. It is expected that corners will result in breakage as the angles created in the XY-plane are the same as those created between the nozzle and normal of the bed. To counter act this breakage, a radius of curvature is experimented with; 20 mm was chosen as Figure 6-8 shows that this radius introduces more breakage. After testing, the fibers only degraded by approximately 17% from what is expected when printing at 55°, with the angle still looking sharp.

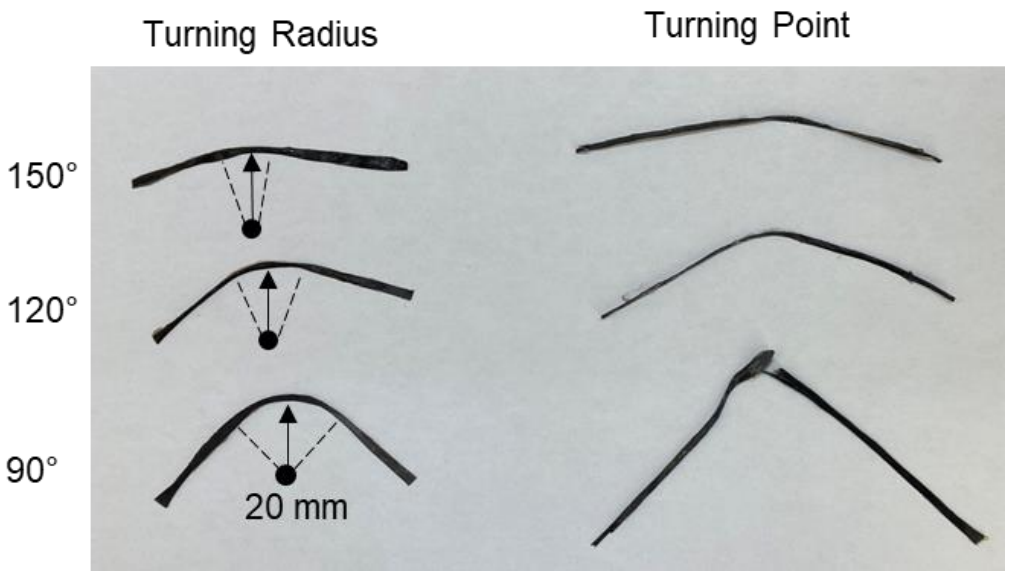

Figure 6-9: Images of 3D printed samples at varying corner angles, with and without a turning radius.

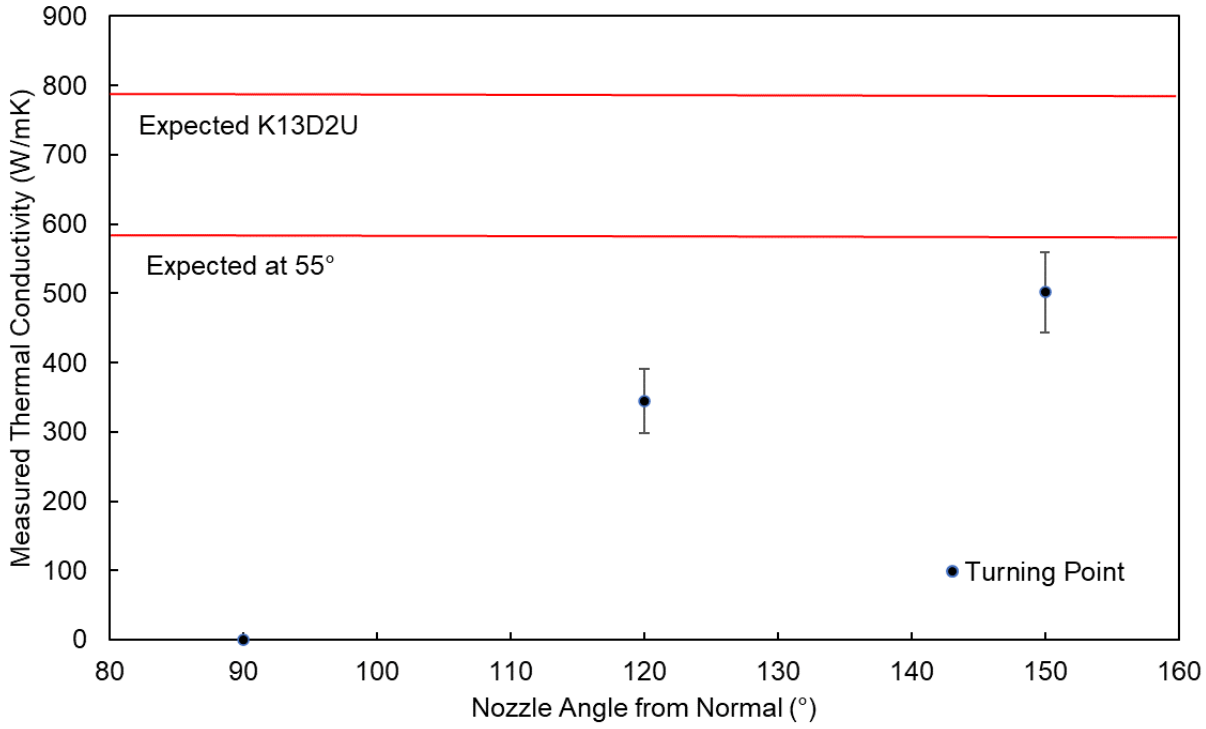

Figure 6-10: Sample measured thermal conductivity when printed at varying corner angles with no radius of curvature.

When printing to create a sharp corner, any angle for the corner was found to cause additional breakage as seen in Figure 6-10. Although the expected thermal conductivity was set

to what was found in Figure 6-6 when printing at a 55° (581 W/mK), samples showed a steady decline in thermal conductivity. When the corner angle was set to 150° and 120°, additional breakage was observed with the thermal conductivity being measured at 501 W/mK and 334 W/mK respectively. Corners with an angle of 90° or less were found to result in completed detachment of fibers, as seen in Figure 6-9. The breakage observed when printing corners is attributed to the edge of the nozzle at the internal corner, damaging the fibers when the rotation is being performed.

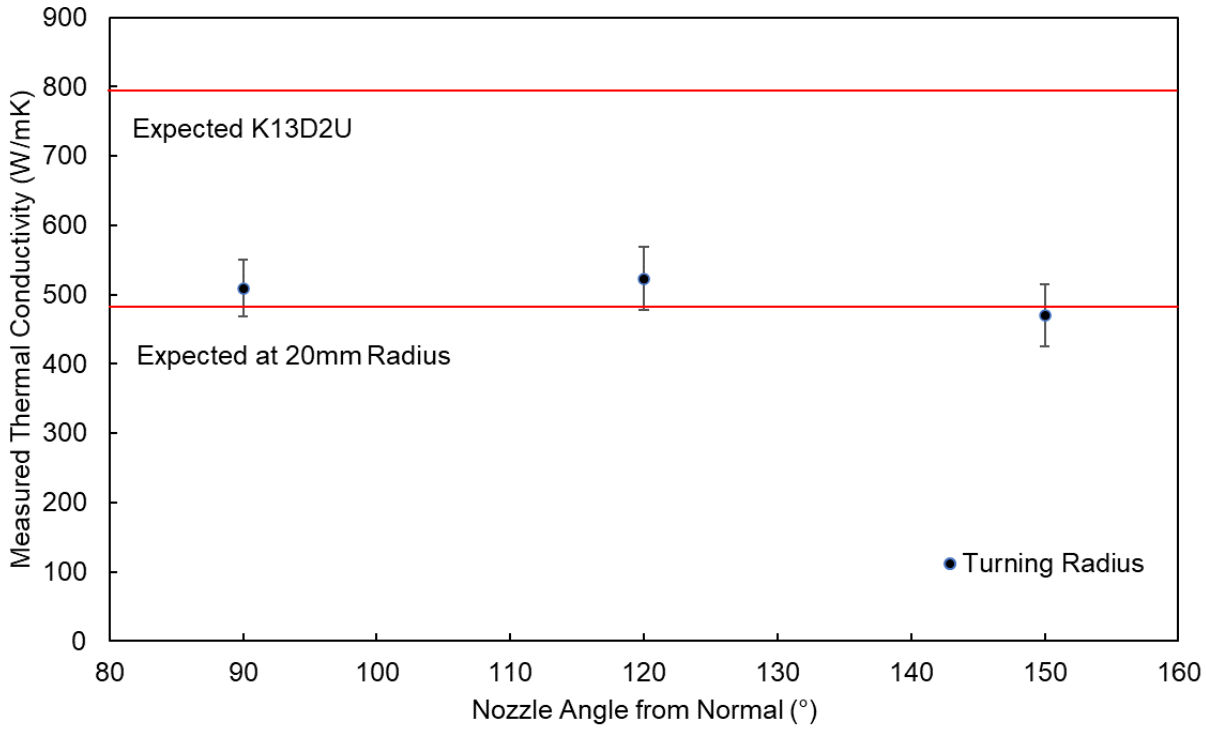

Figure 6-11: Sample measured thermal conductivity when printed at varying corner angles with a radius of curvature of 20 mm.

Figure 6-11 explores that when printing corner angles, using a turning radius prevents additional breakage from occurring. The expected thermal conductivity line is based on the thermal conductivity of samples in Figure 6-8, specifically of the samples printed at a 20 mm radius of curvature. All the samples printed are within the uncertainty error of 483 W/mK, from 150° to 90° corner angle.

6.6 Conclusion

The hypothesis of nozzle angle contributing the most to lowering thermal conductivity was verified. Samples of PCF tows were 3D printed using a custom extruder and IRB 1200-7/0.7 and had their thermal conductivities measured with respect to the nozzle angle they were printed at. Compared to 3D printing with the initial extruder in Chapter 3, printing at a 60° nozzle angle with the new extruder led to increase of thermal conductivity from 440 W/mK to 621 W/mK (81% of the original thermal conductivity of the K13D2U). Other printing method were also investigated such as printing curvatures with varying radii and sharp corners, as these are important aspects of 3D printing complex geometries. It was found that the smallest radius of curvature that can be printed without inducing any additional decrease in thermal conductivity was 30 mm, 20 mm and 15 mm radii saw a sharp decrease in thermal conductivity. When extruding sharp corners, any angle chosen for the corner was found to decrease thermal conductivity, with acute angles causing complete discontinuity in the PCF. Using a curvature for the corners was found to amend this issue, resulting in no visible decrease in thermal conductivity.

Chapter 7 Summary, Conclusions, & Future Work

The work done through this project has revealed several important aspects behind the 3D printing of continuous PCF reinforced polymer composites. First, it was shown that continuous PCF can be 3D printed, the resulting composites had thermal conductivities much greater than others in literature. The resultant samples however had excessive amounts of discrepancy in effective thermal conductivity between what was expected and what was achieved, which was believed to be a factor of the breakage of fibers during the printing process. To identify how different 3D printing parameters affect the fiber breakage, a heat flow meter in a vacuum chamber was designed and fabricated to measure thermal conductivity of fibers after processes were done on them. Initially, one process that was suspected of causing breakage was the fiber coating process, however this was disproven, and the process was shown to cause no breakage. The next element analyzed was printing speed, as this is a common parameter to examine in 3D printing, again this process was shown to have little effect on fiber breakage except in outlier cases where the firmware of the 3D printer caused excess breakage. The last parameter examined on the old extruder and printing system was the raster spacing, this parameter was investigated as overcrowding was observed when printing. Through creation of large samples and testing with a guarded heat flow meter used in previous projects, overall total breakage was reduced. Sample thermal conductivity was found to be what was expected when using fiber thermal conductivity discovered from previous testing when using a raster spacing of 1.5 mm, whilst samples with 1 mm raster spacing had more breakage than that caused by the extruder design.

The experimental setup and testing performed, yielded knowledge that breakage was occurring due to nozzle design rather than printing parameters, necessitating the need for a new nozzle design. Furthermore, a new printing system had to be created to allow for multi-directional printing, which was missing from the initial printer, due to printer extruder angling. A new design

for an extruder and printing system was made, using a 6-axis robot arm and a custom extruder, which allowed for better control of the nozzle during printing. The printing system was compared to the original prototype and found to decrease the amount of breakage seen through thermal conductivity measurements. Nozzle orientation was examined, and samples were printed to test the effects of nozzle orientations on breakage. The angle between the nozzle and a normal from the printing bed was varied, to understand how much this angle affected CF quality. Common printing practices such as printing curves and corners was also tested to find the limitations of the new printing system.

In conclusion, it was found that nozzle angling had the largest impact on breakage. The sharp corner caused when the PCF leaves the extruder onto the printing bed induces significant fibre breakage. Through angling the nozzle such that a 60° angle was formed between the nozzle and the normal of the bed, a thermal conductivity of 621 W/mK was achieved out of the expected 765 W/mK. The printing of curves did not result in additional breakage until the radius of curvature was set to 20 mm. The printing of sharp corners caused high amounts of breakage; this breakage could be avoided using a small radius of curvature.

A lot has been learnt about effective printing techniques for pitch carbon fibre that can help progress current endeavours in 3D printing of CF heatsinks. The basic building parameters such as coating, raster spacing, and nozzle angle provided insight into better pitch carbon fibre printing practices. This work can help continue towards building effective PCF heat exchangers.

7.1 Future Work

The main mechanisms for breakage are now well understood for continuous PCF 3D printing, with this knowledge, future work will need to be done to show its capabilities and applications while making it a viable form of manufacturing. Updating the process to be able to print faster will allow for higher volume production for heat exchangers 3D printed. With stronger heaters production can be sped up, a stronger heating system will allow for the temperature

decrease witnessed in Chapter 5 to not be as prevalent. Printing speed can be increased further, as testing has shown that printing speeds does not increase fiber breakage if printer firmware parameters are given respect.

Additional work with extruded design is also desired, Chapter 6 showed that the breakage varies linearly with the nozzle's orientation with the bed. Printing at a 90° angle with the current type of extruder is not practical, hence it is believed an extruder using a roller, like the tape winding process, is believed to be the next evolution for the printer. Designing a roller with a radius large enough to not cause additional breakage, would allow for printing to be done with the extruder being normal to the printing bed. The use of a roller would also help in print adhesion and linear alignment of rasters, as the melted polymer matrix of the PCF filament would be pressed against each other.

Research should also be done on the performance of 3D printed PCF for applications for large scale samples. Through the 3D printing of samples such as heat sinks and heating blocks, the viability of continuous PCF printing can be proven. The polymer matrix of the samples means that high temperatures can not be used. To amend this, future work should also be done on using a polymer matrix of PEEK or PEI, otherwise refrigerant use cases should be investigated.

Chapter 8 References

[1] J. B. Marcinichen, J. A. Olivier, N. Lamaison, and J. R. Thome, “Advances in electronics cooling,” *Heat Transf. Eng.*, vol. 34, no. 5–6, pp. 434–446, 2013, doi: 10.1080/01457632.2012.721316.

[2] M. Bahiraei and S. Heshmatian, “Electronics cooling with nanofluids: A critical review,” *Energy Convers. Manag.*, vol. 172, no. July, pp. 438–456, 2018, doi: 10.1016/j.enconman.2018.07.047.

[3] S. M. Sohel Murshed and C. A. Nieto de Castro, “A critical review of traditional and emerging techniques and fluids for electronics cooling,” *Renew. Sustain. Energy Rev.*, vol. 78, no. April, pp. 821–833, 2017, doi: 10.1016/j.rser.2017.04.112.

[4] HUGO MARTÍN, “United Airlines saves 170,000 gallons of fuel by using lighter paper on inflight magazine,” *Los Angeles Times*, 2018. [Online]. Available: https://www.latimes.com/business/la-fi-travel-briefcase-united-inflight-magazine-20180120-story.html#:~:text=For a typical 737 plane,%24290%2C000 in annual fuel costs.

[5] J. Puig-Suari, C. Turner, and W. Ahlgren, “Development of the standard CubeSat deployer and a CubeSat class picosatellite,” *IEEE Aerosp. Conf. Proc.*, vol. 1, pp. 1347–1353, 2001, doi: 10.1109/aero.2001.931726.

[6] J. Choi, C. Dun, C. Forsythe, M. P. Gordon, and J. J. Urban, “Lightweight wearable thermoelectric cooler with rationally designed flexible heatsink consisting of phase-change material/graphite/silicone elastomer,” *J. Mater. Chem. A*, vol. 9, no. 28, pp. 15696–15703, 2021, doi: 10.1039/d1ta01911b.

[7] Y. Shi, Y. Wang, D. Mei, and Z. Chen, “Wearable thermoelectric generator with copper foam as the heat sink for body heat harvesting,” *IEEE Access*, vol. 6, pp. 43602–43611, 2018, doi: 10.1109/ACCESS.2018.2863018.

[8] M. Endo, K. Takeuchi, S. Igarashi, K. Kobori, M. Shiraishi, and H. W. Kroto, “The production

and structure of pyrolytic carbon nanotubes (PCNTs)," *J. Phys. Chem. Solids*, vol. 54, no. 12, pp. 1841–1848, 1993, doi: 10.1016/0022-3697(93)90297-5.

[9] H. Chen and A. J. H. McGaughey, "Thermal conductivity of carbon nanotubes with defects," *ASME/JSME 2011 8th Therm. Eng. Jt. Conf. AJTEC 2011*, 2011, doi: 10.1115/ajtec2011-44173.

[10] B. Salce, L. Devoille, R. Calemczuk, A. I. Buzdin, G. Dhalenne, and A. Revcolevschi, "Thermal conductivity of pure and Si-doped CuGeO3," *Phys. Lett. Sect. A Gen. At. Solid State Phys.*, vol. 245, no. 1–2, pp. 127–132, 1998, doi: 10.1016/S0375-9601(98)00347-8.

[11] I. Mochida, S. H. Yoon, N. Takano, F. Fortin, Y. Korai, and K. Yokogawa, "Microstructure of mesophase pitch-based carbon fiber and its control," *Carbon N. Y.*, vol. 34, no. 8, pp. 941–956, 1996, doi: 10.1016/0008-6223(95)00172-7.

[12] Y. Ibrahim and R. Kempers, "Effective thermal conductivity of 3D-printed continuous wire polymer composites," *Prog. Addit. Manuf.*, Jan. 2022, doi: 10.1007/s40964-021-00256-5.

[13] S. Olcun and R. Kempers, "Thermal Characterization of Continuous Pitch Carbon Fiber 3D-Printed using a 6-Axis Robot Arm," 2022.

[14] C. T'Joen, Y. Park, Q. Wang, A. Sommers, X. Han, and A. Jacobi, "A review on polymer heat exchangers for HVAC&R applications," *Int. J. Refrig.*, vol. 32, no. 5, pp. 763–779, 2009, doi: 10.1016/j.ijrefrig.2008.11.008.

[15] X. Chen, Y. Su, D. Reay, and S. Riffat, "Recent research developments in polymer heat exchangers - A review," *Renew. Sustain. Energy Rev.*, vol. 60, pp. 1367–1386, 2016, doi: 10.1016/j.rser.2016.03.024.

[16] D. C. Deisenroth, M. A. Arie, S. Dessiatoun, A. Shooshtari, M. Ohadi, and A. Bar-Cohen, "Review of most recent progress on development of polymer heat exchangers for thermal management applications," *ASME 2015 Int. Tech. Conf. Exhib. Packag. Integr. Electron. Photonic Microsystems, InterPACK 2015, collocated with ASME 2015 13th Int. Conf.*

Nanochannels, Microchannels, Minichannels, vol. 3, pp. 1–10, 2015, doi: 10.1115/IPACK2015-48637.

[17] L. Zaheed and R. J. J. Jachuck, “Review of polymer compact heat exchangers, with special emphasis on a polymer film unit,” *Appl. Therm. Eng.*, vol. 24, no. 16, pp. 2323–2358, 2004, doi: 10.1016/j.applthermaleng.2004.03.018.

[18] J. G. Cevallos, A. E. Bergles, A. Bar-Cohen, P. Rodgers, and S. K. Gupta, “Polymer heat exchangers-history, opportunities, and challenges,” *Heat Transf. Eng.*, vol. 33, no. 13, pp. 1075–1093, 2012, doi: 10.1080/01457632.2012.663654.

[19] H. Müller-Steinhagen, M. R. Malayeri, and A. P. Watkinson, “Heat exchanger fouling: Mitigation and cleaning strategies,” *Heat Transf. Eng.*, vol. 32, no. 3–4, pp. 189–196, 2011, doi: 10.1080/01457632.2010.503108.

[20] T. Kroulíková, T. Kůdelová, E. Bartuli, J. Vančura, and I. Astrouski, “Comparison of a novel polymeric hollow fiber heat exchanger and a commercially available metal automotive radiator,” *Polymers (Basel).*, vol. 13, no. 7, pp. 1–13, 2021, doi: 10.3390/polym13071175.

[21] T. Brozova, M. Raudensky, and I. Astrouski, “Flexible polymeric hollow fiber heat exchangers,” *Proc. Therm. Fluids Eng. Summer Conf.*, vol. 2018-March, pp. 1373–1382, 2018, doi: 10.1615/TFEC2018.hte.020837.

[22] J. B. P. Christmann, L. J. Krätz, and H. J. Bart, “Falling film evaporation with polymeric heat transfer surfaces,” *Desalination*, vol. 308, pp. 56–62, 2013, doi: 10.1016/j.desal.2011.05.027.

[23] I. A. Tsekmes, R. Kochetov, P. H. F. Morshuis, and J. J. Smit, “Thermal conductivity of polymeric composites: A review,” *Proc. IEEE Int. Conf. Solid Dielectr. ICSD*, pp. 678–681, 2013, doi: 10.1109/ICSD.2013.6619698.

[24] B. Weidenfeller, M. Höfer, and F. R. Schilling, “Thermal conductivity, thermal diffusivity, and specific heat capacity of particle filled polypropylene,” *Compos. Part A Appl. Sci.*

Manuf., vol. 35, no. 4, pp. 423–429, 2004, doi: 10.1016/j.compositesa.2003.11.005.

[25] C. I. Idumah and A. Hassan, “Recently emerging trends in thermal conductivity of polymer nanocomposites,” *Rev. Chem. Eng.*, 2016, doi: 10.1515/revce-2016-0004.

[26] I. L. Ngo, S. Jeon, and C. Byon, “Thermal conductivity of transparent and flexible polymers containing fillers: A literature review,” *International Journal of Heat and Mass Transfer*. 2016. doi: 10.1016/j.ijheatmasstransfer.2016.02.082.

[27] Y. Acari, A. Ueda, and S. Nacal ’, “Thermal Conductivity of a Polymer Composite,” *J. Appl. Polym. Sci.*, 1993.

[28] R. F. Hill and P. H. Supancic, “Thermal Conductivity of Platelet-Filled Polymer Composites”.

[29] A. Li, C. Zhang, and Y. F. Zhang, “Thermal conductivity of graphene-polymer composites: Mechanisms, properties, and applications,” *Polymers (Basel).*, vol. 9, no. 9, pp. 1–17, 2017, doi: 10.3390/polym9090437.

[30] Y.-M. Chen and J.-M. Ting, “Ultra high thermal conductivity polymer composites,” *Carbon N. Y.*, vol. 40, pp. 359–362, 2002.

[31] G. W. Lee, M. Park, J. Kim, J. I. Lee, and H. G. Yoon, “Enhanced thermal conductivity of polymer composites filled with hybrid filler,” *Compos. Part A Appl. Sci. Manuf.*, 2006, doi: 10.1016/j.compositesa.2005.07.006.

[32] H. Serkan Tekce, D. Kumlutas, and I. H. Tavman, “Effect of Particle Shape on Thermal Conductivity of Copper Reinforced Polymer Composites”, doi: 10.1177/0731684407072522.

[33] R. Trojanowski, T. Butcher, M. Worek, and G. Wei, “Polymer heat exchanger design for condensing boiler applications,” *Appl. Therm. Eng.*, vol. 103, pp. 150–158, 2016, doi: 10.1016/j.applthermaleng.2016.03.004.

[34] M. Srinivasan, P. Maettig, K. W. Glitza, B. Sanny, and A. Schumacher, “Out of Plane

Thermal Conductivity of Carbon Fiber Reinforced Composite Filled with Diamond Powder," *Open J. Compos. Mater.*, vol. 6, no. April, pp. 41–57, 2016.

[35] P. M. Adams, H. A. Katzman, G. S. Rellick, and G. W. Stupian, "Characterization of high thermal conductivity carbon fibers and a self-reinforced graphite panel," *Carbon N. Y.*, vol. 36, no. 3, pp. 233–245, 1998, doi: 10.1016/S0008-6223(97)00189-9.

[36] S. Yuan, J. Bai, C. K. Chua, J. Wei, and K. Zhou, "Highly enhanced thermal conductivity of thermoplastic nanocomposites with a low mass fraction of MWCNTs by a facilitated latex approach," *Compos. Part A Appl. Sci. Manuf.*, 2016, doi: 10.1016/j.compositesa.2016.09.002.

[37] J. G. Park *et al.*, "Thermal conductivity of MWCNT/epoxy composites: The effects of length, alignment and functionalization," *Carbon N. Y.*, vol. 50, no. 6, pp. 2083–2090, 2012, doi: 10.1016/j.carbon.2011.12.046.

[38] A. Miranda, N. Barekar, and B. J. McKay, "MWCNTs and their use in Al-MMCs for ultra-high thermal conductivity applications: A review," *J. Alloys Compd.*, vol. 774, pp. 820–840, 2019, doi: 10.1016/j.jallcom.2018.09.202.

[39] M. L. Minus and S. Kumar, "The processing, properties, and structure of carbon fibers," *Jom*, vol. 57, no. 2, pp. 52–58, 2005, doi: 10.1007/s11837-005-0217-8.

[40] K. I. Morita, "Carbon Fibers," *Sen'i Gakkaishi*, vol. 40, pp. 1–6, 1984, doi: 10.2115/fiber.40.4-5_P344.

[41] E. Frank, D. Ingildeev, and M. R. Buchmeiser, *High-performance PAN-based carbon fibers and their performance requirements*, vol. 000. Elsevier Ltd, 2017. doi: 10.1016/B978-0-08-100550-7.00002-4.

[42] M. G. Huson, "High-performance pitch-based carbon fibers," in *Structure and Properties of High-Performance Fibers*, Elsevier, 2017, pp. 31–78. doi: 10.1016/B978-0-08-100550-7.00003-6.

[43] J. Flöck, K. Friedrich, and Q. Yuan, “On the friction and wear behaviour of PAN- and pitch-carbon fiber reinforced PEEK composites,” *Wear*, vol. 225–229, no. I, pp. 304–311, 1999, doi: 10.1016/S0043-1648(99)00022-8.

[44] Q. Yuan, S. A. Bateman, and K. Friedrich, “Thermal and mechanical properties of PAN- and pitch-based carbon fiber reinforced PEEK composites,” *J. Thermoplast. Compos. Mater.*, vol. 21, no. 4, pp. 323–336, 2008, doi: 10.1177/0892705708089478.

[45] K. Miyachi, Y. Muranaka, S. Nonaka, A. Ueno, and H. Nagano, “Measurement of thermal diffusivity and evaluation of fiber condition of discontinuous fiber CFRP,” *Infrared Phys. Technol.*, vol. 115, no. December 2020, p. 103743, 2021, doi: 10.1016/j.infrared.2021.103743.

[46] R. J. Kuriger, M. K. Alam, D. P. Anderson, and R. L. Jacobsen, “Processing and characterization of aligned vapor grown carbon fiber reinforced polypropylene,” *Compos. - Part A Appl. Sci. Manuf.*, vol. 33, no. 1, pp. 53–62, 2002, doi: 10.1016/S1359-835X(01)00070-7.

[47] R. J. Kuriger and M. K. Alam, “Thermal conductivity of thermoplastic composites with submicrometer carbon fibers,” *Exp. Heat Transf.*, vol. 15, no. 1, pp. 19–30, 2002, doi: 10.1080/089161502753341843.

[48] P. Feraboli, E. Peitso, T. Cleveland, P. B. Stickler, and J. C. Halpin, “Notched behavior of prepreg-based discontinuous carbon fiber/epoxy systems,” *Compos. Part A Appl. Sci. Manuf.*, vol. 40, no. 3, pp. 289–299, 2009, doi: 10.1016/j.compositesa.2008.12.012.

[49] M. Kim *et al.*, “Characterization of resistive heating and thermoelectric behavior of discontinuous carbon fiber-epoxy composites,” *Compos. Part B Eng.*, vol. 90, pp. 37–44, 2016, doi: 10.1016/j.compositesb.2015.11.037.

[50] M. Hashimoto, T. Okabe, T. Sasayama, H. Matsutani, and M. Nishikawa, “Prediction of tensile strength of discontinuous carbon fiber/polypropylene composite with fiber

orientation distribution," *Compos. Part A Appl. Sci. Manuf.*, vol. 43, no. 10, pp. 1791–1799, 2012, doi: 10.1016/j.compositesa.2012.05.006.

[51] Y. Liu, B. Zwingmann, and M. Schlaich, "Carbon fiber reinforced polymer for cable structures-a review," *Polymers (Basel).*, vol. 7, no. 10, pp. 2078–2099, 2015, doi: 10.3390/polym7101501.

[52] S. Tang and C. Hu, "Design, Preparation and Properties of Carbon Fiber Reinforced Ultra-High Temperature Ceramic Composites for Aerospace Applications: A Review," *J. Mater. Sci. Technol.*, vol. 33, no. 2, pp. 117–130, 2017, doi: 10.1016/j.jmst.2016.08.004.

[53] M. Arif, M. Asif, and D. Ahmed, "Advanced Composite Material for Aerospace Application-a Review," *Int. J. Eng. Manuf. Sci.*, vol. 7, no. 2, pp. 393–409, 2017, [Online]. Available: http://www.ripublication.com

[54] E. C. Botelho, R. A. Silva, L. C. Pardini, and M. C. Rezende, "A review on the development and properties of continuous fiber/epoxy/aluminum hybrid composites for aircraft structures," *Mater. Res.*, vol. 9, no. 3, pp. 247–256, 2006, doi: 10.1590/S1516-14392006000300002.

[55] S. Y. Park, C. H. Choi, W. J. Choi, and S. S. Hwang, "A Comparison of the Properties of Carbon Fiber Epoxy Composites Produced by Non-autoclave with Vacuum Bag Only Prepreg and Autoclave Process," *Appl. Compos. Mater.*, vol. 26, no. 1, pp. 187–204, 2019, doi: 10.1007/s10443-018-9688-y.

[56] H. Koushyar, S. Alavi-Soltani, B. Minaie, and M. Violette, "Effects of variation in autoclave pressure, temperature, and vacuum-application time on porosity and mechanical properties of a carbon fiber/epoxy composite," *J. Compos. Mater.*, vol. 46, no. 16, pp. 1985–2004, 2012, doi: 10.1177/0021998311429618.

[57] R. Joven and B. Minaie, "Thermal properties of autoclave and out-of-autoclave carbon fiber-epoxy composites with different fiber weave configurations," *J. Compos. Mater.*, vol.

52, no. 29, pp. 4075–4085, 2018, doi: 10.1177/0021998318774608.

[58] M. Martins *et al.*, “Highly conductive carbon fiber-reinforced polymer composite electronic box: Out-of-autoclave manufacturing for space applications,” *Fibers*, vol. 6, no. 4, Dec. 2018, doi: 10.3390/fib6040092.

[59] C. Silva, E. Marotta, M. Schuller, L. Peel, and M. O’Neill, “In-plane thermal conductivity in thin carbon fiber composites,” *J. Thermophys. Heat Transf.*, vol. 21, no. 3, pp. 460–467, 2007, doi: 10.2514/1.27859.

[60] J. R. Gaier, Y. YoderVandenberg, S. Berkebile, H. Stueben, and F. Balagadde, “The electrical and thermal conductivity of woven pristine and intercalated graphite fiber-polymer composites,” *Carbon N. Y.*, vol. 41, no. 12, pp. 2187–2193, 2003, doi: 10.1016/S0008-6223(03)00238-0.

[61] N. Athanasopoulos and N. J. Siakavellas, “Heat Manipulation Using Highly Anisotropic Pitch-Based Carbon Fiber Composites,” *Adv. Eng. Mater.*, vol. 17, no. 10, pp. 1494–1503, 2015, doi: 10.1002/adem.201500085.

[62] E. M. Silverman, “Product Development of Engineered Thermal Composites for Cooling Spacecraft Electronics,” no. January 2005, pp. 1–19, 2005.

[63] K. Goncharov, Y. Panin, M. Balykin, and A. Khmelnitsky, “High Thermal Conductive Carbon Fiber Radiators with Controlled Loop Heat Pipes,” no. July, 2016.

[64] K. Yassin and M. Hojjati, “Processing of thermoplastic matrix composites through automated fiber placement and tape laying methods: A review,” *J. Thermoplast. Compos. Mater.*, vol. 31, no. 12, pp. 1676–1725, 2018, doi: 10.1177/0892705717738305.

[65] Y. Di Boon, S. C. Joshi, and S. K. Bhudolia, “Review: Filament winding and automated fiber placement with in situ consolidation for fiber reinforced thermoplastic polymer composites,” *Polymers (Basel).*, vol. 13, no. 12, 2021, doi: 10.3390/polym13121951.

[66] V. Dhinakaran, K. V. Surendar, M. S. H. Riyaz, and M. Ravichandran, “Review on study of

thermosetting and thermoplastic materials in the automated fiber placement process," *Mater. Today Proc.*, vol. 27, pp. 812–815, 2020, doi: 10.1016/j.matpr.2019.12.355.

[67] S. Sun, Z. Han, H. Fu, H. Jin, J. S. Dhupia, and Y. Wang, "Defect characteristics and online detection techniques during manufacturing of FRPs using automated fiber placement: A review," *Polymers (Basel).*, vol. 12, no. 6, p. 1337, 2020, doi: 10.3390/POLYM12061337.

[68] B. Denkena, C. Schmidt, K. Völtzer, and T. Hocke, "Thermographic online monitoring system for Automated Fiber Placement processes," *Compos. Part B Eng.*, vol. 97, pp. 239–243, 2016, doi: 10.1016/j.compositesb.2016.04.076.

[69] P. Zhang, R. Sun, X. Zhao, and L. Hu, "Placement suitability criteria of composite tape for mould surface in automated tape placement," *Chinese J. Aeronaut.*, vol. 28, no. 5, pp. 1574–1581, 2015, doi: 10.1016/j.cja.2015.06.002.

[70] N. Shahrubudin, T. C. Lee, and R. Ramlan, "An overview on 3D printing technology: Technological, materials, and applications," *Procedia Manuf.*, vol. 35, pp. 1286–1296, 2019, doi: 10.1016/j.promfg.2019.06.089.

[71] J. Y. Lee, J. An, and C. K. Chua, "Fundamentals and applications of 3D printing for novel materials," *Appl. Mater. Today*, vol. 7, pp. 120–133, 2017, doi: 10.1016/j.apmt.2017.02.004.

[72] A. Dawood, B. M. Marti, V. Sauret-Jackson, and A. Darwood, "3D printing in dentistry," *Br. Dent. J.*, vol. 219, no. 11, pp. 521–529, 2015, doi: 10.1038/sj.bdj.2015.914.

[73] S. C. Joshi and A. A. Sheikh, "3D printing in aerospace and its long-term sustainability," *Virtual Phys. Prototyp.*, vol. 10, no. 4, pp. 175–185, 2015, doi: 10.1080/17452759.2015.1111519.

[74] S. Kuntanapreeda and D. Hess, "Opening access to space by maximizing utilization of 3D printing in launch vehicle design and production," *Appl. Sci. Eng. Prog.*, vol. 14, no. 2, pp. 1–3, 2020, doi: 10.14416/J.ASEP.2020.12.002.

[75] D. C. Deisenroth, R. Moradi, A. H. Shooshtari, F. Singer, A. Bar-Cohen, and M. Ohadi, “Review of Heat Exchangers Enabled by Polymer and Polymer Composite Additive Manufacturing,” *Heat Transf. Eng.*, vol. 39, no. 19, pp. 1652–1668, 2018, doi: 10.1080/01457632.2017.1384280.

[76] E. Klein, J. Ling, V. Aute, Y. Hwang, and R. Radermacher, “A Review of Recent Advances in Additively Manufactured Heat Exchangers,” *Int. Refrig. Air Cond. Conf.*, no. 2006, pp. 1–10, 2018, [Online]. Available: https://docs.lib.purdue.edu/iracc%0Ahttps://docs.lib.purdue.edu/iracc/1983

[77] I. Kaur and P. Singh, “State-of-the-art in heat exchanger additive manufacturing,” *International Journal of Heat and Mass Transfer*, vol. 178. Elsevier Ltd, Oct. 01, 2021. doi: 10.1016/j.ijheatmasstransfer.2021.121600.

[78] D. Bacellar *et al.*, “Design optimization and validation of high-performance heat exchangers using approximation assisted optimization and additive manufacturing Design optimization and validation of high-performance heat exchangers using approximation assisted optimization an,” *Sci. Technol. Built Environ.*, vol. 23, no. 6, pp. 896–911, 2017, doi: 10.1080/23744731.2017.1333877.

[79] K. Rajan, M. Samykano, K. Kadirgama, W. Sharuzi, and W. Harun, *Fused deposition modeling : process , materials , parameters , properties , and applications*, no. 0123456789. Springer London, 2022. doi: 10.1007/s00170-022-08860-7.

[80] L. Novakova-Marcincinova, J. Novak-Marcincin, J. Barna, and J. Torok, “Special materials used in FDM rapid prototyping technology application,” *INES 2012 - IEEE 16th Int. Conf. Intell. Eng. Syst. Proc.*, pp. 73–76, 2012, doi: 10.1109/INES.2012.6249805.

[81] T. Isobe, T. Tanaka, T. Nomura, and R. Yuasa, “Comparison of strength of 3D printing objects using short fiber and continuous long fiber,” *IOP Conf. Ser. Mater. Sci. Eng.*, vol. 406, no. 1, 2018, doi: 10.1088/1757-899X/406/1/012042.

[82] F. Korkees, J. Allenby, and P. Dorrington, “3D printing of composites: design parameters and flexural performance,” *Rapid Prototyp. J.*, vol. 26, no. 4, pp. 699–706, 2020, doi: 10.1108/RPJ-07-2019-0188.

[83] V. Guerra, C. Wan, and T. McNally, “Fused deposition modelling (FDM) of composites of graphene nanoplatelets and polymers for high thermal conductivity: a mini-review,” *Funct. Compos. Mater.*, vol. 1, no. 1, Dec. 2020, doi: 10.1186/s42252-020-00005-x.

[84] Ü. Çevik and M. Kam, “A Review Study on Mechanical Properties of Obtained Products by FDM Method and Metal/Polymer Composite Filament Production,” *J. Nanomater.*, vol. 2020, 2020, doi: 10.1155/2020/6187149.

[85] Z. Zhang *et al.*, “3D Printing Processability of a Thermally Conductive Compound Based on Carbon Nanofiller-Modified Thermoplastic Polyamide 12,” *Polymers (Basel).*, vol. 14, no. 3, p. 470, Jan. 2022, doi: 10.3390/polym14030470.

[86] R. T. L. Ferreira, I. C. Amatte, T. A. Dutra, and D. Bürger, “Experimental characterization and micrography of 3D printed PLA and PLA reinforced with short carbon fibers,” *Compos. Part B Eng.*, vol. 124, pp. 88–100, Sep. 2017, doi: 10.1016/j.compositesb.2017.05.013.

[87] I. Blanco, G. Cicala, and G. Recca, “Specific Heat Capacity and Thermal Conductivity Measurements of PLA-Based 3D-Printed Parts with Milled Carbon Fiber Reinforcement,” 2022.

[88] D. Zhu *et al.*, “Thermal and mechanical properties of polyamide 12/graphene nanoplatelets nanocomposites and parts fabricated by fused deposition modeling,” *J. Appl. Polym. Sci.*, vol. 134, no. 39, pp. 1–13, 2017, doi: 10.1002/app.45332.

[89] L. J. Love *et al.*, “The importance of carbon fiber to polymer additive manufacturing,” *J. Mater. Res.*, vol. 29, no. 17, pp. 1893–1898, 2014, doi: 10.1557/jmr.2014.212.

[90] A. Dorigato, V. Moretti, S. Dul, S. H. Unterberger, and A. Pegoretti, “Electrically conductive nanocomposites for fused deposition modelling,” *Synth. Met.*, vol. 226, pp. 7–14, 2017, doi:

10.1016/j.synthmet.2017.01.009.

[91] Z. Liu, Q. Lei, and S. Xing, “Mechanical characteristics of wood, ceramic, metal and carbon fiber-based PLA composites fabricated by FDM,” *J. Mater. Res. Technol.*, vol. 8, no. 5, pp. 3743–3753, 2019, doi: 10.1016/j.jmrt.2019.06.034.

[92] A. A. Hassen *et al.*, “Anisotropic thermal behavior of extrusion-based large scale additively manufactured carbon-fiber reinforced thermoplastic structures,” no. March, pp. 1–13, 2022, doi: 10.1002/pc.26645.

[93] G. Liu, Y. Xiong, and L. Zhou, “Additive manufacturing of continuous fiber reinforced polymer composites: Design opportunities and novel applications,” *Compos. Commun.*, vol. 27, no. August, p. 100907, 2021, doi: 10.1016/j.coco.2021.100907.

[94] S. M. F. Kabir, K. Mathur, and A.-F. M. Seyam, “A critical review on 3D printed continuous fiber-reinforced composites: History, mechanism, materials and properties,” *Compos. Struct.*, vol. 232, p. 111476, Jan. 2020, doi: 10.1016/j.compstruct.2019.111476.

[95] F. Baumann, J. Scholz, and J. Fleischer, “Investigation of a New Approach for Additively Manufactured Continuous Fiber-reinforced Polymers,” *Procedia CIRP*, vol. 66, pp. 323–328, 2017, doi: 10.1016/j.procir.2017.03.276.

[96] H. Prüß and T. Vietor, “Design for Fiber-Reinforced Additive Manufacturing,” *J. Mech. Des.*, vol. 137, no. 11, p. 111409, 2015, doi: 10.1115/1.4030993.

[97] A. N. Dickson, J. N. Barry, K. A. Mcdonnell, and D. P. Dowling, “Fabrication of continuous carbon , glass and Kevlar fibre reinforced polymer composites using additive manufacturing,” *Addit. Manuf.*, vol. 16, pp. 146–152, 2017, doi: 10.1016/j.addma.2017.06.004.

[98] F. Zhang, G. Ma, and Y. Tan, “The Nozzle Structure Design and Analysis for Continuous Carbon Fiber Composite 3D Printing,” *Adv. Eng. Res.*, vol. 136, no. Icadme, pp. 193–199, 2017.

[99] T. H. J. Vaneker, “Material Extrusion of Continuous Fiber Reinforced Plastics Using Commingled Yarn,” *Procedia CIRP*, vol. 66, pp. 317–322, 2017, doi: 10.1016/j.procir.2017.03.367.

[100] Y. Ming, Z. Xin, J. Zhang, Y. Duan, and B. Wang, “Fabrication of continuous glass fiber-reinforced dual-cure epoxy composites via UV-assisted fused deposition modeling,” *Compos. Commun.*, vol. 21, Oct. 2020, doi: 10.1016/j.coco.2020.100401.

[101] R. Matsuzaki *et al.*, “Three-dimensional printing of continuous-fiber composites by in-nozzle impregnation,” *Sci. Rep.*, vol. 6, pp. 1–7, 2016, doi: 10.1038/srep23058.

[102] Y. Ibrahim, G. W. Melenka, and R. Kempers, “Fabrication and tensile testing of 3D printed continuous wire polymer composites,” *Rapid Prototyp. J.*, vol. 24, no. 7, pp. 1131–1141, Oct. 2018, doi: 10.1108/RPJ-11-2017-0222.

[103] Y. Ibrahim, G. W. Melenka, and R. Kempers, “Additive manufacturing of Continuous Wire Polymer Composites,” *Manuf. Lett.*, vol. 16, no. April, pp. 49–51, 2018, doi: 10.1016/j.mfglet.2018.04.001.

[104] K. Mori, T. Maeno, and Y. Nakagawa, “Dieless Forming of Carbon Fibre Reinforced Plastic Parts Using 3D Printer,” *Procedia Eng.*, vol. 81, no. October, pp. 1595–1600, 2014, doi: 10.1016/j.proeng.2014.10.196.

[105] M. Araya-Calvo *et al.*, “Evaluation of compressive and flexural properties of continuous fiber fabrication additive manufacturing technology,” *Addit. Manuf.*, vol. 22, no. May, pp. 157–164, 2018, doi: 10.1016/j.addma.2018.05.007.

[106] E. Giarmas, K. Tsongas, E. K. Tzimtzimis, A. Korlos, and D. Tzetzis, “Mechanical and fea-assisted characterization of 3d printed continuous glass fiber reinforced nylon cellular structures,” *J. Compos. Sci.*, vol. 5, no. 12, Dec. 2021, doi: 10.3390/jcs5120313.

[107] M. Heidari-Rarani, M. Rafiee-Afarani, and A. M. Zahedi, “Mechanical characterization of FDM 3D printing of continuous carbon fiber reinforced PLA composites,” *Compos. Part B*

Eng., vol. 175, Oct. 2019, doi: 10.1016/j.compositesb.2019.107147.

[108] H. Zhang, J. Wu, C. Robert, C. M. Ó Brádaigh, and D. Yang, "3D printing and epoxy-infusion treatment of curved continuous carbon fibre reinforced dual-polymer composites," *Compos. Part B Eng.*, vol. 234, p. 109687, Apr. 2022, doi: 10.1016/j.compositesb.2022.109687.

[109] J. M. Chacón, M. A. Caminero, P. J. Núñez, E. García-Plaza, I. García-Moreno, and J. M. Reverte, "Additive manufacturing of continuous fibre reinforced thermoplastic composites using fused deposition modelling: Effect of process parameters on mechanical properties," *Compos. Sci. Technol.*, vol. 181, p. 107688, Sep. 2019, doi: 10.1016/j.compscitech.2019.107688.

[110] J. Shang *et al.*, "Controllable inter-line bonding performance and fracture patterns of continuous fiber reinforced composites by sinusoidal-path 3D printing," *Compos. Sci. Technol.*, vol. 192, no. October 2019, p. 108096, 2020, doi: 10.1016/j.compscitech.2020.108096.

[111] N. Kumekawa, Y. Mori, H. Tanaka, and R. Matsuzaki, "Experimental evaluation of variable thickness 3D printing of continuous carbon fiber-reinforced composites," *Compos. Struct.*, vol. 288, no. February, p. 115391, 2022, doi: 10.1016/j.compstruct.2022.115391.

[112] Y. Ibrahim, A. Elkholy, J. S. Schofield, G. W. Melenka, and R. Kempers, "Effective thermal conductivity of 3D-printed continuous fiber polymer composites," *Adv. Manuf. Polym. Compos. Sci.*, vol. 6, no. 1, pp. 17–28, 2020, doi: 10.1080/20550340.2019.1710023.

[113] A. Elkholy, M. Rouby, and R. Kempers, "Characterization of the anisotropic thermal conductivity of additively manufactured components by fused filament fabrication," *Prog. Addit. Manuf.*, vol. 4, no. 4, pp. 497–515, 2019, doi: 10.1007/s40964-019-00098-2.

[114] A. Elkholy and R. Kempers, "An accurate steady-state approach for characterizing the thermal conductivity of Additively manufactured polymer composites," *Case Stud. Therm.*

Eng., vol. 31, no. December 2021, p. 101829, 2022, doi: 10.1016/j.csite.2022.101829.

[115] G. W. Melenka, E. Lepp, B. K. O. Cheung, and J. P. Carey, “Micro-computed tomography analysis of tubular braided composites,” *Compos. Struct.*, vol. 131, pp. 384–396, 2015, doi: 10.1016/j.compstruct.2015.05.057.

[116] C. Shemelya *et al.*, “Anisotropy of thermal conductivity in 3D printed polymer matrix composites for space based cube satellites,” *Addit. Manuf.*, vol. 16, pp. 186–196, 2017, doi: 10.1016/j.addma.2017.05.012.

[117] Stepashkin, D. I. Chukov, F. S. Senatov, A. I. Salimon, A. M. Korsunsky, and S. D. Kaloshkin, “3D-printed PEEK-carbon fiber (CF) composites: Structure and thermal properties,” *Compos. Sci. Technol.*, vol. 164, pp. 319–326, Aug. 2018, doi: 10.1016/j.compscitech.2018.05.032.

[118] M. Spoerk *et al.*, “Anisotropic properties of oriented short carbon fibre filled polypropylene parts fabricated by extrusion-based additive manufacturing,” *Compos. Part A Appl. Sci. Manuf.*, vol. 113, no. January, pp. 95–104, 2018, doi: 10.1016/j.compositesa.2018.06.018.

[119] N. Nguyen, E. Melamed, J. G. Park, S. Zhang, A. Hao, and R. Liang, “Direct Printing of Thermal Management Device Using Low-Cost Composite Ink,” *Macromol. Mater. Eng.*, vol. 302, no. 10, pp. 1–6, 2017, doi: 10.1002/mame.201700135.

[120] J. Ji *et al.*, “Enhanced thermal conductivity of alumina and carbon fibre filled composites by 3-D printing,” *Thermochim. Acta*, vol. 690, Aug. 2020, doi: 10.1016/j.tca.2020.178649.

[121] Y. Hu, R. B. Ladani, M. Brandt, Y. Li, and A. P. Mouritz, “Carbon fibre damage during 3D printing of polymer matrix laminates using the FDM process,” *Mater. Des.*, vol. 205, p. 109679, 2021, doi: 10.1016/j.matdes.2021.109679.

[122] M. A. Caminero, J. M. Chacón, I. García-Moreno, and G. P. Rodríguez, “Impact damage resistance of 3D printed continuous fibre reinforced thermoplastic composites using fused deposition modelling,” *Compos. Part B Eng.*, vol. 148, pp. 93–103, Sep. 2018, doi:

10.1016/j.compositesb.2018.04.054.

[123] M. A. Caminero, I. García-Moreno, G. P. Rodríguez, and J. M. Chacón, “Internal damage evaluation of composite structures using phased array ultrasonic technique: Impact damage assessment in CFRP and 3D printed reinforced composites,” *Compos. Part B Eng.*, vol. 165, pp. 131–142, May 2019, doi: 10.1016/j.compositesb.2018.11.091.

[124] M. A. Caminero, J. M. Chacón, I. García-Moreno, and J. M. Reverte, “Interlaminar bonding performance of 3D printed continuous fibre reinforced thermoplastic composites using fused deposition modelling,” *Polym. Test.*, vol. 68, no. March, pp. 415–423, 2018, doi: 10.1016/j.polymertesting.2018.04.038.

[125] X. Liao *et al.*, “High strength in combination with high toughness in robust and sustainable polymeric materials,” *Science (80-.).*, vol. 366, no. 6471, pp. 1376–1379, 2019, doi: 10.1126/science.aay9033.

[126] X. J. Hu, A. A. Padilla, J. Xu, T. S. Fisher, and K. E. Goodson, “3-Omega Measurements of Vertically Oriented Carbon Nanotubes on Silicon,” *J. Heat Transfer*, vol. 128, no. 11, pp. 1109–1113, 2006, doi: 10.1115/1.2352778.

[127] D. G. Cahill, “Thermal conductivity measurement from 30 to 750 K: The 3ω method,” *Rev. Sci. Instrum.*, vol. 61, no. 2, pp. 802–808, 1990, doi: 10.1063/1.1141498.

[128] H. D. Wang, J. H. Liu, X. Zhang, and Y. Song, “Raman measurements of optical absorption and heat transfer coefficients of a single carbon fiber in atmosphere environment,” *Int. J. Heat Mass Transf.*, vol. 70, pp. 40–45, 2014, doi: 10.1016/j.ijheatmasstransfer.2013.10.054.

[129] L. J. Majerus, “Application of the Thermal Flash Technique for Characterizing High Thermal Diffusivity Micro and Nanostructures,” 2010.

[130] X. Zhang, S. Fujiwara, and M. Fujii, “Measurements of thermal conductivity and electrical conductivity of a single carbon fiber,” *Int. J. Thermophys.*, vol. 21, no. 4, pp. 965–980, 2000,

doi: 10.1023/A:1006674510648.

[131] J. L. Wang, M. Gu, X. Zhang, and Y. Song, “Thermal conductivity measurement of an individual fibre using a T type probe method,” *J. Phys. D. Appl. Phys.*, vol. 42, no. 10, 2009, doi: 10.1088/0022-3727/42/10/105502.

[132] J. Yang, L. Kong, B. Mu, H. Zhang, Y. Li, and W. Cao, “Measurement of intrinsic thermal conductivity of carbon fiber using direct electrical heating method,” *Rev. Sci. Instrum.*, vol. 90, no. 11, Nov. 2019, doi: 10.1063/1.5124720.

[133] C. Dames *et al.*, “A hot-wire probe for thermal measurements of nanowires and nanotubes inside a transmission electron microscope,” *Rev. Sci. Instrum.*, vol. 78, no. 10, 2007, doi: 10.1063/1.2785848.

[134] L. Piraux, J. P. Issi, and P. Coopmans, “Apparatus for thermal conductivity measurements on thin fibres,” *Measurement*, vol. 5, no. 1, pp. 2–5, 1987, doi: 10.1016/0263-2241(87)90020-0.

[135] P. W. May, R. Portman, and K. N. Rosser, “Thermal conductivity of CVD diamond fibres and diamond fibre-reinforced epoxy composites,” *Diam. Relat. Mater.*, vol. 14, no. 3–7, pp. 598–603, 2005, doi: 10.1016/j.diamond.2004.10.039.

[136] R. Manglik, *Heat Transfer and Fluid Flow Data Books*. Genium Publishing Corporation. [Online]. Available: https://app.knovel.com/hotlink/toc/id:kpHTFFDB0F/heat-transfer-fluid-flow/heat-transfer-fluid-flow

[137] M. Fujii *et al.*, “Measuring the thermal conductivity of a single carbon nanotube,” *Phys. Rev. Lett.*, vol. 95, no. 6, Aug. 2005, doi: 10.1103/PhysRevLett.95.065502.

[138] K. Naito, Y. Tanaka, J. M. Yang, and Y. Kagawa, “Flexural properties of PAN- and pitch-based carbon fibers,” *J. Am. Ceram. Soc.*, vol. 92, no. 1, pp. 186–192, Jan. 2009, doi: 10.1111/j.1551-2916.2008.02868.x.

[139] J. S. Steinhart and S. R. Hart, “Calibration curves for thermistors,” *Deep. Res. Oceanogr.*

Abstr., vol. 15, no. 4, pp. 497–503, 1968, doi: 10.1016/0011-7471(68)90057-0.

[140] Y. Ibrahim, C. Isaacs, and R. Kempers, “3D Printing of Pitch Carbon Fiber Composites for Heat Exchanger Applications,” in *14 International Conference on Heat, Fluid Mechanics and Thermodynamics*, 2019, pp. 1–7.

[141] S. J. Kline, “Describing uncertainty in single sample experiments,” *Mech. Eng.*, vol. 75, pp. 3–8, 1953.

[142] N. Li, G. Link, and J. Jelonnek, “3D microwave printing temperature control of continuous carbon fiber reinforced composites,” *Compos. Sci. Technol.*, vol. 187, no. December 2019, p. 107939, 2020, doi: 10.1016/j.compscitech.2019.107939.

[143] B. Akhoundi, M. Nabipour, O. Kordi, and F. Hajami, “Calculating printing speed in order to correctly print PLA/continuous glass fiber composites via fused filament fabrication 3D printer,” *J. Thermoplast. Compos. Mater.*, 2021, doi: 10.1177/0892705721997534.

[144] T. C. Yang and C. H. Yeh, “Morphology and mechanical properties of 3D printed wood fiber/polylactic acid composite parts using Fused Deposition Modeling (FDM): The effects of printing speed,” *Polymers (Basel).*, vol. 12, no. 6, p. 1334, 2020, doi: 10.3390/POLYM12061334.

[145] D. Young, N. Wetmore, and M. Czabaj, “Interlayer fracture toughness of additively manufactured unreinforced and carbon-fiber-reinforced acrylonitrile butadiene styrene,” *Addit. Manuf.*, vol. 22, no. November 2017, pp. 508–515, 2018, doi: 10.1016/j.addma.2018.02.023.

[146] S. Milenkovic, V. Slavkovic, C. Fragassa, N. Grujovic, N. Palic, and F. Zivic, “Effect of the raster orientation on strength of the continuous fiber reinforced PVDF/PLA composites, fabricated by hand-layup and fused deposition modeling,” *Compos. Struct.*, vol. 270, no. February, p. 114063, 2021, doi: 10.1016/j.compstruct.2021.114063.

[147] E. Ivanov *et al.*, “PLA/Graphene/MWCNT composites with improved electrical and thermal

properties suitable for FDM 3D printing applications," *Appl. Sci.*, vol. 9, no. 6, 2019, doi: 10.3390/app9061209.

[148] P. Urhal, A. Weightman, C. Diver, and P. Bartolo, "Robot assisted additive manufacturing: A review," *Robot. Comput. Integr. Manuf.*, vol. 59, pp. 335–345, Oct. 2019, doi: 10.1016/j.rcim.2019.05.005.

[149] Y. Yao, Y. Zhang, M. Aburaia, and M. Lackner, "3d printing of objects with continuous spatial paths by a multi-axis robotic fff platform," *Appl. Sci.*, vol. 11, no. 11, Jun. 2021, doi: 10.3390/app11114825.

[150] A. İpekçi and B. Ekici, "Experimental and statistical analysis of robotic 3D printing process parameters for continuous fiber reinforced composites," *J. Compos. Mater.*, 2021, doi: 10.1177/0021998321996425.

[151] Z. Li, L. Wang, and G. Ma, "Mechanical improvement of continuous steel microcable reinforced geopolymer composites for 3D printing subjected to different loading conditions," *Compos. Part B Eng.*, vol. 187, no. November 2019, p. 107796, 2020, doi: 10.1016/j.compositesb.2020.107796.

[152] M. Pollák, J. Kaščak, M. Telišková, and J. Tkáč, "Design of the 3D printhead with extruder for the implementation of 3D printing from plastic and recycling by industrial robot," *TEM J.*, vol. 8, no. 3, pp. 709–713, 2019, doi: 10.18421/TEM83-02.

[153] "IRB 1200," *ABB Robotics*, 2022. https://new.abb.com/products/robotics/industrial-robots/irb-1200